Doklady Physics, Vol. 47, No. 7, 2002, pp. 485–487. Translated from Doklady Akademii Nauk, Vol. 385, No. 1, 2002, pp. 41–43.

PHYSICS

Reversible Loss of Strength of C_{60} Single-Crystal Fullerite under the Action of Ultra-Weak Ionizing Radiation

Yu. I. Golovin*, A. A. Dmitrievskiĭ*, R. K. Nikolaev, and I. A. Pushnin***

Presented by Academician Yu.A. Osip'yan January 30, 2002

Received January 30, 2002

When examining the action of ionizing radiation on various objects of an animal or lifeless nature, radiation effects corresponding to moderate absorption doses D (conditionally from ~1 to ~10^8 Gy) have been comprehensively studied. However, the response of the objects to doses $D \ll 1$ Gy and $D \gg 10^8$ Gy have not been thoroughly investigated. In addition, this response cannot be reliably predicted in the general case by directly extrapolating data obtained for moderate values of D. For example, in materials science, there exists a complicated nonmonotonic dependence of the variation of initial properties on the absorbed dose or on fluence [1]. For low doses D, instead of the usual (for moderate doses) strengthening, the loss of strength by crystals [2, 3], rapid relaxation of nonequilibrium defect structures in them [4], the growth of internal-friction peaks in polymeric materials [5], and changes in phase-transition conditions of ferroelectrics [6], etc. can occur. In radiobiological studies, the so-called sensitivity-window effect often manifests itself. This effect consists of anomalously strong biochemical and physiological responses that correspond to certain ranges of low exposure intensities and irradiation doses [7]. At the same time, information concerning the variation in physical properties of fullerites under the action of ionizing radiation [8–10] remains limited.

In the present paper, we discuss the discovery of an effect whereby a decrease in the microhardness H of C_{60} fullerite is observed as a result of its exposure to β^+ and γ radiation with doses $D < 0.1$ cGy. At room temperature, the microhardness was restored to its initial value approximately 30 h after the exposure had finished. Afterwards, the microhardness could be reversibly lowered again by subsequent irradiation.

* *Tambov State University, ul. Internatsional'naya 33, Tambov, 392622 Russia*

** *Institute of Physics of Solids, Russian Academy of Sciences, Chernogolovka, Moscow oblast, 132432 Russia*

E-mail: golovin@tsu.tmb.ru

The $^{137}_{55}Cs$ radionuclide with an activity $A = 4.2$ MBq was taken as a radiation source. Together with γ-rays having the maximal energy $E'_m = 0.66$ MeV and a quantum yield of 0.85 per decay, this radionuclide emits β^--particles within two spectral ranges having the maximal energies $E'_m = 0.564$ and 1.176 MeV with quantum yields 0.947 and 0.053 per decay, respectively [11]. In the zone where the sample is placed, the calculated absorbed-dose rate of the γ-ray component reached $I_\gamma = 88$ μGy h^{-1}, while the β^--particle flux density was $I_\beta = 9.3 \times 10^3$ cm^{-2} s^{-1}.

Due to the small penetration depth (tens of microns) in a crystal of β^--particles with energies of <1 MeV, we used the method of dynamic nanoindentation [12] for investigating their possible effect on the mechanical properties of thin near-surface layers. In all experiments, the maximal load was 200 mN, while the maximal print depth attained was about 7 μm. To avoid the rapid oxidation of the sample surface, all the manipulations (irradiation, measurements of the microhardness, holding after an exposure) were performed in the dark or in weak red illumination.

As is seen from the figure (in which every point was obtained by averaging 15–20 individual measurements), the increase in the dose of the combined β^+ and γ-irradiation resulted in a decrease in the sample microhardness. In this case, saturation was observed in a time $t_{sat} \sim 6$ h. After the exposure had finished, complete restoration of the initial microhardness was observed (after a ~30-hour holding at room temperature). Repeated irradiation after holding resulted in a loss of strength corresponding to the same amplitude as had been observed for the first irradiation.

We have studied the effect of sample screening by an aluminum plate 2 mm thick, which completely absorbed the β^- component. The intensity of the γ component was virtually unaffected by the screening, which led to the disappearance of the strength-loss effect. In other words, the doses of γ radiation used did not cause a measurable variation of H. The problem of the role of γ irradiation for the combined action of β^-

1028-3358/02/4707-0485$22.00

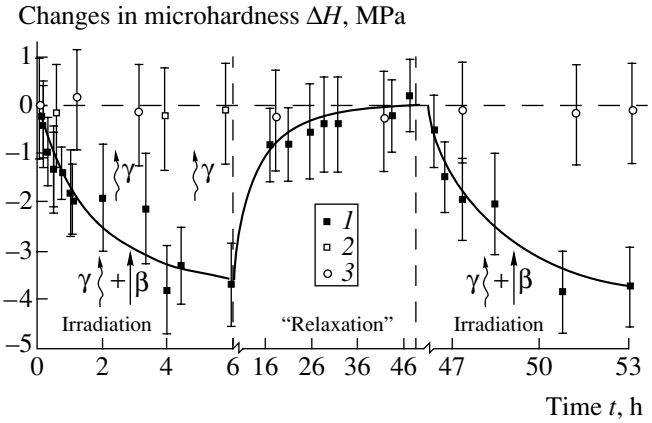

C_{60} microhardness variations ΔH as a function of time t: (*1*) after irradiation by a combined flux of β^+-particles and γ-rays; (*2*) after irradiation by γ-rays; (*3*) after polishing the oxidized surface layer (in the absence of irradiation).

and γ components requires special consideration. However, it is clear that, for approximately equal fluxes of particles and energies carried by the β^- and γ components, the role of the former in changing the properties of near-surface layers must be more pronounced than that of the latter. Indeed, for the weighted-average energy $\langle E_\beta \rangle = 179.8$ keV of β-particles in the flux emitted by the $^{137}_{55}Cs$ radioactive nuclide [11], the thickness of the absorbing layer for these particles is smaller by a factor of approximately $\sim 10^3$ than for γ-rays with $E_\gamma = 0.66$ MeV. In addition, the bulk density of excited states in the near-surface layer is, correspondingly, higher by approximately the same factor.

We now estimate the number n of atomic defects produced by the flux of β^--particles for the maximum fluence $F = I_\beta t_{sat} \approx 2 \times 10^8$ cm^{-2}, which was used by us. Usually, it is assumed that the energy spent for the production of an atomic radiative defect is $E_0 = 20$–30 eV. Then, in the near-surface layer with the thickness $h_{1/2} \approx 13$ μm, which absorbs half of the flux with an energy $\langle E_\beta \rangle = 0.18$ MeV [11], $n = F\langle E_\beta \rangle/(h_{1/2}E_0) \approx 10^{15}$ cm^{-3} of radiative defects are formed. For such a low concentration of structural defects, elucidation of the mechanism of their effect on plasticity characteristics requires a separate analysis. We can assume that there exist at least three possible reasons for the efficient action of low radiation doses on fullerite:

(1) The plasticity of fcc crystals is limited by the existence of local locks for slipping dislocations. In the C_{60} single crystals under investigation, these locks might be carbon molecules of different molecular mass (preferentially, C_{70}, dimers, oxidized molecules, admixtures of other chemical elements, etc.). Their total concentration in the near-surface layers amounts to $\sim 10^{-3}$–10^{-4}. The modification of even a small number of the strongest locks under the action of irradiation can increase the mobility of dislocations and lower the microhardness H.

(2) Excitations induced by the flux of β^--particles form point defects which are not dispersed stochastically over the bulk of a sample (as in the case of the γ-radiation), but produce quasi-one-dimensional tracks with a macroscopic length $h_{1/2} \sim 10$ μm, which can cause a more pronounced loss of strength.

(3) The saturation and closeness of covalent bonds inside a C_{60} molecule result in the fact that the plastic deformation of fullerite is realized preferentially by breaking weaker intermolecular bonds. Knocking out one or two carbon atoms from a symmetric C_{60} molecule can lead to the loss of its stability under loading and to macroscopic deformation. These processes can occur not only due to the slipping of certain ball-shaped molecules with respect to other ones, but also due to the disintegration of the molecules themselves. Such a multiplication of the action of a vacancy in the C_{60} molecular structure can result in a "house of cards" effect and may considerably increase the irradiation efficiency.

Of course, we offer only working hypotheses that require additional study. However, the very fact of the loss of fullerite strength under the action of such small doses of irradiation stimulates the search for similar effects in other cyclic carbon-containing substances (e.g., single crystals of the aromatic series, polymers, etc.) and obliges us to be more careful in dealing with the possible consequences of irradiation—even in the case of ultra-weak doses.

ACKNOWLEDGMENTS

This study was performed under the aegis of the Fullerenes and Atomic Clusters program, grant 2008, with financial support from the Russian Foundation for Basic Research, project nos. 00-02-16094 and 02-02-17571, and from the Ministry of Education of the Russian Federation, project no. E00-3.4-552.

REFERENCES

1. V. L. Indenbom, V. V. Kirsanov, and A. N. Orlov, *Problems of Atomic Science and Technology, Series: Physics of Radiation Damages and Radiation Materials Science* (Khar'kovskoe Fiziko-Tekhnicheskoe Izd., Kharkov, 1982), No. 2 (21), pp. 3–22.
2. V. A. Makara and N. N. Novikov, Fiz. Khim. Obrab. Mater., No. 6, 137 (1973).
3. S. Fujita, K. Maeda, and S. Hyodo, Phys. Status Solidi A **109**, 383 (1988).
4. V. A. Lomovskoĭ, A. G. Lipson, N. Yu. Lomovskaya, and I. A. Gagina, Vysokomol. Soedin., Ser. A **2**, 980 (2000).

5. A. G. Lipson, D. M. Sakov, V. I. Savenko, and E. I. Saunin, Pis'ma Zh. Éksp. Teor. Fiz. **70** (2), 118 (1999) [JETP Lett. **70** (2), 123 (1999)].
6. A. G. Lipson, D. M. Sakov, E. I. Saunin, and V. A. Kuznetsov, Zh. Fiz. Khim. **74**, 1452 (2000).
7. L. S. Vartanyan, S. M. Gurevich, A. I. Kozachenko, *et al.*, Biokhimiya **65** (4), 522 (2000).
8. C. E. Foerster, C. M. Lapienski, F. C. Serbena, and F. C. Zawislak, Thin Solid Films **340,** 201 (1999).
9. V. M. Mikushkin and V. V. Shnitov, Fiz. Tverd. Tela (St. Petersburg) **39** (1), 187 (1997) [Phys. Solid State **39,** 164 (1997)].
10. Yu. S. Gordeev, V. M. Mikushkin, and V. V. Shnitov, Fiz. Tverd. Tela (St. Petersburg) **42** (2), 371 (2000) [Phys. Solid State **42,** 381 (2000)].
11. V. F. Kozlov, *Reference Book on Radiation Safety* (Énergoatomizdat, Moscow, 1991).
12. Yu. I. Golovin, V. I. Ivolgin, V. V. Korenkov, and V. Ya. Farber, Fiz. Tverd. Tela (St. Petersburg) **43** (11), 2021 (2001) [Phys. Solid State **43,** 2105 (2001)].

Translated by G. Merzon

Doklady Physics, Vol. 47, No. 7, 2002, pp. 488–491. From Doklady Akademii Nauk, Vol. 385, No. 1, 2002, pp. 44–47.

PHYSICS

The Role of the Finite-Orbit Effect in Theory of Magnetic Islands in Tokamaks[1]

S. V. Konovalov*, A. B. Mikhaĭlovskiĭ*, V. S. Tsypin, and S. E. Sharapov*****

Presented by Academician A.M. Fridman January 23, 2002

Received January 29, 2002

1. In tokamaks, plasma particles (ions and electrons) are excursive with respect to a corresponding magnetic-field line as a result of the so-called magnetic drift, i.e., the drift due to both the curvature and the transverse inhomogeneity of the magnetic field (see [1] and references therein). Such drift is sign-variable, so that a particle deviates from the magnetic-field line only by a certain finite distance Λ called the orbit size of the drift motion. Therefore, when a perturbation of an electromagnetic field with a characteristic transverse wave number $k_\perp$ arises, the plasma response to this perturbation depends on the parameter $k_\perp\Lambda$. The theory of linear instabilities of tokamak plasma for finite $k_\perp\Lambda$ was developed in [1] and in a series of other original papers. Furthermore, the results of these papers were comprehensively systematized in the monographs [2, 3] and the review [4].

Presently, extensive theoretical and experimental investigations on the magnetic islands in tokamaks are performed (see the review [5] and references therein). The appearance of nonlinear regular structures of such a type leads to the reconnection of the magnetic field lines and, as a result, to enhanced transverse heat transport and limitations imposed on the parameter β, i.e., the ratio of plasma pressure to magnetic-field pressure. This is unacceptable for fusion reactors of the ITER (International Thermonuclear Experimental Reactor) type; for details see [6]. Up to now, much attention has been devoted to studying magnetic islands with a half-width w considerably larger than the ion drift-orbit size, i.e., $w > \Lambda$. In addition, a series of papers, e.g., [7], was devoted to studying islands with a half-width smaller than the ion Larmor radius ρ_i, $w < \rho_i$. In this context, the question arises as to whether magnetic islands satisfying the conditions

$$\rho_i < w < \Lambda \tag{1}$$

exist.

Since the value of Λ depends on the pitch angle (the circularity degree) of a particle, i.e., on the ratio of its characteristic transverse and longitudinal velocities, and since, for strongly circulating particles, $\Lambda \simeq \rho_i$, it is evident that we can consider islands satisfying conditions (1) only in the case of weakly circulating ions. Actually, according to [1–4], for these ions, we have

$$\Lambda \simeq \frac{\rho_i}{\epsilon^{1/2}} \gg \rho_i. \tag{2}$$

Here, ϵ is the ratio of minor and major tokamak radii, i.e., the so-called inverse aspect ratio. An orbit size on the order of (2) also is typical for trapped ions. With allowance for the above, the problem of the evolution of islands with half-width satisfying the condition

$$\rho_i < w < \frac{\rho_i}{\epsilon^{1/2}} \tag{3}$$

is important. Studying such islands is the main goal of the present paper.

Inequalities (1)–(3) imply single-temperature plasma; i.e., they exclude the possibility of the existence of a group of high-energy ions. Meanwhile, the presence of high-energy ions is typical for recent experimental facilities (for instance, for JET [8]). This is caused by the injection of a beam of high-energy neutral atoms or the acceleration of a group of ions in conditions of ion cyclotron resonance. The size of drift orbits for high-energy ions substantially exceeds estimate (2). Therefore, in addition to the islands satisfying condition (3), we also analyze islands obeying inequality (1) and assume that Λ is the characteristic orbit size for the high-energy ions.

2. Elucidating the role of the effect of interest is reduced to analyzing the contribution of finite-orbit particles to the evolution equation for the magnetic-

[1] The article was submitted by the authors in English.

* *Institute of Nuclear Fusion, Russian Research Centre Kurchatov Institute, pl. Kurchatova 1, Moscow, 123182 Russia*

** *Institute of Physics, University of São Paulo, Rua do Matão, Travessa R, 187, 05508-900, São Paulo, Brazil*

*** *EURATOM/UKAEA Fusion Association, Culham Science Center, Abingdon, OXON OX14 3EA, United Kingdom*

1028-3358/02/4707-0488$22.00

island width, which is usually called the generalized Rutherford equation. Following [6, 7, 9–11], we represent this equation in the form

$$\frac{dw}{dt} \sim \frac{\Delta'}{4} + \Delta^{\Lambda} + \dots . \quad (4)$$

Here, the sign ~ implies equality with an accuracy to a certain positive coefficient, so that effects with a positive or negative contribution to the right-hand side of Eq. (4) lead to growth or decay of the islands, respectively. The quantity Δ' is usually called the tearing-mode stability parameter. The sign of the term with Δ' in Eq. (4) depends on the character of the radial distribution of the longitudinal plasma current. In the case of a well organized discharge, we have $\Delta' < 0$; i.e., the effect caused by the term with Δ' is stabilizing. The terms corresponding to the trend of the parametric instability characterize effects of the bootstrap current Δ_{bs}, polarization current Δ_p, and magnetic well Δ_{mw} (see [5] for details). These effects were comprehensively studied in preceding publications in the approximation of sufficiently large-scale islands, $w < \frac{\rho_i}{\epsilon^{1/2}}$. We can expect that the corresponding terms, usually denoted as Δ_{bs}, Δ_p, and Δ_{mw} [5], should be modified in the case of interest, i.e., when $w < \frac{\rho_i}{\epsilon^{1/2}}$. The study of such a modification could be the subject of further publications. Within the scope of the present work, we analyze only the effect characterized by the term Δ^{Λ}. Here, superscript Λ emphasizes that we deal with the contribution of particles with large drift orbits Λ.

For calculating Δ^{Λ}, we introduce standard variables ψ and ξ characterizing the island configuration of the magnetic field [5, 10, 11], where $\psi = \tilde{\psi}\cos\xi - \frac{x^2 B_0}{2L_s}$ and $\xi = m\theta - n\zeta - \omega t$. Here, $\tilde{\psi}$ is the perturbation amplitude; x is the distance from the rational (singular) magnetic surface around which the islands are localized; B_0 is the equilibrium magnetic field at this surface; $L_s = \frac{qR}{s}$ is the so-called shear length; q is the safety factor; R is the major radius of the torus; $s = \frac{d\ln q}{d\ln r}$ is the shear; r is the radial coordinate; θ and ζ are the poloidal and toroidal angles, respectively; ω is the island-rotation frequency; and m and n are poloidal and toroidal mode numbers interrelated by the equality $\frac{m}{n} = q$, where q is taken at the rational magnetic surface $r = r_s$. The island half-width w introduced above is related to $\tilde{\psi}$ by the relationship $w = 2\left(\frac{L_s\tilde{\psi}}{B_0}\right)^{1/2}$. It is assumed that the values of L_s and s are taken at $r = r_s$.

Along with the variable ψ, which characterizes the magnetic flux of the island configuration, we introduce the dimensionless magnetic-flux function $\Omega = -\frac{\psi}{\tilde{\psi}}$. In addition, we introduce the function $j_{\parallel}^{\Lambda} = j_{\parallel}^{\Lambda}(\Omega, \xi)$, which characterizes the longitudinal current density in the island configuration due to the presence of large-orbit particles. Then, according to [5, 11], the quantity Δ^{Λ} is defined by the expression

$$\Delta^{\Lambda} = -\frac{2^{3/2}Rq}{cswB_0}\sum_{\sigma_x}\int_1^{\infty} d\Omega \oint \frac{j_{\parallel}^{\Lambda}\cos\xi\, d\xi}{(\Omega + \cos\xi)^{1/2}}. \quad (5)$$

Here, c is the speed of light and $\sigma_x = \operatorname{sgn} x = \pm 1$. Physically, the integration region in Eq. (5) corresponds to the space lying outside the magnetic-island separatrix. The contour integration over ξ in (5) implies integration from 0 to 2π.

3. We calculate $j_{\parallel}^{\Lambda}$ by taking account of the following considerations. We know the total density n_{Λ} of the ion Λ group and consider it as a sum of the equilibrium $n_{0\Lambda}$ and perturbed $\tilde{n}_{\Lambda}$ densities; i.e., $n_{\Lambda} = n_{0\Lambda} + \tilde{n}_{\Lambda}$. Allowing for the fact that the electric charge $e_i n_{\Lambda}$ of this ion group is compensated by the charge of the corresponding part of the electron-plasma component $e_e n_e^{\Lambda}$, i.e., in the simplest case, $e_i = -e_e = e$, we have $n_e^{\Lambda} = n_{\Lambda}$. It is the longitudinal motion of these compensating electrons that causes the longitudinal current $j_{\parallel}^{\Lambda}$. Assuming the electrons to be cold and allowing for their transverse motion in the crossed electric and magnetic fields, we conclude that $j_{\parallel}^{\Lambda}$ can be found on the basis of the electron continuity equation. Using the relations above, this equation can be written in the form

$$-e\frac{d_0}{dt}(n_{0\Lambda} + \tilde{n}_{\Lambda}) + \nabla_{\parallel} j_{\parallel}^{\Lambda} = 0. \quad (6)$$

Here, $\nabla_{\parallel}$ is the longitudinal gradient operator (along the total island magnetic field), $\frac{d_0}{dt} = \frac{\partial}{\partial t} + (\mathbf{V}_E \cdot \nabla)$, $\mathbf{V}_E = \frac{c[\mathbf{B}_0 \times \nabla\phi]}{B_0^2}$ is the electron velocity in the cross fields, ϕ is the electrostatic potential related to transverse electric field $\mathbf{E}_{\perp}$ by $\mathbf{E}_{\perp} = -\nabla_{\perp}\phi$, and $\nabla_{\perp}$ is the transverse gradient.

In order to calculate $\tilde{n}_{\Lambda}$, we turn to the drift kinetic equation (see, e.g., Eq. (16.70) in [3]). In general, we can use this equation to find the expression at $\tilde{n}_{\Lambda}$ for

arbitrary $k_\perp\Lambda$ (cf. [1]). However, in accordance with (1), we are interested only in the limiting case of large drift orbits, $k_\perp\Lambda \gg 1$. In this limiting case, assuming the particle-velocity distribution to be Maxwellian with the temperature T_Λ, we find

$$\tilde{n}_\Lambda = -\frac{e\phi}{T_\Lambda} n_{0\Lambda}. \quad (7)$$

Physically, relation (7) implies that, in the case of small-scale perturbations, the spatial distribution of the ion group under consideration obeys the Boltzmann law. Expression (7) can also be found from the corresponding formulas of [1] with the assumption that $k_\perp\Lambda \gg 1$ (in terms of [1], $k_\perp\Lambda$ is equal to $\xi_\parallel$).

4. For cold electrons, the electrostatic potential ϕ has the form [5, 10, 11]

$$\phi = \frac{B_0\omega}{ck_y}[x - h(\Omega)],$$

where $k_y = \dfrac{m}{r_s}$ and $h(\Omega)$ is the so-called electrostatic-potential profile function. In terms of the variables (Ω, ξ), the operator $\dfrac{d_0}{dt}$, if we ignore both the island width and rotation frequency, is defined by the relationship $\dfrac{d_0}{dt} = -\omega\Omega_x h'\dfrac{\partial}{\partial\xi}$, where $h' \equiv \dfrac{dh}{d\Omega}$ and $\Omega_x = \left(\dfrac{\partial\Omega}{\partial x}\right)_\xi$. We also take into account the fact that $n_{0\Lambda}(r) = n_{0\Lambda}(r_s) + x\left(\dfrac{\partial n_{0\Lambda}}{\partial r}\right)_{r=r_s}$. In addition, we have

$$x = \sigma_x\left(\frac{2L_s\tilde{\psi}}{B_0}\right)^{1/2}(\Omega + \cos\xi)^{1/2}, \quad \nabla_\parallel = k_\parallel\frac{\partial}{\partial\xi},$$

where $k_\parallel = -\dfrac{k_y x}{L_s}$. Then, (6) reduces to the form

$$\frac{\partial j_\parallel^\Lambda}{\partial\xi} = c_\Lambda g(\Omega)\frac{\sin\xi}{(\Omega + \cos\xi)^{1/2}}. \quad (8)$$

Here,

$$c_\Lambda = \frac{\pi}{4\sqrt{2}}\frac{\omega^2}{k_y^2}\frac{e^2 n_{0\Lambda}B_0L_s}{cT_\Lambda}\left(1 - \frac{\omega_{*\Lambda}}{\omega}\right), \quad (9)$$

$\omega_{*\Lambda} = \dfrac{k_y cT_\Lambda}{eB_0}\left(\dfrac{\partial \ln n_{0\Lambda}}{\partial r}\right)_{r=r_s}$ is the diamagnetic drift frequency of the ion group under consideration, and the function $g(\Omega)$ is defined (see [11]) by the relationship $g(\Omega) = \left(\dfrac{8\sigma_x}{\pi w}\right)h'(\Omega)$. Integrating (8) over ξ, we obtain

$$j_\parallel^\Lambda = -2c_\Lambda g(\Omega)[(\Omega + \cos\xi)^{1/2} - \langle(\Omega + \cos\xi)^{1/2}\rangle], \quad (10)$$

where $\langle\ldots\rangle$ implies averaging over ξ with the weight $(\Omega + \cos\xi)^{-1/2}$.

Substituting relationship (10) into Eq. (5), we find

$$\Delta^\Lambda = \frac{4\pi e^2 n_{0\Lambda}}{T_\Lambda c^2}\frac{\omega^2}{k_y^2}\frac{q^2R^2}{s^2w}\left(1 - \frac{\omega_{*\Lambda}}{\omega}\right)I, \quad (11)$$

where

$$I = -\frac{1}{2}\int_1^\infty d\Omega g(\Omega)\langle(\Omega + \cos\xi)^{1/2}\rangle\oint\frac{\cos\xi d\xi}{(\Omega + \cos\xi)^{1/2}}. \quad (12)$$

According to [11], $g(\Omega) = \displaystyle\int_0^\kappa \frac{d\kappa}{\lambda_3(\kappa)}$, where κ is related to Ω by $\kappa = \left[\dfrac{2}{\Omega + 1}\right]^{1/2}$. The function $\lambda_3(\kappa)$ is defined as

$$\lambda_3(\kappa) = \frac{1}{3}[2(2 - \kappa^2)E(\kappa) - (1 - \kappa^2)K(\kappa)], \quad (13)$$

where $K(\kappa)$ and $E(\kappa)$ are the complete elliptical integrals of the first and second kinds, respectively. Then, the integral I reduces to the form

$$I = 4\pi\int_0^1 d\kappa\frac{g(\kappa)}{\kappa^5}\left\{2\left[1 - \frac{E(\kappa)}{K(\kappa)}\right] - \kappa^2\right\}. \quad (14)$$

A numerical calculation yields $I = 1.50$.

5. According to equality (11), the quantity Δ^Λ depends on the shear and magnetic island half-width as $(s^2w)^{-1}$; the dependence is the same as that of the quantity Δ_{mw} characterizing the magnetic-well effect (see [5] for details). Consequently, the large-orbit effect, referred to below as the Λ-effect, can be treated as a variant of the magnetic-well effect.

To estimate the order of magnitude of the quantity Δ^Λ, we consider the case when the ions of the Λ-group are trapped and weakly circulating ions of the core plasma, i.e., when $n_{0\Lambda} \simeq \epsilon^{1/2}n_0$ and $T_\Lambda = T_i$, where n_0 and T_i are the core plasma density and ion temperature, respectively. In addition, we assume the island-rotation frequency ω to be on the order of the diamagnetic drift frequency $\omega_{\star\Lambda}$, so that $\dfrac{\omega}{k_y} \simeq \dfrac{v_{T_i}\rho_i}{L_n}$, where v_{T_i} is the ion thermal velocity and L_n is the characteristic length of the plasma-density inhomogeneity, which, for simplicity, is assumed to be on the order of r_s. Then, we find from integral (11) the estimate

$$\Delta^\Lambda \simeq \frac{\epsilon^{1/2}\beta_p}{s^2w}, \quad (15)$$

where $\beta_p = \frac{8\pi n_0 T_i}{B_\theta^2}$ (the so-called poloidal beta) and B_θ is the poloidal magnetic field (see, for details, [5]). We also have, according to [5], $\Delta_{mw} \simeq \frac{\epsilon^2 \beta_p}{s^2 w}$. Consequently, $\frac{\Delta^\Lambda}{\Delta_{mw}} \simeq \epsilon^{-3/2}$; i.e., the Λ effect is substantially stronger than the standard magnetic-well effect. We also note that for $s \simeq 1$, the estimate (15) for Δ^Λ is the same as that for Δ_{bs}, i.e., for the bootstrap current contribution to Eq. (4) of island-width evolution. It follows that, in studying the islands of sufficiently small width, i.e., for the condition (3), and allowing for the bootstrap current effect, we must also take into account the Λ effect.

According to relationships (11) and (14), for $\frac{\omega}{\omega_{*\Lambda}} > 1$, i.e., in the case of superdrift magnetic islands rotating in the direction of the ion diamagnetic drift, $\Delta^\Lambda > 0$. In other words, the Λ effect is destabilizing. On the other hand, for the subdrift magnetic islands rotating in the ion diamagnetic-drift direction for which $0 < \frac{\omega}{\omega_{*\Lambda}} < 1$, we have $\Delta^\Lambda < 0$; i.e., in this case, the Λ effect turns out to be stabilizing. These results are consistent with the predictions of [7] concerning the islands with $w < \rho_i$. In addition, according to relationships (11) and (14), the Λ effect is destabilizing ($\Delta^\Lambda > 0$) in the case of islands rotating in the direction of the electron diamagnetic drift, i.e., when $\frac{\omega}{\omega_{*\Lambda}} < 0$.

ACKNOWLEDGMENTS

The authors are grateful to R.M.O. Galvao and I.C. Nascimento for discussions stimulating this work.

The work was supported by the Program for the Support of Leading Scientific Schools, Russian Foundation for Basic Research project no. 00-15-96526; by the Research Support Foundation (FAPESP) of the State of Sao Paulo, and by the Excellence Research Programs (PRONEX) RMOG 50/70 Grant from the Ministry of Science and Technology, Brazil.

REFERENCES

1. A. B. Mikhaĭlovskiĭ and A. M. Fridman, Nucl. Fusion **16**, 837 (1976).
2. A. B. Mikhaĭlovskiĭ, *Instabilities of Plasma in Magnetic Traps* (Atomizdat, Moscow, 1978).
3. A. B. Mikhaĭlovskiĭ, *Instabilities in a Confined Plasma* (Institute of Physics, Bristol, 1998).
4. A. B. Mikhaĭlovskiĭ, *Review of Plasma Physics* (Consultant Bureau, New York, 1986), Vol. 9, pp. 103–264.
5. A. B. Mikhaĭlovskiĭ, Plasma Physics Contr. Fusion, 2002 (in press).
6. ITER Physics Expert Group on Disruptions, Plasma Control and MHD, ITER Physics Basis Editors, in *Nucl. Fusion*, 1999, Vol. 39, pp. 2251–2389.
7. A. I. Smolyakov, Sov. J. Plasma Phys. **15**, 667 (1989).
8. H. L. Berk, D. N. Borba, B. N. Breizman, *et al.*, Phys. Rev. Lett. **87**, 185002 (2001).
9. P. H. Rutherford, Phys. Fluids **16**, 1903 (1973).
10. A. B. Mikhaĭlovskiĭ, V. D. Pustovitov, V. S. Tsypin, and A. I. Smolyakov, Phys. Plasmas **7**, 1204 (2000).
11. S. V. Konovalov, A. B. Mikhaĭlovskiĭ, and V. S. Tsypin, Plasma Physics Contr. Fusion **44**, 579 (2002).

Doklady Physics, Vol. 47, No. 7, 2002, pp. 492–494. Translated from Doklady Akademii Nauk, Vol. 385, No. 1, 2002, pp. 48–50.

PHYSICS

Exact Solution of Equations of Magnetic Hydrodynamics for an Axisymmetric Plasma Flow

N. D. Naumov

Presented by Academician A.F. Andreev March 11, 2002

Received February 22, 2002

The construction of exact solutions to a set of nonlinear equations of magnetic hydrodynamics is of doubtless interest. The self-similar approach [1] turns out to be an efficient method of solving this problem. The method allows us to pass from solving a set of partial differential equations to integrating a set of ordinary differential equations, which is a much simpler problem. Such solutions to equations of magnetic hydrodynamics were previously obtained for unsteady plasma motions belonging to the class of continuum motions for which their velocities are proportional to the distance to the center of symmetry (see, e.g., [1, 2] and literature cited therein).

These studies dealt with the one-dimensional plasma motion when the ratio of a spatial coordinate and a certain function of time served as a self-similar variable. An analogous approach can be used for constructing solutions to steady equations of magnetic hydrodynamics in the case of axisymmetric flows provided that the transverse coordinate divided by a certain function of the longitudinal coordinate is chosen as a self-similar variable [3]. Using this method, we here construct an exact solution to equations of magnetic hydrodynamics in the case of two-dimensional axisymmetric plasma flows.

The condition rot[**VB**] = 0 of the magnetic field-line freezing-in is evidently satisfied for steady plasma flows provided that **B** = *w***V**, where *w* is a certain function. It is easy to see that the condition div**B** = 0 is satisfied if we set $w = A\rho$, where *A* is a certain constant, because in this case, the condition is equivalent to the continuity equation $\mathrm{div}\rho\mathbf{V} = 0$.

Therefore, for an axisymmetric flow, we set

$$\mathbf{V} = (V_r(r, z), 0, V_z(r, z)), \quad \mathbf{B} = A\rho\mathbf{V}. \tag{1}$$

In this case, from steady equations of magnetic hydrodynamics, we arrive at the following equations:

$$\frac{1}{r}\frac{\partial \rho r V_r}{\partial r} + \frac{\partial \rho V_z}{\partial z} = 0, \tag{2}$$

$$\rho\frac{\partial}{\partial r}V_r^2 = \rho V_z\frac{\partial}{\partial z}\left(\frac{\rho}{2\pi}A^2 - 2\right)V_r - \frac{\partial}{\partial r}\left(\frac{\rho^2}{4\pi}A^2V_z^2 + 2p\right), \tag{3}$$

$$\rho\frac{\partial}{\partial z}V_z^2 = \rho V_r\frac{\partial}{\partial r}\left(\frac{\rho}{2\pi}A^2 - 2\right)V_z - \frac{\partial}{\partial z}\left(\frac{\rho^2}{4\pi}A^2V_r^2 + 2p\right). \tag{4}$$

It is worth noting that Eq. (1) corresponds to the following azimuth component of the current density:

$$j_\varphi = \frac{cA}{4\pi}\left(\frac{\partial \rho V_r}{\partial z} - \frac{\partial \rho V_z}{\partial r}\right).$$

Hence, the constant *A* determines the electric current flowing in plasma.

A similar analytical solution to the set of Eqs. (2)–(4) can be obtained for the class of motions indicated above if the ratio of the radial coordinate and the flow radius $a = a(z)$ is chosen as a self-similar variable:

$$V_r = ua'\frac{r}{a}, \quad V_z = u. \tag{5}$$

Here, $u = u(z)$ is the longitudinal flow velocity and the primes stand for the derivatives with respect to *z*. For such a coordinate dependence of the velocity components, it is easy to verify that the function

$$\rho = \rho_0\frac{u_0R^2}{ua^2} \tag{6}$$

satisfies continuity equation (2), where *R*, ρ_0, and u_0 are constant values of the flow radius, density, and longitudinal velocity, respectively, at $z = 0$.

Substituting expressions (5) and (6) into Eq. (4), we arrive at the following differential equation:

$$Q\frac{u'}{a^2} + \frac{1}{8\pi}A^2Q^2r^2\frac{d}{dz}\frac{a'^2}{a^6} = -\frac{\partial p}{\partial z}.$$

1028-3358/02/4707-0492$22.00

This equation allows us to find the plasma pressure in the general form:

$$p(r, z) = p_0 - \frac{1}{8\pi}A^2Q^2r^2\frac{a'^2}{a^6} - Q\int_0^z \frac{u'}{a^2}dz. \qquad (7)$$

Here, for brevity, we introduce the notation $Q = \rho_0 u_0 R^2$.

Substituting expressions (5)–(7) into Eq. (3), we obtain the ordinary differential equation

$$\frac{d}{dz}ua' = \frac{1}{4\pi}QA^2\frac{d}{dz}\frac{a'}{a^2};$$

i.e., the longitudinal velocity is a function of the flow radius and its derivative:

$$u = \frac{1}{4\pi}\rho_0 u_0 A^2\frac{R^2}{a^2} + \frac{C}{a'},$$
$$C = u_0 a_0'\left(1 - \frac{1}{4\pi}\rho_0 A^2\right). \qquad (8)$$

As follows from Eqs. (8) for $A^2 = \frac{4\pi}{\rho_0}$, the longitudinal flow velocity is inversely proportional to the flow radius. According to Eq. (6), this corresponds to the case of incompressible plasma with $\rho = \rho_0$. A similar situation takes place for nonzero values of the initial divergence angle α, i.e., if $a_0' = \tan\alpha = 0$. In what follows, the electric current is characterized by a constant β defined by the equality $A^2 = \frac{4\pi\beta}{\rho_0}$; in the case of incompressible plasma, $\beta = 1$.

The results obtained above allow us to specify general expression (7) for the plasma pressure:

$$p = \frac{B_0^2}{8\pi}\left[\frac{1}{\cos^2\alpha} - \frac{R^4}{a^4}\left(1 + a'^2\frac{r^2}{a^2}\right)\right]$$
$$+ \left(\rho_0 u_0^2 - \frac{B_0^2}{4\pi}\right)\left[1 - R^2\tan\alpha\left(\frac{1}{a'a^2} + 2\int_0^z \frac{dz}{a^3}\right)\right], \qquad (9)$$

where we introduced the notation $B_0^2 = 4\pi\beta\rho_0 u_0^2$.

In order to derive the equation for the flow radius as a function of the longitudinal coordinate, we take into account the boundary condition for plasma pressure: $p(a, z) = 0$. As a result, from Eq. (9) we find the following first-order differential equation for the radius of the incompressible-plasma flow:

$$a'^2 = \frac{a^4}{b^4} - 1, \qquad (10)$$

where $b = R\sqrt{\cos\alpha}$. In the case of compressible plasma,

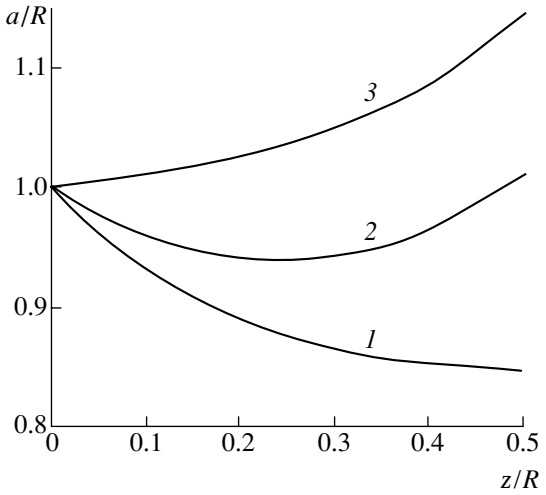

Flow radius as a function of the longitudinal coordinate.

we arrive at the second-order differential equation

$$aa''\left(a'^3 + \gamma\frac{a^2}{R^2}\right) = 2a'^3(1 + a'^2), \qquad (11)$$

where $\gamma = \left(1 - \frac{1}{\beta}\right)\tan\alpha$.

It is easy to solve Eq. (10) exactly. This allows us to find the radius of the incompressible-plasma flow as an explicit function of the longitudinal coordinate. For $\alpha < 0$, the flow radius initially decreases to the minimal value $a_{\min} = b$ corresponding to the longitudinal coordinate $z_{\min} = s = kbF(\arccos\sqrt{\cos\alpha}, k)$:

$$\frac{b}{a} = \mathrm{cn}\left(\frac{s - z}{kb}, k\right).$$

Here, $\mathrm{cn}(x, k)$ is the Jacobian elliptic function, $F(x, k)$ is the incomplete elliptical integral of the first kind, and $k = \frac{1}{\sqrt{2}}$. Furthermore, for $z > s$, the flow starts to expand:

$$\frac{b}{a} = \mathrm{cn}\left(\frac{z - s}{kb}, k\right). \qquad (12)$$

Expression (12) is valid provided that the values of the longitudinal coordinate are smaller than the critical value $z_k = s + kbK(k)$, where $K(k)$ is the complete elliptical integral of the first kind. As $z \longrightarrow z_k$, the flow radius increases without bound.

If $\alpha \geq 0$, a monotonic increase in the flow radius occurs:

$$\frac{b}{a} = \mathrm{cn}\left(\frac{z + s}{kb}, k\right).$$

This expression holds for $0 \leq z < kbK(k) - s$.

It should also be noted that expression (9) for the pressure of incompressible plasma can be written, with allowance for Eq. (10), in the form

$$p = \frac{1}{2}\rho_0 u_0^2 R^4\left(1-\frac{r^2}{a^2}\right)\left(\frac{1}{b^4}-\frac{1}{a^4}\right).$$

Using Eqs. (1), (5), and (10), we can prove that this result corresponds to the general form of the Euler equation for the steady flow of incompressible plasma at $\mathbf{B} = 2\sqrt{\pi\rho}\,\mathbf{V}$:

$$\mathrm{grad}\left(\frac{p}{\rho}+\frac{V^2}{2}\right) = 0.$$

Equation (11) can be solved by numerical methods. The calculation results for the flow radius are shown in the figure for various values of the parameters introduced above: (*1*) $\alpha = -0.7$, $\beta = 1.01$; (*2*) $\alpha = -0.5$, $\beta = 1$; and (*3*) $\alpha = 0.1$, $\beta = 1.1$.

As is seen from these results, in contrast to the case of incompressible plasma (curve *2*), the flow radius of compressible plasma (curves *1* and *3*) varies monotonically. This is due to the fact that expression (8) can only be used in the case of the nonvanishing derivative a'. Therefore, the behavior of the incompressible-plasma flow is determined by initial conditions. If $\alpha < 0$, the flow radius decreases, but the longitudinal flow velocity increases. On the other hand, if $\alpha > 0$, the flow radius increases, but the longitudinal flow velocity decreases.

From Eqs. (8) with regard to Eq. (11), we obtain the following expression for the derivative of the longitudinal flow velocity:

$$u' = 2\beta u_0 R^2\frac{a'^3(\gamma a^2 - a'R^2)}{a^3(\gamma a^2 + a'^3R^2)}.$$

This expression allows us to find the range of possible values of the parameter β for which the incompressible-plasma flows under consideration occur. Since

$$u_0' = \frac{2\beta u_0 \tan\alpha \sin^2\alpha}{R(\cos^2\alpha - \beta)},$$

the signs of the initial values for the derivatives of the flow radius and of the longitudinal flow velocity are opposite for $\beta > \cos^2\alpha$.

REFERENCES

1. L. I. Sedov, *Similarity and Dimensional Methods in Mechanics* (Nauka, Moscow, 1981; Academic, New York, 1959).
2. A. G. Kulikovskiĭ and G. A. Lyubimov, *The Magnetohydrodynamics* (Fizmatgiz, Moscow, 1962; Addison-Wesley, Reading, 1965).
3. N. D. Naumov, Dokl. Akad. Nauk **362**, 469 (1998) [Phys.–Dokl. **43**, 597 (1998)].

Translated by V. Chechin

Doklady Physics, Vol. 47, No. 7, 2002, pp. 495–498. Translated from Doklady Akademii Nauk, Vol. 385, No. 2, 2002, pp. 177–180.

PHYSICS

A Mathematical Model for Water–Vapor Phase Transitions in Geothermal Systems with Allowance for Capillary Forces

G. G. Tsypkin* and C. Calore**

Presented by Academician D.M. Klimov February 19, 2002

Received February 21, 2002

1. Capillary forces in geothermal reservoirs mainly affect heat-and-mass transfer processes in low-permeability domains with large gradients in the water content. In this respect, the problem on propagating a phase-transition front is representative, because capillary forces are maximal in this case. Such processes are of great importance for the operation of fractured collectors consisting of large-volume low-permeability blocks separated by cracks. The extraction of a heat-transfer agent from such a system causes a sharp pressure drop in the cracks, whose total void volume is small. As a result, the subsequent operation of the geothermal system is determined by the ability of the low-permeability blocks to vent the superheated vapor.

Numerical calculations of transport processes in geothermal systems containing equilibrium water–vapor mixtures were carried out in [1] with allowance for capillary forces. In the present paper, we formulate a new mathematical model of phase transitions which implies the existence of a sharp water–vapor interface at which capillary forces are present. Based on the derived analytical solution, we show that the capillary forces in a wetting medium stabilize the motion of the vaporization front. They prevent its destabilization and the origination of a mixed water–vapor domain. Moreover, they result in an increase in the yield of extracted vapor.

The approach based on the concept of a vaporization front was considered in studies [2–5], which were devoted to problems on phase transitions in geothermal systems.

2. We assume a geothermal reservoir to be an incompressible porous medium saturated with either water or vapor. In this case, the system of basic equations is determined by the laws of conservation of mass and energy, Darcy's law, the equation of state for vapor, and the thermodynamic relationships. Thus, in the water domain,

$$m\frac{\partial}{\partial t}\rho_w + \mathrm{div}\rho_w\mathbf{v}_w = 0, \quad \mathbf{v}_w = -\frac{k}{\mu_w}\mathrm{grad}P,$$

$$\frac{\partial}{\partial t}(\rho e)_1 + \mathrm{div}(\rho_w h_w \mathbf{v}_w) = \mathrm{div}(\lambda_1 \mathrm{grad}T),$$

$$\rho_w = \rho_{w0}(1 + \alpha(P - P_0) - \beta(T - T_0)),$$

$$dh_w = C_w dT + \frac{dP}{\rho_w}, \quad de_S = C_S dT, \quad e_w = h_w - \frac{P}{\rho_w},$$

$$\lambda_1 = m\lambda_w + (1-m)\lambda_S,$$

$$(\rho e)_1 = m\rho_w e_w + (1-m)\rho_S e_S.$$

Furthermore, in the vapor domain,

$$m\frac{\partial}{\partial t}\rho_v + \mathrm{div}\rho_v\mathbf{v}_v = 0, \quad \mathbf{v}_v = -\frac{k}{\mu_v}\mathrm{grad}P,$$

$$\frac{\partial}{\partial t}(\rho e)_2 + \mathrm{div}(\rho_v h_v \mathbf{v}_v) = \mathrm{div}(\lambda_2 \mathrm{grad}T),$$

$$P = \rho_v RT, \quad e_v = h_v - \frac{P}{\rho_v},$$

$$dh_v = C_P dT, \quad de_S = C_S dT,$$

$$\lambda_2 = m\lambda_v + (1-m)\lambda_S,$$

$$(\rho e)_2 = m\rho_v e_v + (1-m)\rho_S e_S.$$

Here, T is temperature; P is pressure; h is the enthalpy density; e is the energy density; v is the filtration rate; m is the porosity; k is the permeability coefficient; C is the specific heat; R is the gas constant; μ is the viscosity; ρ is the density; λ is the heat conductivity; α is the water compressibility coefficient; and β is the coefficient of thermal expansion for water. The subscripts w,

* *Institute of Problems in Mechanics, Russian Academy of Sciences, pr. Vernadskogo 101, Moscow, 117526 Russia*

** *Istituto di Geoscienze e Georisorse, Area della Ricerca CNR, Via G. Moruzzi, 1, 56124 Pisa, Italy*

1028-3358/02/4707-0495$22.00

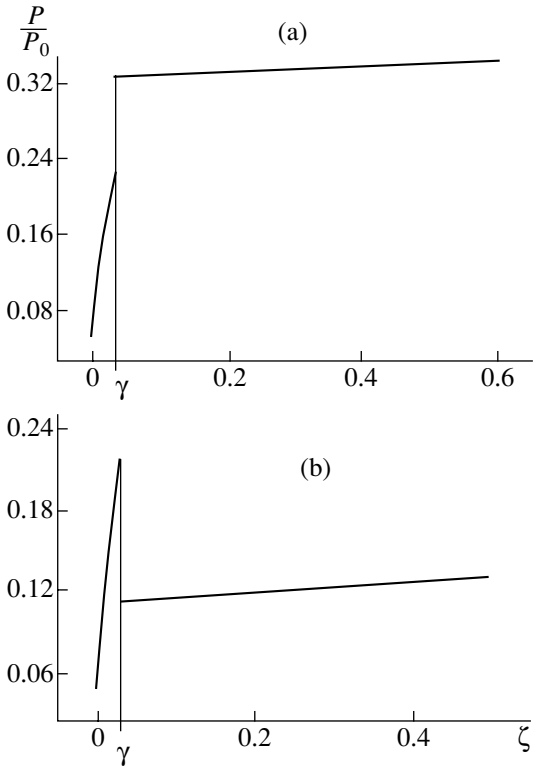

Fig. 1. Dimensionless pressure in the water and vapor domains with a pressure jump at the vaporization front in (a) a nonwettable medium with $\theta = 91°$, $T^* = 446.22$ K, $P_{v-} = 8.84 \times 10^5$ Pa, and $P_{w+} = 1.31 \times 10^6$ Pa and in (b) a wettable medium with $\theta = 89°$, $T^* = 445.87$ K, $P_{v-} = 8.73 \times 10^5$ Pa, and $P_{w+} = 4.49 \times 10^5$ Pa.

v, and S stand for water, vapor, and the skeleton of the porous medium, respectively.

The conditions of the local thermal equilibrium between phases imply that the relationships

$$T_+ = T_- = T_*, \quad P_{w+} = P_{v-} + P_c \tag{1}$$

must be satisfied at the vaporization front, where the capillary pressure P_c is determined by the Laplace formula

$$P_c = -\frac{2\sigma\cos\theta}{r}. \tag{2}$$

Here, σ is the surface tension, θ is the wetting angle, and r is the capillary radius. For a porous medium, representative values of the last quantity are given by the formula $r = \sqrt{\frac{k}{m}}$. In the case of a low-permeability porous medium, the liquid pressure was estimated to differ significantly from the vapor pressure even when the wetting angle is small. In addition, the capillary pressure drops as the permeability coefficient increases.

A decrease in the saturation vapor pressure at a curved surface (meniscus) is an extra effect determining the phase-transition conditions. This decrease is given by the Kelvin formula

$$P_{v-} = P_* \exp\left(-\frac{2\sigma V_w}{rR_0T}\right).$$

Here, R_0 is the universal gas constant, V_w is the molar water volume, and P_* is the flat-surface pressure. The Clapeyron equilibrium curve for a water–vapor mixture with allowance for the Kelvin correction can be presented in the form

$$P_{v-} = P_a \exp\left(A + \frac{B}{T_*} - \frac{2\sigma V_w}{rR_0T_*}\right),$$

$$A = 12.512, \quad B = 4611.73.$$

This equation, together with Eqs. (1) and (2) and the laws of conservation of mass and energy, composes a complete system of boundary conditions at the phase-transition front with allowance for capillary forces. The laws of conservation of mass and energy take the form

$$m\left(1 - \frac{P_{v-}}{\rho_w RT_*}\right)V_n = \frac{kP_{v-}}{\mu_v\rho_w RT_*}(\mathrm{grad}P)_{n-} - \frac{k}{\mu_w}(\mathrm{grad}P)_{n+},$$

$$mq\rho_w V_n = (\lambda\mathrm{grad}T)_{n+} - (\lambda\mathrm{grad}T)_{n-} - q\rho_w\frac{k}{\mu_w}(\mathrm{grad}P)_{n+}.$$

Here, V is the front velocity and q is the specific heat of vaporization. The index n stands for the normal component. The subscripts plus, minus, and asterisk imply that the quantities are to be taken, respectively, on the right and left sides of the front and directly at the front.

3. For simplicity, we now consider a one-dimensional problem of the vapor extraction from a water-saturated hydrothermal permeable reservoir occupying the half-space $x > 0$ and contacting impermeable rocks at the fixed boundary $x = 0$. At the initial state, the stratum pressure is P_0 and the temperature is T_0. We assume that, at the boundary $x = 0$, which represents a fracture, the pressure P^0 decreases to a value lower than the pressure of the phase transition at the initial temperature. In this case, a vaporization front between the water and vapor domains propagates to the right.

We now restrict our analysis to the case of sufficiently small values of the permeability coefficient and

ignore small quantities. Thus, we arrive at the following system of basic equations: in the water domain,

$$\frac{\partial P}{\partial t} - \frac{\beta}{\alpha}\frac{\partial T}{\partial t} = \frac{k}{m\alpha\mu_w}\frac{\partial^2 P}{\partial x^2}, \quad \frac{\partial T}{\partial t} = a_1\frac{\partial^2 T}{\partial x^2}$$

and in the vapor domain,

$$-\left(\frac{\partial P}{\partial x}\right)^2 = P\frac{\partial^2 P}{\partial x^2}, \quad \frac{\partial T}{\partial t} = a_1\frac{\partial^2 T}{\partial x^2}.$$

Let the initial and boundary values of both the temperature and pressure be constant. In this case, the problem has the self-similar solution

$$T = T(\zeta), \quad P = P(\zeta), \quad \xi = \frac{x}{2\sqrt{a_1 t}}, \quad X(t) = 2\gamma\sqrt{a_1 t}.$$

In both the domains, the solutions can be expressed in terms of probability integrals. Substituting the solutions into the system of boundary conditions at the vaporization front, we arrive at a system of transcendental equations for determining the front velocity, the phase-transition temperature, and the pressure on both sides of the interface.

4. We numerically solved the system of transcendental equations at the moving boundary for representative values of the basic physical parameters with $T_0 = 450$ K, $P_0 = 4 \times 10^6$ Pa, $P_0 = 2 \times 10^5$ Pa, $k = 0.5 \times 10^{-17}$ m^2, and $m = 0.1$. Examples of the calculation results for the pressure in the water and vapor domains are shown in Fig. 1 for (a) nonwettable and (b) wettable media. As is seen, a pressure jump occurs at the front. In the first case, the liquid pressure exceeds the vapor pressure; in the second case, the situation is the reverse.

There exist two different regimes of vapor extraction. In the case of a wettable medium, which is illustrated in Fig. 2, temperature curve (*1*) is at a conventional position with respect to phase-transition temperature curve (*2*); i.e., the temperature curve in the water domain is situated lower than the vaporization-temperature curve. At larger values of the permeability coefficient and of the wetting angle, the curves change their positions. The temperature in the water domain becomes higher than the vaporization temperature. From the physical standpoint, this corresponds to the superheating of the liquid phase. This fact can be treated as an instability in the phase-transition front (which is usually referred to as a morphological instability) resulting in the formation of a two-phase water–vapor domain between the water and vapor domains. For example, this effect manifests itself in the case of the parameters taken in Fig. 2 but for values of the wetting angle corresponding to either neutral or nonwettable media ($\theta \geq 90°$). Therefore, the capillary pressure stabilizes and destabilizes the phase-transition front in wettable and nonwettable media, respectively.

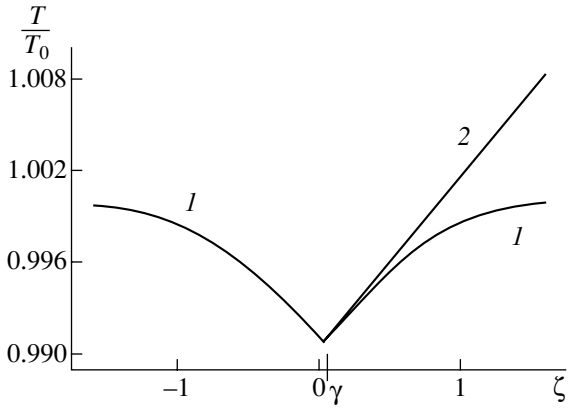

Fig. 2. (*1*) Dimensionless temperature and (*2*) phase-transition temperature for a wettable porous medium with $P_0 = 1.5 \times 10^5$ Pa, $k = 0.7 \times 10^{-17}$ m^2, and $P_0 = 3 \times 10^5$ Pa.

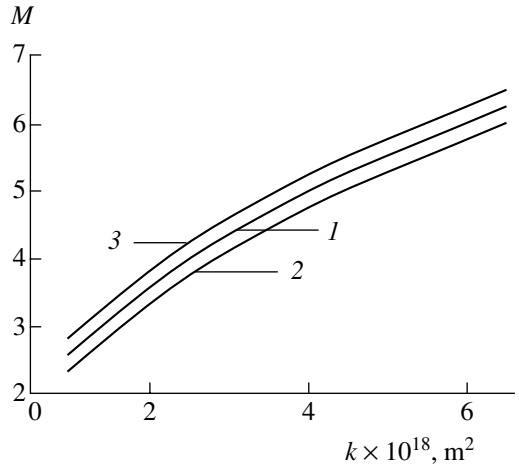

Fig. 3. Mass of extracted vapor as a function of the permeability coefficient at various wetting angles for (*1*) neutral ($\theta = 90°$), (*2*) nonwettable ($\theta = 91°$), and (*3*) wettable ($\theta = 89°$) media.

The mass of extracted vapor, which is an important characteristic of the process, can be presented as

$$M = m\int_0^\infty \rho_{w0}\,d\zeta - m\int_\gamma^\infty \rho_w(\zeta)\,d\zeta$$
$$= m\rho_{w0}\left[\gamma + \int_\gamma^\infty \left(1 - \frac{\rho_w}{\rho_{w0}}\right)d\zeta\right].$$

This quantity is composed of the two terms describing the contributions due to both the motion of the phase-transition front and the expansion of liquid caused by

the pressure drop. The front velocity decreases with increasing initial pressure and permeability coefficient. Curves for the mass of the extracted heat-transfer agent are presented in Fig. 3 for (*1*) neutral, (*2*) nonwettable, and (*3*) wettable media. As is seen, a decrease in the wetting angle results in an increase in the vapor yield. This fact can be explained by a pressure drop at the front in the water domain. The drop results in an increase in the pressure gradient and, consequently, the mass flux towards the front. In contrast, in the case of a nonwettable medium, the water pressure at the vaporization front increases, which is accompanied by a reduction of the amount of the extracted heat-transfer agent.

REFERENCES

1. K. Pruess and M. O'Sullivan, in *Proceedings of VII Workshop on Geothermal Reservoirs Engineering, Stanford, 1992*, pp. 165–174.
2. S. K. Garg and J. W. Pritchett, Water Resource Res **24,** 843 (1988).
3. K. Pruess, C. Calore, R. Celati, and Y. S. Wu, Int. J. Heat Mass Transf. **30**, 2595 (1987).
4. A. W. Woods and S. D. Fitzgerald, J. Fluid Mech. **251,** 563 (1993).
5. G. G. Tsypkin, Dokl. Akad. Nauk **337**, 748 (1994) [Phys.–Dokl. **39**, 594 (1994)].

Translated by V. Chechin

Doklady Physics, Vol. 47, No. 7, 2002, pp. 499–503. Translated from Doklady Akademii Nauk, Vol. 385, No. 3, 2002, pp. 323–327.

PHYSICS

Scaling Properties of a Two-Phase Zone in Directed Crystallization

D. V. Alexandrov and A. O. Ivanov

Presented by Academician N.A. Vatolin February 18, 2002

Received March 6, 2002

A wealth of physical, mechanical, and chemical processes associated with phase and chemical transitions are conventionally described on the basis of the Stefan classical frontal model. The evaporation of liquids, the growth of a new phase in a metastable medium, frontal burning or frontal chemical reactions, the filtration displacement of viscous fluids in porous substances, etc., are among them. In many cases, a locally flat shape of the front separating two phases is violated, and a transient domain containing elements of both phases is formed. In this two-phase domain, the interface often represents a strongly branched structure having the properties of the scale–time self-similarity. Its known manifestations are growing dendrites, clouds, fractal clusters, hydrodynamic viscous "fingers" in porous media, and chemical reactions in turbulent flows [1–4]. The listed objects are natural examples of so-called fractal formations [1] whose self-similarity and scale–time invariance are described by a scaling power dependence with a fractional exponent called the fractal dimensionality.

Among many phenomena of phase transitions, the processes of directed crystallization of multicomponent melts and solutions used for producing pure crystals or alloys with desired properties play an important applied role. In a solidifying melt, an impurity often precipitates intensely from the crystal bulk. If this process is characterized by a strong dependence of the phase-transition temperature of the crystallizing liquid on the available impurity concentration, a metastable domain, the so-called zone of concentrational (constitutional) supercooling, arises ahead of the solidification front [5]. The temperature of the multicomponent melt in this zone is lower than its solidification temperature, a condition which leads to the appearance in this domain of the elements of a new phase in the form of dendrites, crystallites, etc. As a result, the solid and liquid phases are separated by the two-phase zone.

Ural State University,
pr. Lenina 51, Yekaterinburg, 620083 Russia

It is natural that the presence of the two-phase zone principally changes the pattern of the process. For this reason, this phenomenon is actively investigated (see, e.g., [6–13]). However, the hypothesis regarding the possible self-similar fractal structure of the two-phase zone has been poorly studied until now. Among the sparse investigations in this field, we find study [11], in which the effect of fractal dimensionality on the parameters of the self-similar solidification mode was investigated by using the heuristically introduced fractal-like spatial density distribution in the two-phase zone. Until now, only asymptotic approximate solutions to equations of heat and mass transfer in the two-phase zone were known [7, 8].

This study is based on the exact analytical solutions recently obtained [12, 13] to the model proposed for the quasi-equilibrium two-phase zone in [14], where it was shown that supercooling in the developed two-phase zone is almost completely eliminated due to intense heat release by growing elements of the solid phase. Here, we show that the distributions of an impurity and a volume solid-phase fraction in the quasi-equilibrium two-phase zone are described by scaling-power spatial dependences with a fractional exponent. This scaling dimensionality depends on the thermal properties of a melt and is invariant with respect to the operational parameters governing solidification. In other words, this exponent is a universal characteristic for each melt. The presented experimental data [15] corroborate the conclusion that the scaling exponent holds in the time evolution of the two-phase zone. This result makes it possible to formulate the concept of the fractal structure of the two-phase zone.

We consider the process of the directed solidification of a binary melt along the ξ axis, with the two-phase zone in thermodynamic equilibrium. We assume that the process proceeds with a constant rate u_s, and the distributions $\sigma_m(\xi)$, $\theta_m(\xi)$, and $\varphi(\xi)$ of an impurity, temperature, and the volume fraction of the solid phase, respectively, attain steady-state values in the two-phase zone $u_s\tau < \xi < u_s\tau + \delta$ (here, τ is the time and δ is the length of the two-phase zone). The heat and mass trans-

1028-3358/02/4707-0499$22.00

fer in the two-phase zone are described by the heat equation and impurity diffusion equation

$$\frac{\partial}{\partial\tau}[\rho_m C_m\theta_m] = \frac{\partial}{\partial\xi}\left(\lambda_m\frac{\partial\theta_m}{\partial\xi}\right) + L_V\frac{\partial\varphi}{\partial\tau}, \quad (1)$$

$$\frac{\partial}{\partial\tau}[(1-\varphi)\sigma_m] = \frac{\partial}{\partial\xi}\left(D_m\frac{\partial\sigma_m}{\partial\xi}\right) - k\sigma_m\frac{\partial\varphi}{\partial\tau}, \quad (2)$$

where k is the equilibrium coefficient of impurity distribution and L_V is the latent solidification heat. The effective transport coefficients D_m, ρ_m, C_m, and λ_m in the two-phase zone depend on the volume fraction of the solid component φ:

$$\begin{aligned} D_m(\varphi) &= D_l(1-\varphi), \\ \rho_m(\varphi)C_m(\varphi) &= \rho_l C_l(1-\varphi) + \rho_s C_s\varphi, \\ \lambda_m(\varphi) &= \lambda_l(1-\varphi) + \lambda_s\varphi. \end{aligned} \quad (3)$$

Here, D_l is the diffusivity of an impurity in the liquid phase (diffusion in the solid phase is conventionally neglected); and ρ_l and ρ_s, C_l and C_s, and λ_l and λ_s are the densities, heat capacities, and thermal conductivities of the liquid and solid phases, respectively. The temperature in the two-phase domain is determined through an impurity concentration from the liquidus equation. In the case of a low impurity content, this dependence is linear:

$$\theta_m(x) = \theta_0 - m\sigma_m(x), \quad (4)$$

where θ_0 is the phase-transition temperature for a pure melt and m is the liquidus slope determined from the binary-system phase diagram. At the solid-phase–two-phase-zone interface $\xi = \Sigma(\tau)$ and two-phase-zone–melt interface $\xi = \Sigma(\tau) + \delta(\tau)$, the following conditions of heat and mass balance are satisfied:

$$\begin{aligned} \varphi = \varphi_\star, \quad \lambda_s\frac{\partial\theta_s}{\partial\xi} - \lambda_m\frac{\partial\theta_m}{\partial\xi} &= L_V(1-\varphi_\star)\frac{d\Sigma}{d\tau}, \\ \xi &= \Sigma(\tau); \end{aligned} \quad (5)$$

$$(1-k)(1-\varphi_\star)\sigma_m\frac{d\Sigma}{d\tau} + D_m\frac{\partial\sigma_m}{\partial\xi} = 0, \quad \xi = \Sigma(\tau); \quad (6)$$

$$\begin{aligned} \varphi = 0, \quad \sigma = \sigma_l, \quad D_m\frac{\partial\sigma_m}{\partial\xi} &= D_l\frac{\partial\sigma_l}{\partial\xi}, \\ \frac{\partial\theta_m}{\partial\xi} = g_l, \quad \xi &= \Sigma(\tau) + \delta(\tau), \end{aligned} \quad (7)$$

where $\varphi_\star$ is the volume fraction of the solid phase at the crystal–two-phase-zone interface. The melt solidification with a constant rate u_s can be realized only when the phase interfaces are far from the walls of an ingot mold. In this case, it is possible to consider the temperature gradients g_l and g_s as constant at the two-phase-zone interfaces.

In [12], the exact analytical solution to model (1)–(7) for the quasi-steady solidification process (steady in the reference frame $x = \dfrac{(\xi - u_s\tau)u_s}{D_l}$ connected with the moving zone) is constructed for crystallization in a field of fixed temperature gradients g_s and g_l in the solid and liquid phases, respectively. In this case, the classical diffusion equation was used for the melt, and the impurity concentration $\sigma_{l\infty}$ far from the zone was considered as known. The method developed in [12, 13] is based on the elimination of the temperature field by using Eq. (4) and on the integration with respect to a new variable—the volume fraction of the solid phase. Here, we present only the final result. The impurity concentration depends explicitly only on the volume fraction of the solid phase and has the form

$$\begin{aligned} \sigma_m(\varphi) = \sigma_{l\infty}(1 + G_l - J(\varphi))&\frac{N_1\Lambda_1 - 1}{[1-\varphi-M_2(\varphi)]N_1\Lambda_1} \\ &\times\exp\left[-k\int_0^\varphi\frac{dz}{1-z-M_2(z)}\right], \end{aligned} \quad (8)$$

$$J(\varphi) = \frac{N_1\Lambda_1}{N_1\Lambda_1 - 1}\int_0^\varphi\exp\left[k\int_0^\alpha\frac{dy}{1-y-M_2(y)}\right]\frac{dM_1}{d\alpha}d\alpha.$$

The volume fraction of the solid phase φ and the dimensionless thickness of the two-phase zone ε are determined from the relationships

$$x(\varphi) = \varepsilon + N_1\int_0^\varphi\frac{\Lambda_0(z)\dfrac{dc_m}{dz}}{h(z)(p_0 - c_m(z)) - N_2 z + B}dz, \quad (9)$$

$$\begin{aligned} \varepsilon &= -N_1\int_0^{\varphi_\star}\frac{\Lambda_0(z)\dfrac{dc_m}{dz}}{h(z)(p_0 - c_m(z)) - N_2 z + B}dz, \\ \varepsilon &= \frac{u_s}{D_l}\delta. \end{aligned} \quad (10)$$

Here, the dimensionless variables and parameters have the form

$$h(\varphi) = \frac{\rho_m(\varphi)C_m(\varphi)}{\rho_l C_l}, \quad \Lambda_0(\varphi) = \frac{\lambda_m(\varphi)}{\lambda_s},$$

$$p_0 = \frac{\theta_0}{m\sigma_{l\infty}},$$

$$D_0(\varphi) = \frac{D_m(\varphi)}{D_l}, \quad N_1 = \frac{\lambda_s}{D_l\rho_l C_l}, \quad N_2 = \frac{L}{C_l m\sigma_{l\infty}},$$

$$G_l = \frac{D_l g_l}{m\sigma_{l\infty}u_s},$$

$$M_1(\varphi) = \frac{D_0(\varphi)[h(\varphi)p_0 - N_2\varphi + B]}{N_1\Lambda_0(\varphi)},$$

$$M_2(\varphi) = \frac{D_0(\varphi)h(\varphi)}{N_1\Lambda_0(\varphi)}, \quad c_m = \frac{\sigma_m}{\sigma_{l\infty}},$$

$$B = 1 + G_l - p_0 - N_1\Lambda_1 G_l, \quad \Lambda_1 = \frac{\lambda_l}{\lambda_s},$$

and the solidification rate u_s and the volume fraction of the solid phase $\varphi_\star$ are determined from the following set of equations:

$$u_s = \frac{\lambda_s g_s - \lambda_l g_l}{\rho_l L + \rho_l C_l m\sigma_{l\infty}[(p_0 - c_m|_{x=\varepsilon})h(0) - (p_0 - c_m|_{x=0})h(\varphi_\star)]},$$

$$(1-k)(1-\varphi_\star)c_m(\varphi_\star) + \frac{D_0(\varphi_\star)[h(\varphi_\star)(p_0 - c_m(\varphi_\star)) - N_2\varphi_\star + B]}{N_1\Lambda_0(\varphi_\star)} = 0.$$

Analytical solutions (8)–(10) were experimentally well corroborated in [10], where it was shown that the impurity concentration and, therefore, the temperature are functions of only one variable φ (see also Fig. 1 in [10]). In addition, it was shown in [12] that the extension of the two-phase zone as well as the volume fraction of the solid phase or the impurity concentration in the two-phase zone changes self-similarly when the operational parameters of the process, i.e., the temperature gradients controlling solidification, are varied. This behavior of unknown functions implies that the zone of concentrational supercooling has a fractal structure. It is well known that many natural fractal-like objects can be described by scale-invariant fractals (see, e.g., [2]). In view of this circumstance, we try to study the two-phase zone by introducing certain power dependences. We describe the distribution of the volume fraction of the solid phase and the impurity concentration in the two-phase zone by homogeneous self-similar functions

$$\varphi(y) = \varphi_\star y^D, \quad y = 1 - \frac{x}{\varepsilon}, \tag{11}$$

$$\sigma_m(y) = \sigma_\varepsilon + (\sigma_\star - \sigma_\varepsilon)y^D, \tag{12}$$

satisfying the scaling relationships

$$\varphi(\lambda y) = \lambda^D\varphi(y), \quad \sigma_m(\lambda y) - \sigma_\varepsilon = \lambda^D(\sigma_m(y) - \sigma_\varepsilon).$$

Here, $\sigma_\star$ is the impurity concentration at the interface between the solid phase and two-phase zone, σ_ε is the impurity concentration at the interface between the two-phase zone and the melt, and ε is the length of the two-phase zone. The scaling parameter D, which is the exponent in spatial distributions (11) and (12), plays the role of the dimensionality of fractal objects [2]. If fractal-like scaling spatial dependences (11) and (12) accurately approximate exact analytical solutions (8)–(10), this fact testifies to the fractal structure of the two-phase zone. As is easily seen, σ_ε in Eq. (12) is the nonfractal section of the function $\sigma_m(x)$. In other words, the impurity distribution $\sigma_m(x)$ near the two-phase-zone–melt interface is not fractal, because virtually no displacement of impurities into the melt at this interface takes place.

In Fig. 1, it is possible to compare the exact solution to model (1)–(7) with Eqs. (8)–(10) and power dependences (11) and (12) for an iron–nickel alloy with the following thermal and physical characteristics: λ_l = 0.1 cal/(cm s °C), λ_s = 0.177 cal/(cm s °C), ρ_l = 7 g/cm^3, ρ_s = 7.8 g/cm^3, $D_L = 1.0 \times 10^{-5}$ cm^2/s, C_s = 0.057 cal/(g °C), C_l = 0.102 cal/g °C, m = 2.65°C, L_V = 3786.6 cal/cm^3, and θ_0 = 1529.5°C.

The good agreement between the scaling dependences and the analytical solution corroborates the hypothesis about the fractal-like structure of the whole two-phase zone. We emphasize that, according to Eqs. (11) and (12), the volume fraction and the impurity concentration inside the zone are determined only by their values at its interfaces and are independent of the scaling parameter, which is $D = 1.37 \pm 0.05$ for all the curves in Fig. 1. Small variations in the impurity-distribution coefficient strongly influence the scaling parameter D. Figure 2 shows the coefficient D as a function of the initial impurity concentration $\sigma_{l\infty}$ in the melt for various values of the equilibrium distribution coefficient k. As this concentration increases, the dependence becomes almost linear, whereas, with decreasing $\sigma_{l\infty}$, nonlinearity appears, because $D \longrightarrow 1$

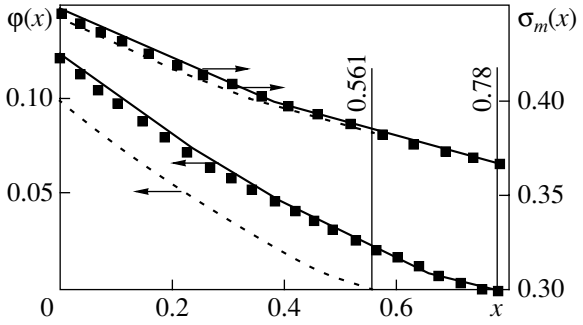

Fig. 1. Volume fraction of the solid phase $\varphi(x)$ and impurity concentration $\sigma_m(x)$ for a Fe–Ni alloy at temperature gradients g_l = 20°C/cm and g_s = 120°C/cm ($\varphi_\star$ = 0.123) and g_s = 100°C/cm ($\varphi_\star$ = 0.097) according to the exact analytical solutions from data [12]. Solid and dashed curves are the dependences corresponding to fractal-like distributions (11) and (12). The vertical straight lines are the boundaries of the dimensionless length ε of the two-phase zone for k = 0.68.

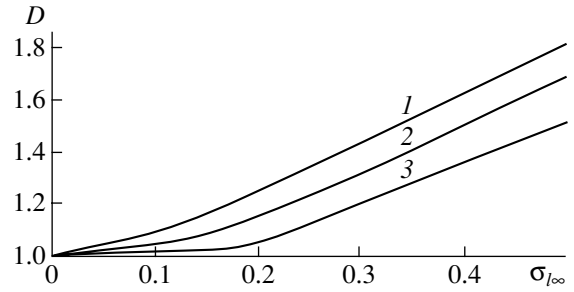

Fig. 2. Scaling exponent D vs. the impurity concentration $\sigma_{l\infty}$ in melt far from the two-phase zone for k = (*1*) 0.63, (*2*) 0.68, and (*3*) 0.73.

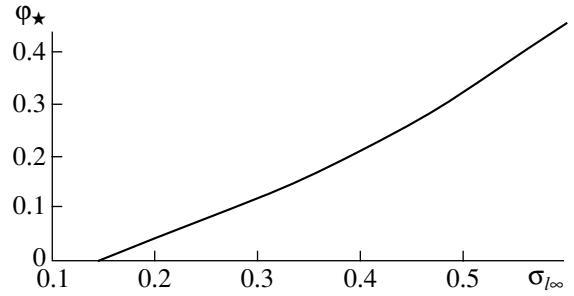

Fig. 3. Volume fraction of the solid phase $\varphi_\star$ vs. the impurity concentration $\sigma_{l\infty}$ in melt far from the two-phase zone for k = 0.68.

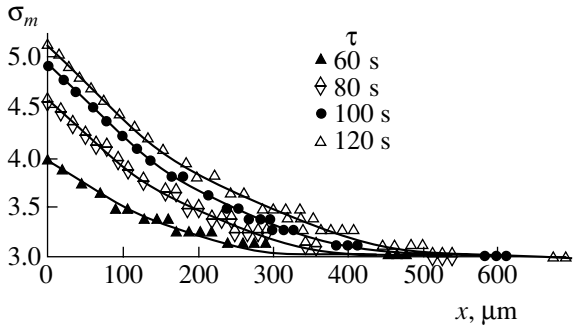

Fig. 4. Fractal-like law (12) and experimental data [15] for the two-phase zone developing in time.

for small $\sigma_{l\infty}$. The last property can be shown by means of the asymptotic expansions of integral relationships for small $\varphi_\star$ values ($0 \le \varphi < \varphi_\star \ll 1$). We substitute the following approximations for $\varphi_\star \to 0$ into Eqs. (8)–(10):

$$D_0(\varphi) \sim 1, \quad h(\varphi) \sim 1, \quad \Lambda_0(\varphi) \sim \Lambda_1,$$
$$1 - \varphi \gg M_2(\varphi), \quad M_1(\varphi) \sim G_l(\varphi - 1),$$
$$B \sim -p_0 - N_1\Lambda_1 G_l.$$

We obtain

$$\sigma_m(\varphi) \simeq \sigma_{l\infty} \times \left[1 + G_l + \frac{G_l}{1-k}((1-\varphi)^{1-k} - 1)\right](1-\varphi)^{k-1}, \quad (13)$$

$$1 - \frac{x}{\varepsilon} \simeq \frac{1}{G_l\sigma_{l\infty}\varepsilon}(\sigma_m(\varphi) - \sigma_m(0)), \quad (14)$$

$$\varepsilon \simeq \frac{1}{G_l\sigma_{l\infty}}[\sigma_m(\varphi_\star) - \sigma_m(0)]. \quad (15)$$

Expanding Eq. (13) into a series in φ, we have

$$\sigma_m(\varphi) \simeq \sigma_{l\infty}\left[1 + G_l + \left(1 + G_l - \frac{G_l}{1-k}\right)(1-k)\varphi\right]. \quad (16)$$

Further, combining Eqs. (14)–(16), we obtain

$$\frac{1}{\varepsilon G_l}\left(1 + G_l - \frac{G_l}{1-k}\right)(1-k)\varphi \simeq 1 - \frac{x}{\varepsilon},$$

$$\frac{1}{\varepsilon G_l}\left(1 + G_l - \frac{G_l}{1-k}\right)(1-k) \simeq \frac{1}{\varphi_\star},$$

which indicates that

$$\varphi \simeq \varphi_\star\left(1 - \frac{x}{\varepsilon}\right), \quad \varphi_\star \to 0. \quad (17)$$

Now, approximate expression (16) can be represented as

$$\sigma_m(\varphi) \simeq \sigma_{l\infty}\left[1 + G_l + \varepsilon G_l\frac{\varphi}{\varphi_\star}\right]. \quad (18)$$

Taking into account that

$$\sigma_m(0) \equiv \sigma_\varepsilon \simeq \sigma_{l\infty}(1 + G_l),$$
$$\sigma_m(\varphi_\star) \equiv \sigma_\star \simeq \sigma_{l\infty}[1 + G_l + \varepsilon G_l],$$

we obtain from Eq. (18)

$$\sigma_m(\varphi) \simeq \sigma_\varepsilon + (\sigma_\star - \sigma_\varepsilon)\frac{\varphi}{\varphi_\star} = \sigma_\varepsilon + (\sigma_\star - \sigma_\varepsilon)\left(1 - \frac{x}{\varepsilon}\right). \quad (19)$$

Further, the comparison of Eqs. (11), (12) and (17), (19) indicates that the similarity coefficient $D \to 1$ for the limiting case $\varphi_\star \ll 1$. In Fig. 3, where the solid-phase volume fraction is shown as a function of the impurity concentration at infinity for an iron–nickel alloy, it is seen that the inequality $\varphi \ll 1$ is valid for small $\sigma_{l\infty}$. Therefore, the tendency of the scaling coefficient to unity for small initial impurity concentrations can be considered as justified by the model.

Analyzing Figs. 1–3, we generally conclude that universal scaling dependences (11) and (12) coincide with exact analytical solutions (8)–(10) when the exponent D takes fractional values different from the space dimensionality. Thus, this result makes it possible to interpret the quasi-equilibrium two-phase zone as a fractal-like object in the context of the solidification mode being considered [model (1)–(7)].

The natural question arises of whether or not this property holds during the evolution of the two-phase

zone. Figure 4 shows the impurity concentration ahead of the interface between the solid phase and two-phase zone ($x = 0$; here, x and ε play the role of dimensional variables) for a KCl water solution crystallizing in unsteady conditions according to data [15]. At times $\tau > 60$ s after the onset of solidification, concentrational supercooling ahead of the plane front leads to the appearance of a metastable region; i.e., the two-phase zone is formed. As is seen in Fig. 4, the concentration profile tends to a certain steady value as the crystallization time increases (in other words, spacing between the impurity-concentration distributions decreases with time). Nevertheless, even at stages of crystallization with unestablished characteristics of the two-phase zone, Eq. (12) accurately describes the experimental curves. The scaling parameter for this system is $D \approx 2.7$ for all the curves in Fig. 4 obtained by the authors of [15] for various moments of time. In fact, these experimental data corroborate the proposed hypothesis about the fractal structure of the two-phase zone in the process of its development with the constant scaling exponent D.

The above results make it possible to conclude that the structure of the two-phase zone follows universal fractal–scaling regularities.

ACKNOWLEDGMENTS

This work was supported by the Russian Foundation for Basic Research, project nos. 01-02-96430 Ural and 02-03-96437 Ural; by the Ministry of Education of the Russian Federation, project no. E00-3.2-210; and by the US Civilian Research and Development Foundation for the Independent States of the Former Soviet Union, grant no. REC-005.

REFERENCES

1. B. B. Mandelbrot, *The Fractal Geometry of Nature* (Freeman, New York, 1982).
2. J. Feder, *Fractals* (Plenum, New York, 1988; Mir, Moscow, 1991).
3. B. M. Smirnov, *Physics of Fractal Clusters* (Nauka, Moscow, 1991).
4. T. Vicsek, *Fractal Growth Phenomena* (World Sci., Singapore, 1989).
5. G. P. Ivantsov, Dokl. Akad. Nauk SSSR **81**, 179 (1951).
6. Yu. A. Buyevich, D. V. Alexandrov, and V. V. Mansurov, *Macrokinetics of Crystallization* (Begell House, New York, 2001).
7. R. N. Hills, D. E. Loper, and P. H. Roberts, Q. J. Mech. Appl. Math. **36**, 505 (1983).
8. A. C. Fowler, IMA J. Appl. Math. **35**, 159 (1985).
9. D. M. Anderson and M. G. Worster, J. Fluid Mech. **302**, 307 (1995).
10. M. Czapelski, J. Cryst. Growth **187**, 138 (1998).
11. D. V. Alexandrov, A. O. Ivanov, and M. E. Komarovski, Int. J. Fluid Mech. Res. **26** (2), 224 (1999).
12. D. V. Alexandrov, Acta Mater. **49**, 759 (2001).
13. D. V. Alexandrov, J. Cryst. Growth **222**, 816 (2001).
14. V. T. Borisov, *Theory of the Two-Phase Zone of a Metallic Ingot* (Metallurgiya, Moscow, 1987).
15. K. Nagashima and Y. Furukawa, J. Cryst. Growth **209**, 167 (2000).

Translated by V. Bukhanov

Doklady Physics, Vol. 47, No. 7, 2002, pp. 504–506. Translated from Doklady Akademii Nauk, Vol. 385, No. 1, 2002, pp. 51–53.

TECHNICAL PHYSICS

Electrodynamics of Ultra-Wideband Short-Pulse Processes in Irregular Transmission Lines

M. N. Golikov, V. I. Koroza, and Academician V. N. Mikhaĭlov

Received February 12, 2002

Owing to an increasing interest in the investigations of electrodynamics of transient and pulse processes in irregular transmission lines, including the propagation of ultra-wideband electromagnetic pulses (UWB EMPs) [1] in these lines, new problems arise in waveguide electrodynamics. Models developed for the numerical investigation of monochromatic ($\sim e^{-i\omega t}$) processes are virtually inapplicable to UWB EMPs, because the numerical inversion of Fourier integrals of the monochromatic components of a UWB EMP field which are also numerically obtained in irregular waveguides cannot provide satisfactory accuracy, and the accuracy cannot be checked due to the very wide frequency spectra. This fact forces us to abandon the frequency representations and to develop new, more general calculation methods providing a high accuracy and the possibility of error checking.

In this paper, we present the results of investigating the capabilities of the variational method for solving time-dependent waveguide equations with the example of a planar waveguide in the form of an irregular layer. We use the Cartesian coordinate system, where the y-axis is directed across the waveguide layer under consideration and the z-axis coincides with the direction of wave propagation inside the layer. This layer is sandwiched between perfectly conducting bodies whose boundaries are $y = -a_1(z)$ and $y = a_2(z)$, where $a_1(z)$ and $a_2(z)$ are continuous functions such that $a_1(z) \geq 0$ and $a_2(z) \geq 0$ and they do not simultaneously vanish. Therefore, the layer width is nonzero for arbitrary z: $\Delta(z) = a_1(z) + a_2(z) > 0$. It is also assumed that $a_1(z) = a_{10} = \text{const}$ and $a_2(z) = a_{20} = \text{const}$ for $z < 0$, so that its width in the half-layer $z < 0$ is $\Delta(z) = a_{10} + a_{20} = \Delta_0 = \text{const}$. The shape and parameters of the layer, as well as the wave field components, are assumed to be independent of the x coordinate.

We introduce dimensionless quantities by dividing all the length-dimension quantities (coordinates $a_1(z)$, $a_2(z)$, etc.) by a certain convenient linear scale L and time by $\frac{L}{c}$ (c is the speed of light in vacuum). The designations for the dimensionless variables are the same.

Let a pulse of the transverse electromagnetic (TEM) structure propagate from the regular half-layer ($z < 0$) towards its irregular section. As the pulse attains the irregular section of the layer, it is not only partially reflected, but also transformed into transverse-magnetic (TM) modes.

Applying a variational method similar to [2], we decompose the only magnetic-field component (directed along the x-axis) in the modes of the comparison waveguides

$$H(y, z, t) = \sum e_j(y, z) f_j(z, t), \tag{1}$$

where $f_j(z, t)$, $j = 1, 2, \ldots$ are unknown amplitudes and $e_j(y, z) = \cos\left[\pi(j-1)\frac{a_1(z) + y}{\Delta(z)}\right]$ are the basis functions for planar waveguides. In this case, the amplitude $f_1(z, t)$ corresponds to the magnetic field of the TEM mode, whereas the remaining amplitudes $f_j(z, t)$, $j \geq 2$ correspond to the TM-mode magnetic fields ($E_{0\,j-1}$ waves). The set of time-dependent waveguide equations in the matrix designations coincides in form with Eq. (7) from [2]:

$$\frac{\partial}{\partial z}\left[G(z)\frac{\partial \mathbf{f}}{\partial z} + Q(z)\mathbf{f}\right] - Q^{\tau}(z)\frac{\partial \mathbf{f}}{\partial z} - P(z)\mathbf{f} - T(z)\frac{\partial^2 \mathbf{f}}{\partial t^2} = 0, \tag{2}$$

where $\mathbf{f}(z, t)$ is the unknown column vector whose components are the amplitudes $f_j(z, t)$ and the matrix coefficients $G(z)$, $Q(z)$, $P(z)$, and $T(z)$ are determined by their elements

$$G_{ij} = \int_{-a_1(z)}^{a_2(z)} \varepsilon^{-1} e_j e_i dy, \quad T_{ij} = \int_{-a_1(z)}^{a_2(z)} \mu e_j e_i dy,$$

$$Q_{ij} = \int_{-a_1(z)}^{a_2(z)} \varepsilon^{-1} (e_j)_z e_i dy,$$

State Institute of Strategic Stability Ministry of Atomic Energy, Moscow, Russia

1028-3358/02/4707-0504$22.00

$$P_{ij} = \int_{-a_1(z)}^{a_2(z)} \varepsilon^{-1}\{(e_j)_z(e_i)_z + (e_j)_y(e_i)_y\}dy.$$

Here, the subscripts z and y designate differentiation with respect to these variables, and ε and μ are the permittivity and permeability of the medium.

We consider set (2) together with the initial conditions

$$f_1(z, t)\big|_{t=0} = \varphi(z), \quad f_1(z, t)_t\big|_{t=0} = -(\varepsilon\mu)^{-1/2}\varphi'(z),$$
$$f_s(z, t)\big|_{t=0} = 0, \quad f_s(z, t)_t\big|_{t=0} = 0, \qquad (3)$$
$$s = 2, 3, 4, \ldots,$$

where the function $\varphi(z)$ corresponding to the initial shape of the pulse is considered to be finite and concentrated inside the interval $\alpha < z < \beta$ in the regular section of the layer ($\alpha < \beta < 0$). Since only a certain finite region Λ of dimensionless variables z and t ($\Lambda = \{z_1 \le z \le z_2, 0 \le t \le T\}$) is usually of interest and $z_1 < \alpha$, $z_2 > 0$, $T \le \min\{|z_1 + \alpha|, |z_2 - \beta|\}$, we supplement Eqs. (3) by the auxiliary boundary conditions

$$\mathbf{f}(z_1, t) = \mathbf{f}(z_2, t) = \mathbf{0}, \quad 0 \le t \le T. \qquad (4)$$

The problem involving Eq. (2) with conditions (3) and (4) is closed and makes it possible to find $f(z, t)$ numerically on a discrete mesh in the rectangle Λ.

We also present the total energy density $W(t)$ of the pulse per unit layer width along the x-axis,

$$W(t) = \int_{z_1}^{z_2} dz \int_{-a_1(z)}^{a_2(z)} dy$$
$$\times\left\{\mu\Big(\sum e_s f_s\Big)^2 + \varepsilon^{-1}\left[\left(\int_0^t \Big(\sum e_s f_s d\eta\Big)_y\right)\right]^2\right.$$
$$\left. + \varepsilon^{-1}\left[(\varepsilon\mu)^{1/2}e_1\varphi(z) - \int_0^t \Big(\sum e_s f_s\Big)_z d\eta\right]^2\right\}, \qquad (5)$$

which must be independent of t. This property will be used to estimate the accuracy of calculations.

Figure 1 shows the line profile chosen as an example ($a_1(z) = 0.5$; $a_2(z) = [0.05 + 0.45\cos(\pi z)]$ for $0 < z < 2$ and $a_2(z) = 0.5$ for $z \le 0$ and $z \ge 2$) such that $\Delta_0 = 1$, and the gap width in the narrowest section (for $z = 1$) is equal to $\dfrac{\Delta_0}{10} = 0.1$. Figure 1 also shows the plots of $f_1(z, t)$ as a function of z for the fixed $t =$ (*1*) 0, (*2*) 1, (*3*) 2, (*4*) 3, and (*5*) 4. These plots describe the dynamics of change in the shape of the TEM component of the pulse. The calculations were carried out retaining six terms in sum (1) and with $\varepsilon = \mu = 1$. Derivatives for the mesh steps $hz = 0.01$ and $ht = 0.004$ were calculated with an increased accuracy by the differentiation formulas based on five and seven points for the first and second derivatives with respect to z, respectively, and on three points for derivatives with respect to t.

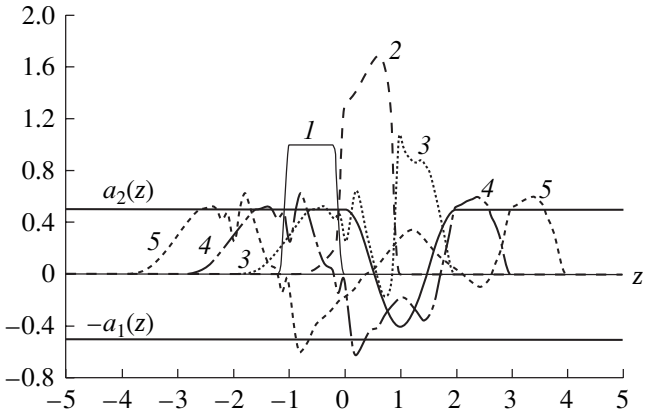

Fig. 1.

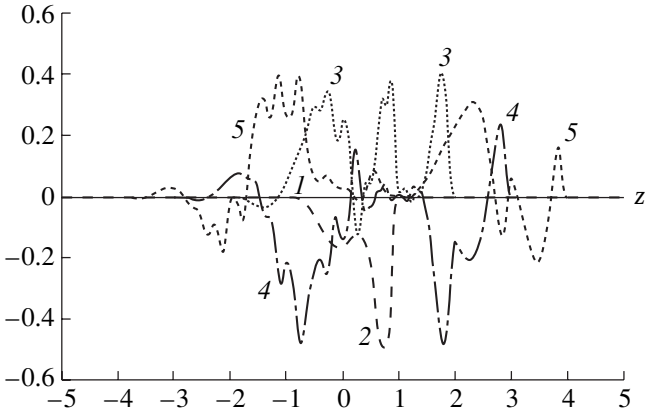

Fig. 2.

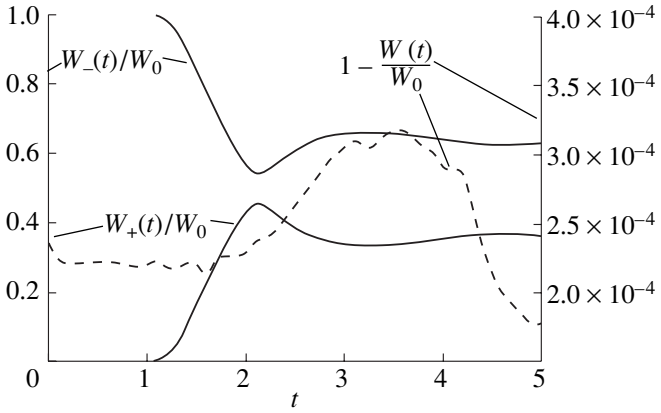

Fig. 3.

Table

$\frac{W_j}{W_0}$	$N = 9$	$N = 12$	$N = 15$
$\frac{W_1}{W_0}$	8.7598×10^{-1}	8.7522×10^{-1}	8.7488×10^{-1}
$\frac{W_2}{W_0}$	1.1081×10^{-1}	1.1135×10^{-1}	1.1178×10^{-1}
$\frac{W_3}{W_0}$	1.4333×10^{-2}	1.4090×10^{-2}	1.3960×10^{-2}
$\frac{W_4}{W_0}$	9.9306×10^{-3}	1.0120×10^{-2}	1.0108×10^{-2}
$\frac{W_5}{W_0}$	1.6001×10^{-3}	1.5997×10^{-3}	1.6345×10^{-3}
$\frac{W_6}{W_0}$	1.8852×10^{-3}	1.9335×10^{-3}	1.9527×10^{-3}
$\frac{W_7}{W_0}$	5.7760×10^{-4}	6.2584×10^{-4}	6.3244×10^{-4}
$\frac{W_8}{W_0}$	5.2230×10^{-4}	5.6044×10^{-4}	5.6511×10^{-4}
$\frac{W_9}{W_0}$	1.3797×10^{-4}	1.8290×10^{-4}	1.8832×10^{-4}
$1 - \frac{W}{W_0}$	2.9261×10^{-4}	2.9361×10^{-4}	2.9337×10^{-4}

Figure 2 shows the plots of $f_2(z, t)$, which corresponds to the E_{01} mode as a function of z for the same fixed values of t as in Fig. 1. Curves indicated by identical numbers in Figs. 2 and 1 correspond to identical values of t. The dynamics of formation of the E_{01} mode, which is absent at $t = 0$ $\{f_2(z, 0) = 0$, curve *1*$)$ due to the partial transformation of the TEM mode into the E_{01} mode in the irregular section of the line, are shown.

The accuracy of calculations is illustrated in Fig. 3 by the quantity $\left[1 - \frac{W(t)}{W_0}\right]$ as a function of t $\{W_0 = W(0)\}$. The same approximation, which is still far from the capability limit of current personal computers, provides a highly accurate determination of $W(t)$ with a relative error of ~0.03%. The table presents the relative energies $\frac{W_j}{W_0}$ calculated for the TEM ($j = 1$), E_{01} ($j = 2$), and E_{08} ($j = 9$) modes at $t = 4$ for $N = 9$, 12, and 15 with errors $\left(1 - \frac{W}{W_0}\right)$, which are equal to $\sim 3 \times 10^{-4}$ and depend only weakly on N. The table indicates that the choice of $N = 6$ in the example under consideration is justified.

As is seen, the accuracy of the method considerably exceeds the current experimental accuracy (~5%). Therefore, there are new possibilities for investigating UWB EMPs, including new approaches in developing standard devices for the calibration of UWB-EMP sensors.

Figure 3 also shows the relative values of that fraction of the energy density $\frac{W_+(t)}{W_0}$ per unit length which penetrates through the narrow section $z = 1$ and the reflected fraction $\frac{W_-(t)}{W_0}$ as functions of t. The functions $W_+(t)$ and $W_-(t)$ were calculated by Eq. (5) after replacing z_1 by 1 and z_2 by 1. In this case, $W_+(t) + W_-(t) = W(t)$. For $t = 5$, energy penetration is virtually completed at a penetration level of 36.7%.

REFERENCES

1. *Ultra-Wideband, Short-Pulse Electromagnetics 3*, Ed. by C. E. Baum, L. Carin, and A. P. Stone (Plenum, New York, 1997).
2. V. I. Koroza, Pis'ma Zh. Tekh. Fiz. **22** (21), 6 (1996) [Tech. Phys. Lett. **22** (11), 865 (1996)].

Translated by V. Bukhanov

Doklady Physics, Vol. 47, No. 7, 2002, pp. 507–509. Translated from Doklady Akademii Nauk, Vol. 385, No. 1, 2002, pp. 54–56.

TECHNICAL PHYSICS

Coupled Ferroelectric–Magnetoelastic Waves in Antiferroelectric Ferromagnets

I. R. Kyzyrgulov and M. Kh. Kharrasov

Presented by Academician V.V. Osiko March 1, 2002

Received January 30, 2002

1. Ferroelectric magnets are the crystals simultaneously combining properties of ferroelectrics or antiferroelectrics and ferromagnets or antiferromagnets. In other words, ferroelectric magnets are modifications of ferroelectrics, on the one hand, and magnets, on the other hand. They can fulfill many functions of ferroelectrics and ferrites and, therefore, can serve as a basis for the development of multifunctional elements of radio circuits.

Up to now, coupled ferroelectric–magnetoelastic waves were considered only for ferroelectric antiferromagnets and ferroelectric ferromagnets [1–3]. Studies of coupled waves for antiferroelectric ferromagnets and antiferroelectric antiferromagnets were not carried out.

We will consider an antiferroelectric ferromagnet consisting of three subsystems interacting with each other, namely, magnetic, elastic, and ferroelectric subsystems, and write out its energy in the form

$$H = H_M + H_U + H_F + H_{MU} + H_{MF} + H_{FU}. \qquad (1)$$

Here, H_M, H_U, and H_F are the energies of magnetic, elastic, and ferroelectric subsystems, respectively; the rest of the terms represent the energies of corresponding interactions. The energies of uniform and nonuniform exchange and of relativistic interactions are taken into account in the Hamiltonian of the magnetic subsystem in an external field. The elastic subsystem is considered in a harmonic approximation, and the reciprocal dielectric susceptibility and correlation properties are taken into account in the Hamiltonian of the ferroelectric subsystem. Magnetoelectric energy, naturally, is relativistic.

2. We write out Hamiltonian (1) in the approximation of secondary quantization. To this end, the magnetic momenta **M** are expressed in terms of the Holstein–Primakoff operators a^+, a; the vector of elastic displacements **u** is expressed in terms of operators of creation and annihilation of phonons b_{ks}^+, b_{ks} (see, e.g., [4]); and the deviation of the polarization vector from the equilibrium value **P** is expressed in terms of the creation and annihilation operators of segnetons $d_{k\delta\alpha}^+$, $d_{k\delta\alpha}$ [2].

Furthermore, for diagonalization of the Hamiltonian of the magnetic and ferroelectric subsystems, we use the Bogolyubov canonical transformation

$$a_k = u_k c_k + v_k^* c_{-k}^+, \quad a = V^{-1/2}\sum_k a_k e^{ikr},$$

$$d_{k\delta\alpha} = U_{k\delta\alpha\gamma} D_{k\delta\gamma} + V_{k\delta\alpha\gamma}^* D_{-k\delta\gamma}^+.$$

Then, Hamiltonian (1) can be written in the form

$$H = \sum_k \varepsilon_k^M c_k^+ c_k + \sum_{ks} \varepsilon_{ks}^U b_{ks}^+ b_{ks} + \sum_{k\delta\alpha} E_{k\delta\alpha} D_{k\delta\alpha}^+ D_{k\delta\alpha}$$

$$+ \left\{ \sum_{ks} \Psi_{ks}^{MU} c_k [b_{-ks} - b_{ks}^+] + \sum_{k\delta\alpha} \Psi_{k\delta\alpha}^{MF} c_k [D_{-k\delta\alpha} - D_{k\delta\alpha}^+] \right.$$

$$\left. + \sum_{k\delta\alpha s} \Psi_{k\delta\alpha s}^{FU} D_{k\delta\alpha} [b_{-ks} - b_{ks}^+] + \text{h.c.} \right\},$$

where ε_k^M, ε_{ks}^U ($s = 1, t_1, t_2$), $E_{k\delta\alpha}$ ($\delta = 1, 2$; $\alpha = 1, 2$) are the energies of corresponding branches of spin, elastic, and ferroelectric waves. The parameters of magnetoelastic and magnetoelectric interactions are defined by the expressions

$$\Psi_{ks}^{MU} = i\sqrt{\frac{\mu M_0}{2\rho\varepsilon_{ks}^U}}(b_{imn} + 2M_0 b_{ijmn} e_{3j}) Q_{ik} e_{km}^s k_n.$$

Here, the first and second term correspond to the piezomagnetic effect and magnetostriction, respectively; $\mathbf{e}_k^s$ is the unit polarization vector of photons; $i, j, m, n = x, y, z$,

$$Q_{ik} = e_{\perp i} u_k + e_{\perp i}^* v_k,$$

Bashkortostan State University, Ufa, ul. Frunze 32, 450074 Russia

1028-3358/02/4707-0507$22.00

$$e_{3i} = \frac{M_{0i}}{M_0}, \quad e_{\perp i} = \frac{1}{\sqrt{2}}(e_{1i} + ie_{2i}),$$

$$\mathbf{e}_1 \perp_s (\mathbf{M}_0, \mathbf{H}_0), \quad \mathbf{e}_2 = [\mathbf{e}_3, \mathbf{e}_1];$$

and

$$\Psi^{MF}_{k\delta\alpha} = -\sqrt{\frac{\lambda\mu M_0}{8\pi\varepsilon^f_{k\delta\alpha}}}(a_{im} + 2M_0 a_{ijm}e_{3j}) \times e^{\delta}_{ki}Q_{mk}(U_{k\delta\gamma\alpha} - V_{k\delta\gamma\alpha}), \quad (2)$$

where the first and second terms describe the linear magnetoelectric effect and magnetic anisotropy induced by vector **P**, respectively. The electroelastic coupling parameter has the simple form

$$\Psi^{FU}_{k\delta\alpha s} = i\sqrt{\frac{\lambda}{8\pi\rho\varepsilon^f_{k\delta\alpha}\varepsilon^U_{ks}}}(w_{ijm}e^{\delta}_{ki}e^{s}_{kj}k_m + i\nu_{ijmn}e^{\delta}_{ki}e^{s}_{km}k_jk_n)(U_{k\delta\gamma\alpha} - V_{k\delta\gamma\alpha}),$$

where w_{ijm} is the piezoelectric-constant tensor and ν_{ijmn} is the tensor related the polarization irregularities and strain.

The eigenfrequencies of magnetoelastic waves are found from the equations of motion for secondary quantized operators. Up to the terms quadratic in the coupling constants, the dispersion relation has the form

$$\prod_{s\delta\alpha}(\omega^2 - \varepsilon^{M^2}_k)(\omega^2 - \varepsilon^{U^2}_{ks})(\omega^2 - E^2_{k\delta\alpha})$$

$$-4\sum_s \left|\Psi^{MU}_{ks}\right|^2 \varepsilon^M_k\varepsilon^U_{ks}\prod_{s'\neq s}(\omega^2 - E^2_{k\delta\alpha})(\omega^2 - \varepsilon^{M^2}_k)(\omega^2 - \varepsilon^{U^2}_{ks'})$$

$$-4\sum_{\delta\alpha}\left|\Psi^{MF}_{k\delta\alpha}\right|^2 \varepsilon^M_k E_{k\delta\alpha}\prod_{(\delta',\alpha')\neq(\delta,\alpha)}(\omega^2 - \varepsilon^{U^2}_{ks})(\omega^2 - E^2_{k\delta'\alpha'})$$

$$-4\sum_{\delta\alpha s}\left|\Psi^{FU}_{k\delta\alpha s}\right|^2 \varepsilon^U_{ks}E_{k\delta\alpha}$$

$$\times \prod_{s'\neq s,\,(\delta',\alpha')\neq(\delta,\alpha)}(\omega^2 - \varepsilon^{U^2}_{ks'})(\omega^2 - E^2_{k\delta'\alpha'}) = 0.$$

3. Interaction between spin waves and ferroelectric waves (2) depends on the direction of the vector **k** with respect to the magnetizations and polarizations of sublattices, external magnetic and electric fields, and magnitude of the field itself for various magnetic and ferroelectric waves. We consider particular cases (coupling constants that are equal to zero in our approximation are omitted).

(a) The case $k \parallel Z$:

$$\Psi^{MF}_{k11} = \gamma_1[a_{xy}(u_k + v_k) + ia_{xz}\sin\theta(u_k - v_k) + 2M_0\{a_{xxy}\sin\theta(u_k + v_k) + ia_{xxz}\sin^2\theta(u_k - v_k)\}][U_{k111} - V_{k111}],$$

$$\Psi^{MF}_{k21} = \gamma_2[i(a_{yz}\sin\theta - a_{yx}\cos\theta)(u_k - v_k) + 2M_0\{a_{yxy}\sin\theta(u_k + v_k) + ia_{yxz}\sin^2\theta(u_k - v_k)\}][U_{k211} - V_{k211}];$$

(b) The case $k \parallel Y$;

$$\Psi^{MF}_{k11} = -\gamma_1[a_{zy}(u_k + v_k) - ia_{zx}\sin\theta(u_k - v_k) + 2M_0\{a_{zxy}\sin\theta(u_k + v_k) + ia_{zxz}\sin^2\theta(u_k - v_k)\}][U_{k111} - V_{k111}],$$

$$\Psi^{MF}_{k21} = \gamma_2[a_{xy}(u_k + v_k) + ia_{xz}\sin\theta(u_k - v_k) + 2M_0\{a_{xxy}\sin\theta(u_k + v_k) + ia_{xxz}\sin^2\theta(u_k - v_k)\}][U_{k211} - V_{k211}];$$

(c) The case $k \parallel X$;

$$\Psi^{MF}_{k11} = \gamma_1[i(a_{yz}\sin\theta - a_{yx}\cos\theta)(u_k - v_k) + 2M_0\{a_{yxy}\sin\theta(u_k + v_k) + ia_{yxz}\sin^2\theta(u_k - v_k)\}][U_{k111} - V_{k111}],$$

$$\Psi^{MF}_{k21} = -\gamma_2[a_{zy}(u_k + v_k) - ia_{zx}\cos\theta(u_k - v_k) + 2M_0\{a_{zxy}\sin\theta(u_k + v_k) + ia_{zxz}\sin^2\theta(u_k - v_k)\}][U_{k211} - V_{k211}],$$

where

$$\gamma_\delta \equiv \sqrt{\frac{\lambda\mu M_0}{4\pi\varepsilon^f_{k\delta 1}}}, \quad \cos\theta = \frac{H_0}{H_\beta};$$

$$\sin\theta = \sqrt{1 - \frac{H_0^2}{H_\beta^2}}, \quad H_\beta = M_0(\beta_{zz} - \beta_{xx}).$$

We can see that with an increasing magnetic field, switching of the coupling between the spin and ferroelectric modes occurs.

The general pattern of coupled ferroelectric–magnetoelastic waves in the absence of the external field for the case $k \parallel X$ has the form presented in the figure.

It is clearly seen in the figure that a coupled ferroelectric–magnetoelastic wave is consistent with the proper oscillations of various subsystems in different regions. Therefore, moving along it, we can pass from

spin waves to acoustic waves, then to ferroelectric waves, etc.

4. As is well known, in antiferromagnets, a reduction of the gap in the spin-wave spectrum occurs within the region of a phase transition. Along these lines, an increase in the coupling of magnetic oscillations with oscillations of the elastic medium was observed in [5]. Within the region of the magnetoelastic resonance, in which $\varepsilon_k^M \approx \varepsilon_{ks}^U$ (the region of intersection of the spin branch and acoustic branch), we can write $\xi^{MU} = \dfrac{\Psi_{ks}^{MU}}{\varepsilon_k^M}$ for the interaction parameter. It is seen from this expression that reduction of the gap in the spin-wave spectrum results in an increase in the coupling coefficient of the subsystems. The effect of a magnetoelastic gap or hardened lattice can serve as an example [5]. Under usual conditions, as a rule, $\xi^{MU} \ll 1$. However, within the region of the phase transition, when the magnon gap in the spin-wave spectrum loses its positive definiteness and only the magnetoelastic gap remains, the coupling coefficient approaches unity, $\xi^{MU} \approx 1$.

A similar phenomenon can be observed in antiferroelectric ferromagnets. The calculations show that in the region of the antiferroelectric–ferroelectric phase transition, a sufficient reduction of the gap in the spectrum of the first and second ferroelectric branches is observed. As was mentioned above, the parameter of the magnetoelectric coupling within the region of the magnetoelectric resonance has the form $\xi^{MF} = \dfrac{\Psi_{k\delta 1}^{MF}}{E_{k\delta 1}}$. Due to the fact that, away from the phase-transition region $\xi^{MF} \approx 10^{-4}$, the gaps in the spectrum of spin and ferroelectric branches are $\varepsilon_0^M \approx 10^{10}$ s^{-1} and $E_{0\delta 1} \approx 10^{12}$ s^{-1}, respectively, in the phase-transition region (under condition $\varepsilon_0^M < E_{0\delta 1}$), the parameter of the magnetoelectric coupling becomes larger by three orders of magnitude and attains $\xi^{MF} \approx 10^{-1}$. This high value of the coupling coefficient is of a considerable importance from the standpoint of signal transformation, since it makes it possible to transform a magnetic signal into an electric one and vice versa with a minimal loss.

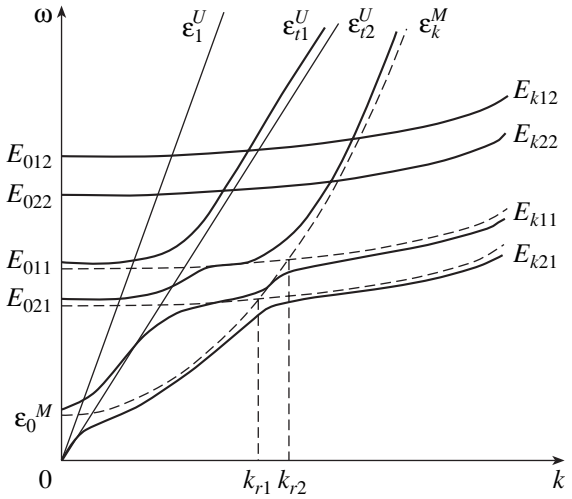

Coupled ferroelectric–magnetoelastic waves for $k \parallel X$.

It should be kept in mind that this effect can exist only in ferroelectric magnets with a ferroelectric Néel point lower than the magnetic Curie point.

REFERENCES

1. M. Kh. Kharrasov and A. U. Abdullin, Dokl. Akad. Nauk **336** (3), 335 (1994) [Phys. Dokl. **39**, 346 (1994)].
2. M. A. Savchenko and M. A. Khabakhpashev, Fiz. Tverd. Tela (Leningrad) **18** (9), 2699 (1976) [Sov. Phys. Solid State **18**, 1573 (1976)].
3. N. Ya. Plyushko and I. E. Chupis, Ukr. Fiz. Zh. **19** (5), 824 (1974).
4. N. N. Bogolyubov, Jr. and B. I. Sadovnikov, *Certain Questions of Statistical Mechanics* (Vysshaya Shkola, Moscow, 1975).
5. E. A. Turov and V. G. Shavrov, Usp. Fiz. Nauk **140**, 429 (1983) [Sov. Phys. Usp. **26**, 593 (1983)].

Translated by T. Galkina

Doklady Physics, Vol. 47, No. 7, 2002, pp. 510–514. Translated from Doklady Akademii Nauk, Vol. 385, No. 2, 2002, pp. 181–185.

TECHNICAL PHYSICS

Dependence of Shape Memory Effect and Superelasticity on the Number of Variants of Dispersed Particles in Titanium–Nickel Single Crystals

Yu. I. Chumlyakov*, E. Yu. Panchenko*, I. V. Kireeva*,
Corresponding Member of the RAS S. P. Efimenko, V. B. Aksenov*, and H. Sehitoglu*****

Received March 4, 2002

It is known that aging under load in Ti–51 at. % Ni polycrystals results in the change of microstructure in contrast to aging in a free state. In the grains oriented in the ⟨111⟩ direction, under tensile load, one crystallographic variant of dispersed Ti_3Ni_4 particles grows under applied tensile stress in the elastic range; without load, four variants of particles grow [1]. Consequently, using Ti–51 at. % Ni single crystals for experimental investigation of aging under load allows us to control the microstructure of crystals, to exclude the effect of boundary grains, and to study the dependence of the shape memory effect and superelasticity on the number of crystallographic variants of the particles. Earlier, we showed that aging without load in Ti–51 at. % Ni single crystals is accompanied by a precipitation of four variants of Ti–51 at. % Ni dispersed particles Ti_3Ni_4, which do not undergo martensitic transformations [2]. The aging of Ti–51 at. % Ni single crystals under tensile load in the ⟨111⟩ and ⟨122⟩ directions was supposed to result in the growth of one variant of particles, as was predicted theoretically [1]. In this study, the effect of the number of variants of dispersed particles on the shape memory effect and superelasticity in the B2–R–B19' martensitic transformation was determined in Ti–51 at. % Ni single crystals.

Single crystals of Ti–51 at. % Ni were grown by the Bridgman method. The preparation technique for samples was presented in [2]. Aging under a load of 150 MPa was carried out in vacuum. The sizes, volume fraction of dispersed particles, and interparticle distances determined by electron-microscopy observations for samples aged without load and under load are presented in the table. It is seen that the particle sizes vary from 40 to 430 nm when the aging temperature takes on values from 673 to 823 K. The volume fraction of particles $f = 9\%$ and the nickel concentration $C_{Ni} = 50.5$ at. % after aging are approximately equal in all the aging regimes and are independent of the number of variants. The average distance between particles L in the case of one variant is less than the value for the case of four variants.

Figure 1 shows the heat-release curves obtained by the method of differential scanning calorimetry (DSC) and temperature dependence of the electrical resistance $\rho(T)$ for crystals aged without load and under load. Figure 2 shows the temperature dependence of the yield load, and superelasticity loops for the same crystals are shown in Figs. 3 and 4. The table also contains the values of the shape memory effect and superelasticity for crystals. The analysis of data presented in the table and in Figs. 1–4 shows that the value of shape memory effect and superelasticity, martensitic-transformation temperatures M_s, M_f, A_s, and A_f, and the strength properties depend on the number of variants and on the sizes of dispersed particles. First, the comparison of the DSC and $\rho(T)$ curves (Fig. 1) for crystals A_I and B_I aged under load with one variant with the corresponding curves for A_{IV} and B_{IV} aged without load with four variants shows that the points M_{s1} and M_{s2} for crystals with one variant of particles are 10 K higher than the corresponding temperatures for crystals with four variants. Earlier, it was shown [2] that M_{s1} is associated with the R–B19' martensitic transformation in the field of local loads of Ti_3Ni_4 particles; M_{s2}, with the transformations in regions free of particles. Second, it is seen in Fig. 2 that the $\sigma_{0.1}(T)$ minimum, which corresponds to the temperature of the martensitic-transformation onset in the material bulk, lies at a higher temperature for A_I crystals than for A_{IV} crystals, and $\sigma_{0.1}(M_s)$ for crystals A_I is about half the value for A_{IV}. Qualitatively similar dependences are obtained for crystals B_I and B_{IV}. Third, the temperature range of the stress-induced martensitic transformation ΔT and the temperature range of

**Siberian Physicotechnical Institute, Tomsk State University, Tomsk, Novosobornaya pl. 1, 634050 Russia*
***Baikov Institute of Metallurgy and Materials Science, Russian Academy of Sciences, Leninskiĭ pr. 49, Moscow, 107311 Russia*
****University of Illinois, 1206 West Green St., Urbana, Illinois 61801, USA*

1028-3358/02/4707-0510$22.00

superelasticity ΔT_{SE} for crystals C are sufficiently wider than the respective ranges for crystals A and B (see Figs. 2–4 and table). For the same size of particles in C_I crystals, ΔT_{SE} = 135 K is 15 K higher than the value for C_{IV} crystals (Figs. 3 and 4). Fourth, the values of the shape memory effect and superelasticity for A_I, B_I, and C_I crystals are less than the respective values for A_{IV}, B_{IV}, and C_{IV} crystals (see table). The dependence of the shape memory effect and superelasticity on the microstructure parameters is physically associated with the features of the martensitic-transformation development in structurally inhomogeneous crystals containing Ti_3Ni_4 particles, which do not undergo the B2–R–B19' transformation. In titanium–nickel crystals without dispersed particles, the main twinning type for B19' martensite is the II-type twinning ⟨011⟩, whereas the twinning type changes in the case of precipitating Ti_3Ni_4 particles, and B19'-martensite crystals contain a high density of compound twins ⟨001⟩ (100) [4, 5]. The density of compound twins increases with decreasing distance between particles [5] and, consequently, depends on the number of variants of particles, since the distance between particles for crystals A_I, B_I, and C_I with one variant of particles is less than the value for A_{IV}, B_{IV}, and C_{IV} with four variants. Therefore, the density of compound twins in A_I, B_I, and C_I crystals is higher than the density in A_{IV}, B_{IV}, and C_{IV} crystals. Since dispersed particles suppress the detwinning of martensite crystals [5, 6], first, for the same crystal orientation, e.g., ⟨111⟩, shape memory effect in single-phase crystals is significantly larger than the effect in crystals with particles (see table). Second, in the heterophase ⟨111⟩ crystals, shape memory effect depends on the particle size, interparticle distance, and the number of particle variants [2]. The rise in the volume fraction of dispersed particles in ⟨111⟩ crystals of Ti–51.3 at. % Ni, Ti–51.5 at. % Ni after aging at 823 K for 1.5 h, significantly reduces shape memory effect from 4.8% in A_{IV} Ti–51 at. % Ni crystals to 3.5%. This decrease is caused by decreasing of interparticle distance with the increase in the volume fraction of dispersed particles. The same effect is responsible for decreasing shape memory effect and superelasticity when transitioning from four variants to one variant of particles (see table).

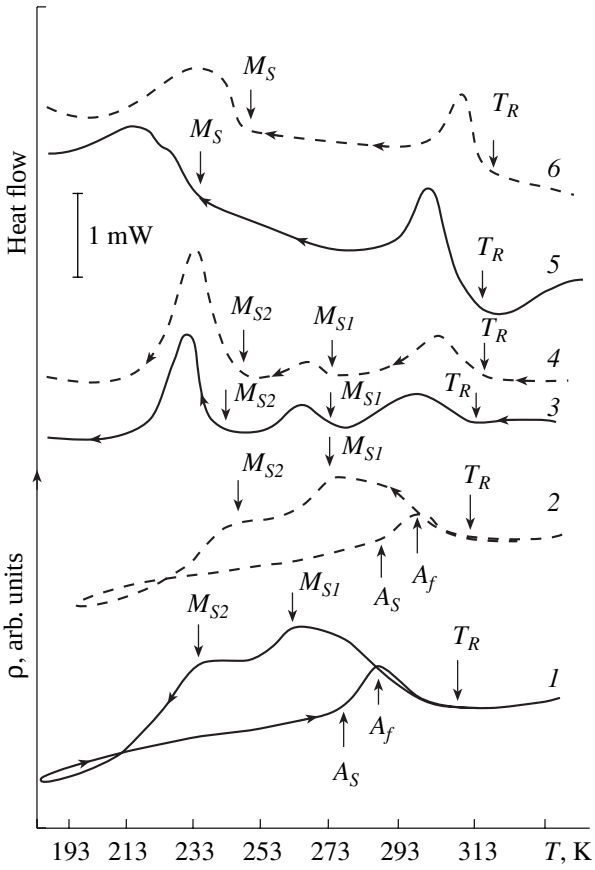

Fig. 1. DSC curves and temperature dependence of electrical resistance ρ(*T*) for Ti–51 at. % Ni single crystals after various thermal treatments: (*1*) ρ(*T*) and (*3*) DSC at 823 K for 1.5 h without load (A_{IV}), (*2*) ρ(*T*) and (*4*) DSC at 823 K for 1.5 h under a load of 150 MPa (A_I), (*5*) DSC at 773 K for 1 h without load (B_{IV}), and (*6*) DSC at 773 K for 1 h under a load of 150 MPa (B_I).

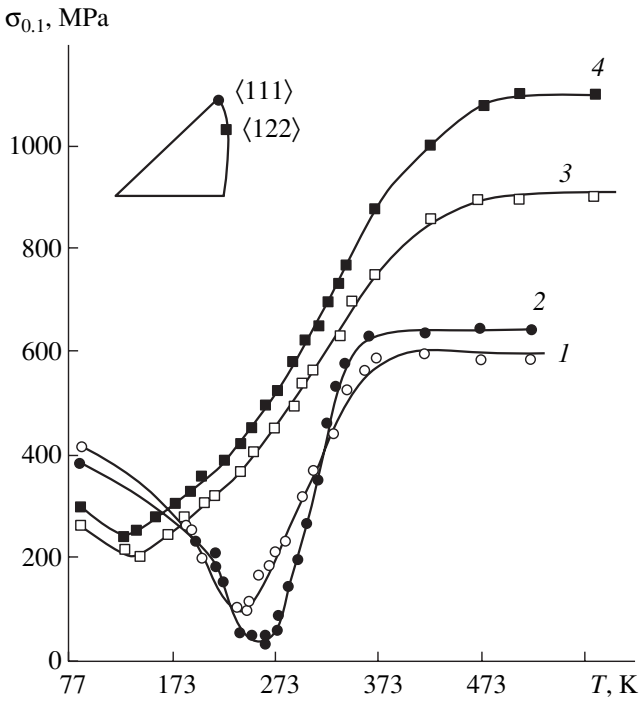

Fig. 2. Temperature dependence of yield load for Ti–51 at. % Ni single crystals under tension after various thermal treatments: (*1*) and (*2*), at 823 K for 1.5 h without load (A_{IV}) and under a load of 150 MPa (A_I), respectively; (*3*) and (*4*), at 673 K for 1 h without load (C_{IV}) and under a load of 150 MPa (C_I), respectively.

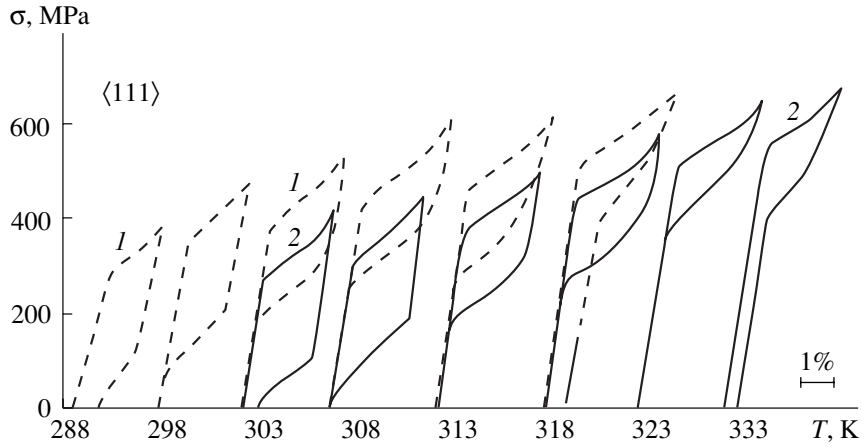

Fig. 3. Temperature dependence of the superelasticity loop for Ti–51 at. % Ni single crystals aged at 823 K for 1.5 h: (*1*) without load (A_{IV}) and (*2*) under a tension load of 150 MPa (A_I).

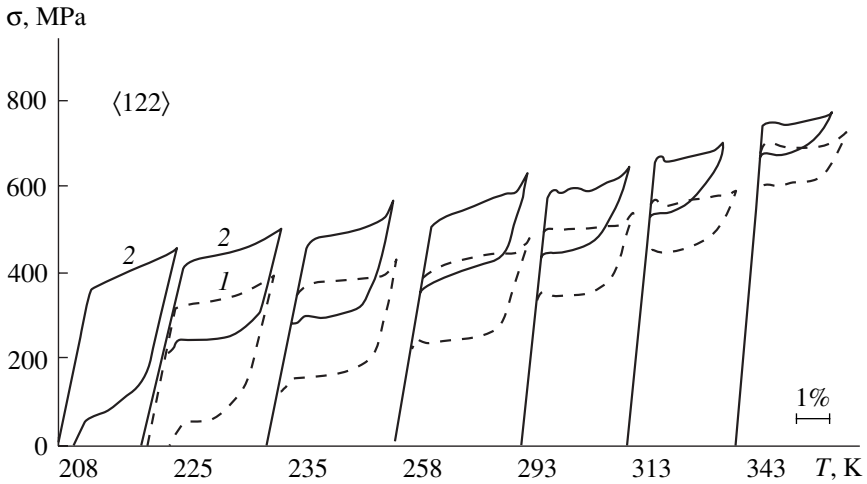

Fig. 4. The same as in Fig. 3, but at 673 K for 1 h: (*1*) C_{IV} crystals and (*2*) C_I crystals.

Thus, a self-accommodated system of type-II twinned martensite crystals is formed in Ti–51 at. % Ni single crystals without particles at $T < M_s$. This system gains strain ε_0 under load and transforms into a B19' martensite single crystal without structural defects associated with the motion of twins and intervariant interfaces. Heating of the sample to $T > A_f$ results in the transformation of a B19' single crystal into a B2 single crystal; strain ε_0 restores its original shape [4]. In crystals with one and four variants of particles at $T < M_s$, B19' martensite has a high density of compound twins, which cannot completely detwin the martensite crystal under deformation because dispersed particles offer resistance to the motion of twins. Therefore, the shape memory effect ε_0 in heterophase alloys is less than the value for single-phase crystals and is caused not only by the lattice deformation in the B2–R–B19' martensitic transformation, as in single-phase crystals, but also by the lattice deformation in the B2–B19' martensitic transformation with the subsequent combined twinning of B19' crystals [2, 3, 6].

Dependence of M_s and $\sigma_{0.1}(M_s)$ in A and B crystals on the number of particle variants is associated with the features of the heterogeneous nucleation of B19' martensite near dispersed particles and with the appearance of long-range load fields in crystals with one variant of particles. Precipitation of four variants of particles each producing internal load fields due to a difference in the lattice parameters of the particle and matrix does not result in the appearance of long-range uniform load fields in the crystal due to their mutual compensation. On the contrary, when one variant of dispersed particles is formed, uniform long-range load fields are created in the crystal [1, 4] due to superposed load fields from all particles and result in the 10-K increase in the temperatures M_{s1} and M_{s2} (Fig. 1), as well as in $\sigma_{0.1}(M_s)$

(Fig. 2). Using the local form of the Clapeyron–Clausius relation [3] gives us

$$M_s = T_0 + \frac{\Delta E^d}{\Delta S^{\text{a–m}}}, \quad (1)$$

where $T_0 = \frac{\Delta H^{\text{a–m}}}{\Delta S^{\text{a–m}}}$ is the phase equilibrium temperature determined by the nickel concentration in crystals after aging; $\Delta S^{\text{a–m}}$ and $\Delta H^{\text{a–m}}$ are the variations of entropy and enthalpy in the B2–B19' transformation, respectively; $\Delta E^d = -\sigma_{ij}\varepsilon_{ij}$ is the elastic energy of defects in the crystal; σ_{ij} is the internal load field around defects; and ε_{ij} is the shape deformation (see table) associated with the B2–B19' martensitic transformation (MT) in heterophase crystals. It follows from Eq. (1) that, first, splitting into two R–B19'-MT peaks in A crystals aged without load is caused by the appearance of internal loads σ_{ij} = 140 MPa near particles. Second, the 10-K increase in the martensitic transformation temperatures in A_I and B_I crystals with one variant of particles with respect to the values for A_{IV} and B_{IV} crystals corresponds to the appearance of long-range load fields σ_{ij} = 70 MPa.

Since shape memory effect in A_I and B_I crystals is less than the effect for A_{IV} and B_{IV} crystals (see table), the Clapeyron–Clausius relation [4]

$$\frac{d\sigma_{0.1}}{dT} = -\frac{\Delta H^{\text{a–m}}}{\varepsilon_0 T_0}$$

indicates that $\alpha = \frac{d\sigma_{0.1}}{dT}$ for one variant of particles must be larger than the value for four variants. Such a dependence of α on the number of variants is, in fact, observed experimentally (Fig. 2, curves *1* and *2*).

In C crystals containing one and four variants of Ti_3Ni_4 particles with sizes of 40 nm, strength properties of B2 phase are significantly higher than in A and B crystals (Fig. 2). As a result, the range of stress-induced martensitic transformation and the range of superelasticity is almost 5 times as large as the respective ranges for A and B crystals (see curves *3* and *4* in Fig. 2). Loads $\sigma_{0.1}(M_s)$ in C crystals are considerably higher than the values in A and B crystals, and the temperatures of martensitic transformation are lower. This behavior testifies to the stabilization of the B2 phase at the expense of fine particles (Fig. 2). Finally, in C_I crystals, M_s determined by the temperature of the minimum in $\sigma_{0.1}(T)$ is lower than the value in C_{IV} crystals, whereas in A and B crystals, the inverse dependence is observed (Fig. 2). This behavior indicates that the mechanisms of nucleation of B19' martensite crystals under cooling and load in A and B crystals can significantly differ from those in C crystals. Indeed, in A and B crystals, martensite crystals nucleate predominantly in large particles, as indicated by the appearance of two peaks associated with the R–B19' martensitic transformation. The critical nucleus size in A and B crystals with one and four variants of particles is less than the interparticle distance. In contrast, the critical nucleus size in C crystals exceeds the interparticle distance and, therefore, the elastic energy of martensite crystals increases due to the inclusion of Ti_3Ni_4 dispersed particles, which do not undergo the martensitic transformation.

Thus, for the first time, it has been shown that the magnitude of shape memory effect and superelasticity, the temperature range of superelasticity, and the temperatures of martensitic transformation in aging

Microstructure parameters and functional properties of Ti–51 at. % Ni single crystals after aging under load and without load

Thermal treatment		Size of particles, nm	Distance between particles, nm	Temperature range of superelasticity, K	Shape memory, %	Superelasticity
Aging, 823 K, 1.5 h	A_{IV} without load	430	360	30	5.45	4.8
	A_I under load	430	250	30	3.8	3.2
Aging, 773 K, 1 h	B_{IV} without load	100	140	40	5.5	4.5
	B_I under load	100	90	30	4.0	3.5
Aging, 673 K, 1.5 h	C_{IV} without load	40	40–50	120	5.5	4.2
	C_I under load	40	–	135	5.0	4.0

Ti–51 at. % Ni single crystals depend on the number of variants of Ti_3Ni_4 dispersed particles.

ACKNOWLEDGMENTS

This work was supported by the Russian Foundation for Basic Research, project nos. 99-03-32579, 01-03-06152, and 01-03-06151; and by the Ministry of Education of the Russian Federation, project no. E00-3.04.29.

REFERENCES

1. L. Q. Chen and D. Y. Li, Acta Mater. **45** (2), 471 (1997).
2. Yu. I. Chumlyakov, S. P. Efimenko, I. V. Kireeva, *et al.*, Dokl. Akad. Nauk **381** (5), 610 (2001) [Dokl. Phys. **46** (12), 849 (2001)].
3. L. Bataillard, J.-E. Bidaux, and R. Gotthardt, Philos. Mag. A **78** (2), 327 (1998).
4. K. Otsuka and C. M. Wayman, *Shape Memory Effect Materials* (Cambridge Univ. Press, Cambridge, 1998).
5. C. M. Wayman, M. Nichida, and A. Chiba, Metallography **21,** 275 (1988).
6. K. Gall, H. Sehitoglu, I. Karaman, *et al.*, Acta Mater. **48,** 3311 (2000).

Translated by T. Galkina

Doklady Physics, Vol. 47, No. 7, 2002, pp. 515–517. Translated from Doklady Akademii Nauk, Vol. 385, No. 3, 2002, pp. 328–331.

TECHNICAL PHYSICS

Deformation Mechanisms and Strain Hardening of Hadfield-Steel Single Crystals Alloyed with Aluminum

E. G. Zakharova[1], I. V. Kireeva[1], Yu. I. Chumlyakov[1], Corresponding Member of RAS S. P. Efimenko[2], H. Sehitoglu[3], and I. Karaman[4]

Received March 4, 2002

Austenitic stainless steels with nitrogen content $C_N \geq 0.5$–0.9 wt % and Hadfield steel Fe–13Mn–1.3C (wt %) are extensively used in industry due to their unique mechanical properties—large strain-hardening coefficient, high plasticity, and increased wear resistance [1–6]. The necessary set of properties in these steels is achieved by the combination of a high concentration of interstitial atoms and low stacking-fault energy $\gamma_{SF} = 0.020$–0.030 J/m^2. The main mechanisms of the Hadfield steel hardening include twinning, dynamic strain aging, and development of γ–ε martensitic transformations [1–15]. It is impossible to experimentally separate these contributions for Hadfield steel polycrystals, since slip and twinning occur simultaneously. Experiments on Hadfield steel single crystals enable us to overcome these difficulties and to separate the contributions of twinning and slip to hardening by a special choice of crystal orientations and temperature [1, 6–10, 13–15].

In order to reveal the nature of strain hardening in austenitic steels with a high content of carbon, we studied the orientational dependence of the deformation mechanisms of Fe–13Mn–1.3C (I) and Fe–13Mn–2.7Al–1.3C (II) (wt %) steels. The choice of alloys for studies was based on the following reasoning. First, mechanical twins are not observed in steel-II polycrystals, and deformation occurs through slip [3]. In contrast, Hadfield steel-I polycrystals are characterized by high densities of twins, stacking faults, and perfect dislocations split into partial Shockley dislocations [1, 2]. Consequently, one can suppose that aluminum alloying increases γ_{SF}, and that mechanical twinning is therefore suppressed. However, data on direct measurements of γ_{SF} by electron microscopy on steel II are not available.

Second, aluminum alloying results in a positive rate sensitivity of the flow stress, whereas the sensitivity of the flow stress in Hadfield steel is negative [3, 4]. For this reason, one can suppose that aluminum atoms change the diffusion mobility of carbon, and dynamical strain hardening in steel II at room temperature should not be expected. Such a difference in the diffusion mobility of carbon can result in the change of the dislocation structure type for slip strain [1, 3, 5]. Thus, new features of plastic deformation can be expected in steel-II single crystals compared to steel-I crystals, because the increase in the stacking fault energy of the matrix γ_{SF} and the decrease in the diffusion mobility of carbon atoms upon aluminum alloying can change the ratio between the mechanical twinning and slip. For this reason, the dislocation structure type—planar or cellular—for slip and, consequently, the regularities of strain hardening can be determined.

Crystals of steels I and II were grown by the Bridgman technique in an inert gas. The technique of sample preparation for studies was presented in [10, 13–15].

Figures 1 and 2 show the stress–strain curves for single crystals of steels I and II together with the variation of the orientation (precession) of the tension axis upon deformation. The dislocation structure of [001] and $[\bar{1}11]$ steel-II crystals deformed at room temperature up to ε = 6–10% is shown in Figs. 3 and 4.

Comparison of the mechanical properties of crystals I and II shows that the critical shear stresses τ_{cr} at $T = 300$ K are close to each other and, consequently, addition of aluminum does not result in additional solid-solution hardening. Studies of the rate sensitivity of stress $\beta = \dfrac{\Delta\sigma}{\Delta \ln \dot{\varepsilon}}$ in steel-II single crystals at room temperature indicate that β is positive for all orientations studied. In steel-I crystals deformed through slip, i.e., in orientations [012], $[\bar{1}23]$, and [001], β is negative, whereas in crystals with twinning, i.e., in $[\bar{1}11]$ and [011] orientations, β is positive [7, 10]. These results for the rate sensitivity of the flow stress during

[1] *Siberian Physicotechnical Institute, Tomsk State University, Tomsk, Novosobornaya pl. 1, 634050 Russia*

[2] *Baĭkov Institute of Metallurgy and Materials Science, Russian Academy of Sciences, Leninskiĭ pr. 49, Moscow, 107311 Russia*

[3] *University of Illinois at Urbana-Champaign, 1206 West Green Street, Urbana, IL 61801, USA*

[4] *Texas A&M University, College Station, TX 77843-3123, USA*

1028-3358/02/4707-0515$22.00

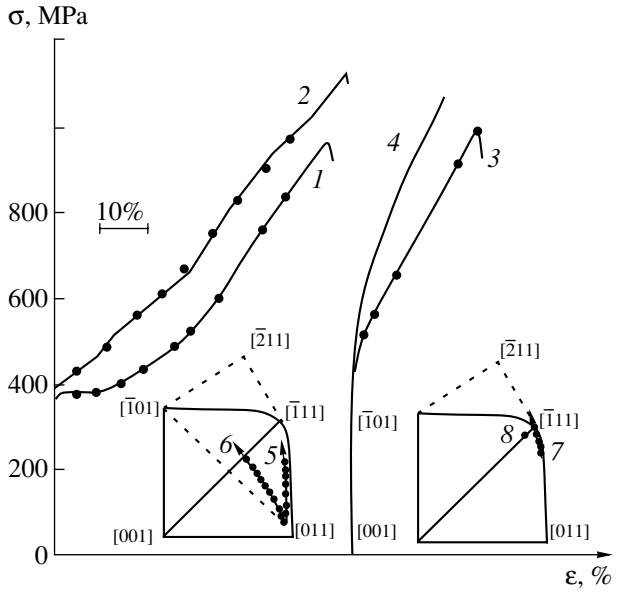

Fig. 1. Stress–strain curves and precession of the crystal axis for the tensile deformation of single crystals of Fe–13Mn–1.3C (I), Fe–13Mn–2.7Al–1.3C (II) (wt %) steels at room temperature: (*1*, *5*) [011] orientation of steel I, (*2*, *6*) [011] orientation of steel II, (*3*, *7*) [$\bar{1}$11] orientation of steel I, and (*4*, *8*) [$\bar{1}$11] orientation of steel II.

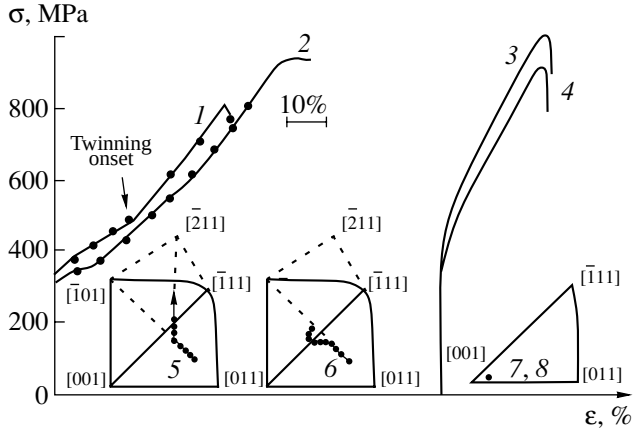

Fig. 2. The same as in Fig. 1, but for (*1*, *5*) [$\bar{1}$23] orientation of steel I, (*2*, *6*) [$\bar{1}$23] orientation of steel II, (*3*, *7*) [001] orientation of steel I, and (*4*, *8*) [001] orientation of steel II.

slip deformation in single crystals of steels I and II agree with the data obtained earlier for polycrystals of these alloys [3, 4]. The stacking fault energy estimate obtained via the technique of determining the width of triple dislocation nodes showed that the addition of aluminum increases the stacking fault energy from 0.020 ± 0.003 J/m^2 in crystals I to 0.050 ± 0.005 J/m^2 in crystals II. An increase in γ_{SF} and change of β from a negative value for steel I to a positive value for steel II result in the change of the deformation mechanism from twinning in steel I to slip in steel II.

Deformation in [011] crystals of steel I and in steel II occurs as twinning and slip, respectively. With the development of deformation in steel I through twinning in the primary system [$\bar{2}$11](111), low values of the strain-hardening coefficient $\theta = \frac{d\sigma}{d\varepsilon}$ for $\varepsilon \le 10\%$ are connected by the Luders band. The further increase in θ is caused by twinning development in both systems with predominant twinning shear in the primary system of twinning (Fig. 1, curves *1* and *5*). In crystals II, deformation occurs as slip (Fig. 1, curves *2* and *6*), the large values of θ are observed from the very onset of plastic strain, and the plastic flow develops at the single linear stage with $\theta = 1000$ MPa $= G/80$ ($G = 80\,000$ MPa is the shear modulus of the Hadfield steel [6]). The dislocation structure in steel II turns out to be planar: plane aggregates of dislocations and multipoles are observed (Fig. 3). Slip lines are identified metallographically. In contrast, for the slip in steel I in crystals [$\bar{1}$23], [012], slip lines are not observed, and plane aggregates of dislocations are absent in the dislocation structure [7].

Thus, aluminum alloying suppresses deformation through twinning in crystals [011] of steel II and changes the type of the dislocation structure from the uniform distribution in steel I to the planar dislocation structure in steel II. For slip deformation, θ/G is equal to θ_{II}/G for slip in other fcc crystals. Consequently, the planar dislocation structure in austenitic steels with a high concentration of carbon atoms provides virtually the same rate of strain hardening θ as multiple twinning.

For deformation through twinning in several systems in [$\bar{1}$11] crystals of steel I, θ is less than the value in steel II (Fig. 1, curves *3* and *4*), where planar slip occurs up to $\varepsilon < 10\%$, after which microtwins are observed. The development of mechanical twinning in several systems is responsible for the high θ values and the linear character of $\sigma(\varepsilon)$ curves in steel I for the predominant development of a single primary system [$\bar{2}$11](111) (Fig. 1, curve *7*) [1, 3, 11–15].

In crystals II, deformation with high θ is caused by the development of multiple planar slip and microtwinning (Fig. 4). The precession of the crystal axis is absent, and microtwinning and slip develop in several systems.

In [$\bar{1}$23] crystals, deformation up to $\varepsilon \le 10\%$ occurs as slip in steels I and II (Fig. 2, curves *1*, *2*, *5*, and *6*). However, the stages of stress–strain curves, the type of the dislocation structure, the value of θ, and the rate sensitivity of the flow stress β are different. In steel I, β has negative sign, which is attributed to the development of the dynamical strain aging at $T = 300$ K [4, 5]. High values of $\theta = G/80$ are caused by the intense accu-

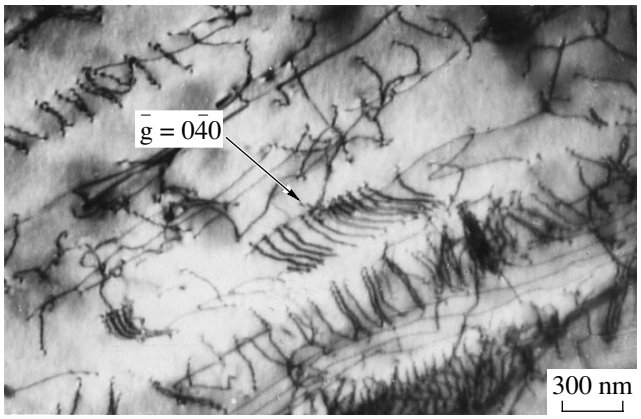

Fig. 3. Electron micrograph of the slip pattern under tension of [001] single crystals of Fe–13Mn–2.7Al–1.3C (wt %) steel for $\varepsilon = 6\%$ and $T = 300$ K.

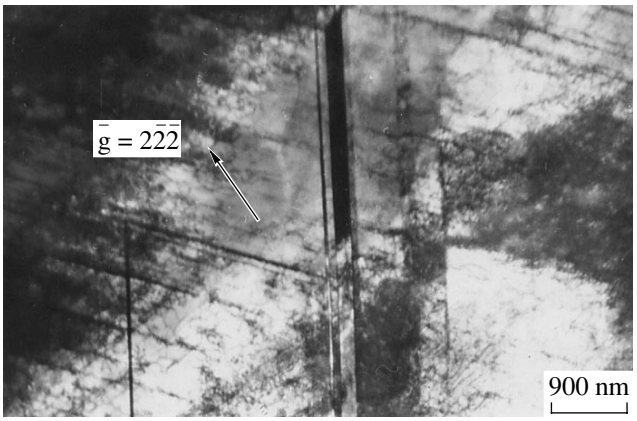

Fig. 4. Electron micrograph of the slip and twinning pattern under tension of $[\bar{1}11]$ single crystals of Fe–13Mn–2.7Al–1.3C (wt %) steel for $\varepsilon = 10\%$ and $T = 300$ K.

mulation of dislocations in crystals because of the high mobility of carbon atoms upon deformation. In steel II, β is positive, the processes of dynamical strain aging are suppressed at $T = 300$ K, and high values of $\theta = G/80$ result from the development of the planar dislocation structure and from interaction between plane aggregates and multipoles.

Finally, in [011] crystals of steel II, twinning is not observed, whereas a high density of interstitial stacking faults and microtwinning is found in steel I [7, 10]. Therefore, higher values of θ in steel I are caused by the simultaneous action of slip and twinning and by the appearance of the additional substructural hardening due to interaction between twinning and slip (Fig. 2, curves *3* and *4*). In steel II, the planar dislocation structure and the development of multiple slip provide values of θ close to those found for steel I.

Thus, aluminum alloying of Hadfield steel increases the stacking fault energy of the matrix, reduces the contribution of mechanical twinning to strain, and gives rise to the development of the planar dislocation structure and to the high values of the strain hardening θ coefficient upon slip deformation.

ACKNOWLEDGMENTS

The work of Prof. Sehitoglu was supported by the National Science Foundation, grant no. CMS 99-00090, Mechanics and Materials Program, Arlington, Virginia. The part of the study carried out at Texas A&M University was supported by the National Science Foundation, grant no. CMS 01-34554, Solid Mechanics and Materials Engineering Program, Directorate of Engineering, Arlington, Virginia.

REFERENCES

1. K. S. Raghavan, A. S. Sastri, and M. J. Marcinkowski, Trans. TMS-AIME **245**, 1569 (1969).
2. P. H. Adler, G. B. Olson, and W. S. Owen, Metall. Trans. A **17**, 1725 (1986).
3. B. K. Zuidema, D. K. Subramanyam, and W. C. Leslie, Metall. Trans. A **18**, 1629 (1987).
4. Y. N. Dastur and W. C. Leslie, Metall. Trans. A **12**, 749 (1981).
5. W. S. Owen and M. Grujicic, Acta Mater. **47** (1), 111 (1998).
6. M. A. Shtremel' and I. A. Kovalenko, Fiz. Met. Metalloved. **63** (1), 172 (1987).
7. Yu. I. Chumlyakov, I. V. Kireeva, E. I. Litvinova, *et al.*, Phys. Met. Metallogr. **90** (Suppl. 1), 1 (2000).
8. Yu. I. Chumlyakov, H. Sehitoglu, I. V. Kireeva, *et al.*, Dokl. Akad. Nauk **361**, 192 (1998) [Dokl. Phys. **43**, 415 (1998)].
9. Yu. I. Chumlyakov, I. V. Kireeva, E. I. Litvinova, *et al.*, Dokl. Akad. Nauk **371**, 45 (2000) [Dokl. Phys. **45**, 101 (2000)].
10. E. G. Zakharova, I. V. Kireeva, Yu. I. Chumlyakov, *et al.*, Fiz. Mezomekh. **4** (2), 77 (2001).
11. L. Remy, Metall. Trans. A **12** (3), 387 (1981).
12. P. Mullner, S. Solenthaler, and M. O. Spiedel, in *Twinning in Advanced Materials*, Ed. by M. N. Yoo and M. Wutting (The Minerals, Metals and Materials Soc., Detroit, 1994), pp. 483–490.
13. I. Karaman, H. Sehitoglu, and Y. I. Chumlyakov, Scr. Mater. **38**, 1009 (1998).
14. I. Karaman, H. Sehitoglu, H. J. Maier, and Y. I. Chumlyakov, Acta Mater. **49**, 3919 (2001).
15. I. Karaman, H. Sehitoglu, K. Gall, *et al.*, Acta Mater. **48**, 1345 (2000).

Translated by T. Galkina

Doklady Physics, Vol. 47, No. 7, 2002, pp. 518–521. Translated from Doklady Akademii Nauk, Vol. 385, No. 1, 2002, pp. 57–60.

MECHANICS

Analysis of the Local-Equilibrium Approximation in the Problem of a Far Planar Turbulent Wake

V. N. Grebenev*, A. G. Demenkov, and G. G. Chernykh***

Presented by Academician Yu.I. Shokin February 13, 2002

Received February 26, 2002

Semiempirical models of turbulence, which include differential transport equations for the moments of hydrodynamic quantities [1], are among the basic methods of describing turbulence. In these models, the closure procedures for infinite systems of coupled equations for the moments often implicitly assume that these systems of differential equations allow the existence of invariant sets (manifolds). As is pointed out in [2], closure relations are, as a rule, derived using empirical hypotheses and certain assumptions, which are often poorly justified.

The correctness of replacing a differential equation by the corresponding closure relation is verified by investigating the consistency of the system used in the model of the *N*th order of closure with the differential constraint (i.e., with the algebraic relation). The method of differential constraints [3] provides the general approach to investigating overdetermined systems. This approach can be used to justify algebraic models applied to the calculation of the moments.

The invariant manifold introduced in [4] for an arbitrary system of evolution equations is a natural generalization of an invariant set of a system of ordinary differential equations and enables one to find certain classes of differential constraints. The invariant manifolds were used in [5, 6] for investigating the problem of the development of a shear-free mixing layer in the third-order closure model. Due to the differential constraints derived, it was established that the equation of the invariant manifold (differential constraint of the model) coincides with the classical tensor-invariant Hanjalic–Launder model [7] for an unstratified flow and with the Zeman–Lumley model [8] for a stratified flow. Reduction of the model on the invariant manifold made it possible to find self-similar solutions to the problem and to separate a class of particular solutions [9].

Local-equilibrium approximations of second-order moments are used while modeling turbulent flows (see, e.g., [10]). In this paper, we analyze these approximations by using the method of differential constraints. The dynamics of a far planar turbulent wake are investigated as an example. It is established that the application of the local-equilibrium approximation is associated with a vanishing of the Poisson bracket for the deviation of the averaged longitudinal velocity component U_1 and of the turbulence energy e. Numerical experiments carried out in the far wake verify this result.

1. EQUATIONS OF THE MODELS

Two mathematical models are used to describe a flow in a far plane turbulent wake. Model 1 is based on the classical (e, ϵ) model of turbulence [11]:

$$U_0\frac{\partial U_1}{\partial x} = \frac{\partial}{\partial y}\langle u'v'\rangle, \tag{1}$$

$$U_0\frac{\partial e}{\partial x} = \frac{\partial}{\partial y}\nu_{t_1}\frac{\partial e}{\partial y} + P - \epsilon, \tag{2}$$

$$U_0\frac{\partial \epsilon}{\partial x} = \frac{\partial}{\partial y}\nu_{t_2}\frac{\partial \epsilon}{\partial y} + \frac{\epsilon}{e}(C_{\epsilon_1}P - C_{\epsilon_2}\epsilon). \tag{3}$$

Here, U_0 is the remote velocity; $U_1 = U_0 - U$ is the deviation of the averaged longitudinal velocity component; the angle brackets $\langle\rangle$ indicate averaging; the coefficients of turbulent viscosity ν_{t_1} and ν_{t_2} have the form

$$\nu_{t_1} = C_\mu\frac{e^2}{\epsilon}, \quad \nu_{t_2} = \frac{\nu_{t_1}}{\sigma_\epsilon}; \tag{4}$$

e is the turbulence energy; ϵ is the rate of dissipation of turbulence energy into heat; and

$$P = \langle u'v'\rangle\frac{\partial U_1}{\partial y}$$

*Institute of Computer Technologies,
Siberian Division, Russian Academy of Sciences,
pr. Akademika Lavrent'eva 6, Novosibirsk, 630090 Russia

** Kutateladze Institute of Thermal Physics,
Siberian Division, Russian Academy of Sciences,
pr. Akademika Lavrent'eva 1, Novosibirsk, 630090 Russia

1028-3358/02/4707-0518$22.00

describes the generation of turbulence energy due to gradients of the averaged velocity, where

$$\langle u'v' \rangle = C_\mu \frac{e^2}{\epsilon} \frac{\partial U_1}{\partial y} \equiv C_\mu e \hat{\tau} \frac{\partial U_1}{\partial y} \quad (5)$$

with $\hat{\tau} = \frac{e}{\epsilon}$. In model 2, the tangential Reynolds stress $\langle u'v' \rangle$ is determined from the differential equation [12]

$$U_0 \frac{\partial \langle u'v' \rangle}{\partial x} = \frac{\partial}{\partial y} \nu_{t_3} \frac{\partial \langle u'v' \rangle}{\partial y} - C_{\phi_1} \langle u'v' \rangle \frac{\epsilon}{e} + C_{\phi_2} e \frac{\partial U_1}{\partial y}, \quad (6)$$

where $\nu_{t_3} = C_s C_\mu^{-1} \nu_{t_1}$. Thus, mathematical model 2 includes Eqs. (1)–(3) and (6). Relation (5) follows from Eq. (6) in the approximation of local equilibrium. The quantities σ_ϵ, C_{ϵ_1}, C_{ϵ_2}, C_μ, C_{ϕ_1}, C_{ϕ_2}, and C_s are empirical constants ($C_{\phi_2} = C_{\phi_1} C_\mu$). Dimensionless variables are introduced by using the body diameter D and the velocity U_0 as scales of length and velocity, respectively.

The above mathematical models are the simplest ones. For better agreement with experimental data, one should use much more complicated mathematical models, which have not yet been analyzed.

2. INVARIANT MANIFOLD OF MODEL 2

The algebraic model of local-equilibrium approximation (5) is derived from the closed equations of model 2 by assuming that terms describing convective and diffusive transfer in (6) are negligible. The correct choice of an operator dominating in an equation at a certain stage of flow development requires the estimation of the joint contribution from all terms of the equation and must be justified (or refuted) by a certain formal procedure based only on the equations of the model.

We consider the set $\mathcal{D}$

$$\mathcal{D} = \left\{ e, \hat{\tau}, U, \langle u'v' \rangle : \mathcal{G}^1(e, \hat{\tau}, U, \langle u'v' \rangle) \equiv \langle u'v' \rangle - C_\mu \hat{\tau} e \frac{\partial U_1}{\partial y} = 0 \right\}. \quad (7)$$

Derivation of Eq. (5) can be related to the invariance of the set $\mathcal{D}$ with respect to the flux generated by system (1)–(3), (6).

Below, we review certain definitions from [4]. Let

$$u_t^i = F^i(t, x, u^1, \ldots, u^m, u_x^1, u_x^2, \ldots), \quad i = 1, 2, \ldots, m$$

be the system of evolution equations E. The system is complemented by differential constraints H of the form

$$h_j(t, x, u^1, \ldots, u^m, u_x^1, u_x^2, \ldots) = 0, \quad j = 1, 2, \ldots, p,$$

where $p \geq m$. The expression $G|_M = 0$ means that a certain equality $G = 0$ is satisfied on the set M. The differential constraints H define the invariant manifold of the system E if the equalities

$$D_t(h_j)|_{[E] \cup [H]} = 0, \quad j = 1, 2, \ldots, p \quad (8)$$

are satisfied. Here, the square brackets denote both the system of equations and its differential corollaries with respect to x.

Solutions to the equation for $\hat{\tau}$

$$\frac{\partial \hat{\tau}}{\partial x} = \frac{1}{\epsilon} \frac{\partial e}{\partial x} - \frac{e}{\epsilon^2} \frac{\partial \epsilon}{\partial x} = U_0^{-1} \left\{ \frac{1}{\epsilon} \frac{\partial}{\partial y} \nu_{t_1} \frac{\partial e}{\partial y} + \frac{P}{\epsilon} - 1 - \frac{e}{\epsilon^2} \frac{\partial}{\partial y} \nu_{t_2} \frac{\partial \epsilon}{\partial y} + \frac{1}{\epsilon} (C_{\epsilon_1} P - C_{\epsilon_2} \epsilon) \right\}$$

$$= U_0^{-1} \left\{ \frac{1}{\epsilon} \frac{\partial}{\partial y} C_\mu \hat{\tau}^2 e \frac{\partial \epsilon}{\partial y} + \frac{1}{\epsilon} \frac{\partial}{\partial y} C_\mu \hat{\tau} e \epsilon \frac{\partial \hat{\tau}}{\partial y} + \frac{P}{\epsilon} - 1 - \frac{1}{\epsilon} \hat{\tau} \frac{\partial}{\partial y} \frac{C_\mu}{\sigma_\epsilon} \hat{\tau} e \frac{\partial \epsilon}{\partial y} - \frac{1}{\epsilon} C_{\epsilon_1} P + C_{\epsilon_2} \right\}$$

are important for proving the invariance of the set $\mathcal{D}$. At $\sigma_\epsilon = 1$ (this value is recommended in [11]) and $C_{\epsilon_1} = 1$ (the recommended value is equal to 1.4), the equation has the solution

$$\hat{\tau}(x, y) \equiv \hat{\tau}_h(x) = U_0^{-1} (C_{\epsilon_2} - 1)(x + x_0).$$

The theorem below provides the criterion of the invariance of $\mathcal{D}$.

Theorem 2.1. *Let* $(U_1, e, \epsilon, \langle u'v' \rangle)$ *be a sufficiently smooth solution to system* (1)–(3), *and* (6), *and let* $\sigma_\epsilon = C_{\epsilon_1} = 1$. *Let us suppose that* $C_{\phi_1} - C_{\phi_2} C_\mu = C_\mu (C_{\epsilon_2} - 1)$. *Then, the set* $\mathcal{D}$ *is the invariant manifold of system* (1)–(3) *and* (6) *at* $\hat{\tau} = \hat{\tau}_h$ *if and only if the Poisson bracket is* $\{e, U_1\} = 0$.

Remark 2.1. *Using the constants* C_{ϕ_1}, C_μ, *and* C_{ϵ_2} *recommended in* [12], *one finds that the right-hand side of the relation* $C_{\phi_2} - C_{\phi_1} C_\mu = C_\mu (C_{\epsilon_2} - 1)$ *is equal to* 0.081. *Therefore,* C_{ϕ_2} *differs only slightly from* $C_{\phi_2} C_\mu =$

Table 1. Variation of $\delta^{\tilde{n}}$ as a function of the distance from the body

I	II	III	IV
725	0.19×10^{-6}	0.19×10^{-6}	0.19×10^{-6}
925	0.11×10^{-6}	0.11×10^{-6}	0.11×10^{-6}
1125	0.66×10^{-7}	0.65×10^{-7}	0.65×10^{-7}
1425	0.35×10^{-7}	0.32×10^{-7}	0.32×10^{-7}

Table 2. Axial values of $(e_0^{(1)})$ turbulence energy, $(\varepsilon_0^{(1)})$ dissipation rate, and $(U_{d0}^{(1)})$ the deviation of the longitudinal velocity component according to model 1

$\frac{x}{D}$	$e_0^{(1)}$	$\varepsilon_0^{(1)}$	$U_{d0}^{(1)}$
725	0.145×10^{-3}	0.253×10^{-6}	0.357×10^{-1}
925	0.112×10^{-3}	0.148×10^{-6}	0.335×10^{-1}
1125	0.929×10^{-4}	0.992×10^{-7}	0.316×10^{-1}
1425	0.749×10^{-4}	0.626×10^{-7}	0.294×10^{-1}

Table 3. The same as in Table 2, but according to model 2

$\frac{x}{D}$	$e_0^{(2)}$	$\varepsilon_0^{(2)}$	$U_{d0}^{(2)}$
725	0.145×10^{-3}	0.253×10^{-6}	0.358×10^{-1}
925	0.113×10^{-3}	0.148×10^{-6}	0.335×10^{-1}
1125	0.930×10^{-4}	0.996×10^{-7}	0.316×10^{-1}
1425	0.747×10^{-4}	0.631×10^{-7}	0.294×10^{-1}

0.252 *and is close to its value* $C_{\phi_2} = C_{\phi_1} C_\mu$ *recommended in* [11, 12].

The simple examples of flows where the Poisson bracket is $\{e, U_1\} = 0$ are as follows: (i) a shear-free flow with zero deviation of the averaged longitudinal velocity component ($U_1 = 0$), (ii) a flow with the degenerate components $e_x = U_{1x} = 0$, and (iii) a flow with equal rates of the generation and dissipation of turbulence energy, i.e., $P = \epsilon$.

3. RESULTS OF NUMERICAL EXPERIMENTS

To illustrate the above statement, we have carried out a series of numerical experiments by using models 1 and 2. Initial conditions specified at $\frac{x_0}{D} = 625$ are in agreement with experimental data on the degeneration of a planar turbulent wake behind a round cylinder [13]. The initial distribution of the tangential stress $\langle u'v' \rangle$ is specified by Eq. (5). A finite-difference algorithm, its test and realization, and the results of its application to the problems of freestream turbulence were detailed in [14, 15]. The calculations are performed to double accuracy. Table 1 presents the quantity

$$\delta^{\tilde{n}} = \frac{\max_j \left| (U_{1x}^h e_y^h)_j^{\tilde{n}} - (U_{1y}^h e_x^h)_j^{\tilde{n}} \right|}{\max_j (\left| \nabla^h e_j \right|, \left| \nabla^h U_1 \right|_j)},$$

which is considered as a function of the distance from the body and, at $x = x^{\tilde{n}}$, characterizes the mesh analog of the Poisson bracket. Here, $(U_{1x}^h)_j$, $(U_{1y}^h)_j$, $(e_x^h)_j$, $(e_y^h)_j$, $(\nabla^h e)_j$, and $(\nabla^h U_1)_j$ are the finite-difference approximations of the first derivatives and gradients at the node $y = y_j$ ($j = 1, 2, \ldots, N_y - 1$). Column I shows the distance from the body $\frac{x}{D}$, and columns II, III, and IV present $\delta^{\tilde{n}}$ in the uniform meshes 1–3 with the parameters $h_x = 0.5$, $h_y = 0.1$; $h_x = 0.25$, $h_y = 0.05$; and $h_x = 0.125$, $h_y = 0.025$, respectively.

The calculations are based on model 2 and indicate that the mesh analog of the Poisson bracket is close to zero for all mesh parameters.

Tables 2 and 3 present the axial values calculated in models 1 and 2, respectively, for the turbulence energy $e_0 = e_0(x) = e(x, 0)$, the rate of energy dissipation $\varepsilon_0 = \varepsilon_0(x) = \varepsilon(x, 0)$, and of deviation of the longitudinal velocity component $U_{d0} = U_1(x, 0)$. According to these data, which were obtained with the mesh parameters $h_x = 0.25$ and $h_y = 0.05$, wake parameters calculated in models 1 and 2 are close to each other. The difference between the corresponding arrays of U_1, e, and ε is no more than the difference between the respective axial values.

Thus, the above theorem and the calculations show that the approximation of local equilibrium is applicable for determining the tangential Reynolds stress $\langle u'v' \rangle$ in the dynamic problem of the far turbulent wake behind a round cylinder.

ACKNOWLEDGMENTS

This work was supported by the Russian Foundation for Basic Research, project no. 01-01-00783, and by Siberian Division, Russian Academy of Sciences, integration project no. 2000-1.

REFERENCES

1. A. S. Monin and A. M. Yaglom, *Statistical Fluid Mechanics* (Gidrometeoizdat, Leningrad, 1992; MIT Press, Cambridge, Mass., 1971), Vol. 1.
2. A. Chorin, in *Lecture Notes in Mathematics* (Springer-Verlag, Berlin, 1977), Vol. 615.

3. A. F. Sidorov, V. P. Shapeev, and N. N. Yanenko, *The Method of Differential Constraints and Its Application in Gas Dynamics* (Nauka, Novosibirsk, 1984).
4. V. K. Andreev, O. V. Kaptsov, V. V. Pukhnachev, and A. A. Rodionov, *Application of the Group Theoretical Methods in Hydrodynamics* (Nauka, Novosibirsk, 1994).
5. V. N. Grebenev and B. B. Ilyushin, Dokl. Akad. Nauk **374** (6), 761 (2000) [Dokl. Phys. **45**, 550 (2000)].
6. V. N. Grebenev, B. B. Ilyushin, and Yu. I. Shokin, J. Nonlinear Sci. Numer. Simulation **1** (4), 305 (2000).
7. K. Hanjalic and B. E. Launder, J. Fluid Mech. **52**, 609 (1972).
8. O. Zeman and J. L. Lumley, J. Atmos. Sci. **33**, 1974 (1976).
9. V. N. Grebenev and B. B. Ilyushin, J. Nonlinear Math. Phys. **9** (2), 144 (2002).
10. W. Lewellen, in *Handbook of Turbulence*, Vol. 1: *Fundamentals and Applications*, Ed. by W. Frost and T. Mouladen (Plenum, New York, 1977; Mir, Moscow, 1980).
11. P. Harsha, in *Handbook of Turbulence*, Vol. 1: *Fundamentals and Applications*, Ed. by W. Frost and T. Mouladen (Plenum, New York, 1977; Mir, Moscow, 1980).
12. K. Hanjalic and B. E. Launder, J. Fluid Mech. **51,** 301 (1972).
13. A. A. Townsend, *The Structure of Turbulent Shear Flow* (Cambridge Univ. Press, Cambridge, 1956; Inostrannaya Literatura, Moscow, 1959).
14. A. G. Demenkov and G. G. Chernykh, Vychisl. Tekhnol. **4** (12), 119 (1995).
15. G. G. Chernykh and A. G. Demenkov, Russ. J. Numer. Anal. Math. Model. **12** (2), 111 (1997).

Translated by Yu. Verevochkin

Doklady Physics, Vol. 47, No. 7, 2002, pp. 522–524. Translated from Doklady Akademii Nauk, Vol. 385, No. 1, 2002, pp. 61–63.

MECHANICS

Tension of a Piezoelectric Ceramic Layer Weakened by Through-Tunnel Cavities

Corresponding Member of the RAS É. I. Grigolyuk*, L. A. Fil'shtinskiĭ, and Yu. D. Kovalev****

Received February 15, 2002

The bending of an isotropic layer (half-layer) weakened by a noncircular through hole was analyzed in [1]. A similar problem for an isotropic layer with a round hole was solved in [2] by other methods. In many studies of a stressed state in a piecewise uniform layer, the solutions to boundary value problems are determined by the Vorovich semi-inverse method [3]. In this paper, we propose a new analytical procedure for investigating the coupled electroelastic fields in a layer weakened by cavities of quite arbitrary cross sections.

We consider a piezoelectric ceramic layer

$$-h \le x_3 \le h, \quad -\infty < x_1, x_2 < \infty$$

weakened by through cavities tunneling along the Ox_3 axis, which are holes whose cross sections are quite smooth, closed contours L_j, $j = 1, 2, \ldots, k$, $\cap L_j = \emptyset$. We assume that the layer ends are covered with a diaphragm, which is rigid in its plane and flexible in the perpendicular direction. Let a stress vector (N, T, Z) act on the lateral sides of the cavities and a uniform field of tension and shear σ_{11}^{∞}, σ_{22}^{∞}, and σ_{12}^{∞} exist at infinity.

The complete set of equations determining a solution to the above problem (in the absence of bulk stresses and charges in the body) involves the following equations:

(i) the equations of equilibrium

$$\partial_j \sigma_{ij} = 0, \quad \partial_i = \frac{\partial}{\partial x_i}, \quad i, j = 1, 2, 3, \tag{1}$$

where summation over repeated subscripts is implied;

(ii) the equations of electrostatics

$$\partial_m D_m = 0, \quad E_m = -\partial_m \varphi; \tag{2}$$

(iii) the Cauchy relations

$$\varepsilon_{ij} = \frac{1}{2}(\partial_i u_j + \partial_j u_i); \tag{3}$$

(iv) the equations of state for a piezoelectric ceramic material preliminarily polarized along the Ox_3 axis [4]

$$\begin{aligned}
\sigma_x &= c_{11}\varepsilon_x + c_{12}\varepsilon_y + c_{13}\varepsilon_z - e_{31}E_z,\\
\tau_{yz} &= 2c_{44}\varepsilon_{yz} - e_{15}E_y,\\
\sigma_y &= c_{12}\varepsilon_x + c_{11}\varepsilon_y + c_{13}\varepsilon_z - e_{31}E_z,\\
\tau_{xz} &= 2c_{44}\varepsilon_{xz} - e_{15}E_x,\\
\sigma_z &= c_{13}(\varepsilon_x + \varepsilon_y) + c_{33}\varepsilon_z - e_{33}E_z,\\
\tau_{xy} &= (c_{11} - c_{12})\varepsilon_{xy},\\
D_x &= \varepsilon_{11}E_x + 2e_{15}\varepsilon_{xz}, \quad D_y = \varepsilon_{11}E_y + 2e_{15}\varepsilon_{yz},\\
D_z &= \varepsilon_{33}E_z + e_{31}(\varepsilon_x + \varepsilon_y) + e_{33}\varepsilon_z;
\end{aligned} \tag{4}$$

(v) the boundary conditions on the layer bases $x_3 = \pm h$

$$u_1 = 0, \quad u_2 = 0, \quad \sigma_{33} = 0, \quad D_3 = 0; \tag{5}$$

(vi) and the boundary conditions on the cavity surface

$$\begin{aligned}
\sigma_{kj} n_j &= P_k, \quad k, j = 1, 2, 3,\\
D_n &= 0, \quad P_1 = N\cos\psi - T\sin\psi,\\
P_2 &= N\sin\psi + T\cos\psi, \quad P_3 = Z.
\end{aligned} \tag{6}$$

In what follows, it is appropriate to use the set of equations of equilibrium in terms of displacements. This set follows from Eqs. (1)–(4) as

$$\begin{aligned}
&V\nabla^2 u + c_{44}\partial_3^2 u + \partial_1\theta = 0,\\
&V\nabla^2 v + c_{44}\partial_3^2 v + \partial_2\theta = 0, \quad \nabla^2 = \partial_1^2 + \partial_2^2,\\
&c_{44}\nabla^2 w + c_{33}\partial_3^2 w\\
&+ \partial_3\{c(\partial_1 u + \partial_2 v) + e_{15}\nabla^2\varphi + e_{33}\partial_3^2\varphi\} = 0,\\
&\varepsilon_{11}\nabla^2\varphi + \varepsilon_{33}\partial_3^2\varphi - e_{15}\nabla^2 w\\
&- e_{33}\partial_3^2 w - \partial_3\{e(\partial_1 u + \partial_2 v)\} = 0,
\end{aligned} \tag{7}$$

$$U = -\frac{1}{2}(c_{11} + c_{12}), \quad V = -\frac{1}{2}(c_{11} - c_{12}),$$

$$c = c_{13} + c_{44}, \quad e = e_{15} + e_{31},$$

* *Moscow State Academy of Automobile and Tractor Engineering (MAMI), Bol'shaya Semenovskaya ul. 38, Moscow, 105839 Russia*

** *Sumy State University, ul. Rimskogo-Korsakova 2, Sumy, 40007 Ukraine*

1028-3358/02/4707-0522$22.00

$$\theta = U(\partial_1 u + \partial_2 v) + c\partial_3 w + e\partial_3 \varphi,$$
$$u_1 = u, \quad u_2 = v, \quad u_3 = w.$$

We seek a solution to set (7) that is symmetric about the median plane $x_3 = 0$ of the layer. We set

$$\{u, v\} = \sum_{k=0}^{\infty} \{u_k, v_k\} \cos\gamma_k x_3, \quad \gamma_k = \frac{2k+1}{2h}\pi,$$
$$\{w, \varphi\} = \sum_{k=0}^{\infty} \{w_k, \varphi_k\} \sin\gamma_k x_3. \tag{8}$$

In view of these relations, Eqs. (7) yield

$$V\kappa_k u_k + \partial_1 \theta_k = 0, \quad V\kappa_k v_k + \partial_2 \theta_k = 0,$$
$$L_{13} w_k + L_{14}\varphi_k + \frac{c}{U}\gamma_k \theta_k = 0,$$
$$L_{23} w_k + L_{24}\varphi_k + \frac{e}{U}\gamma_k \theta_k = 0,$$

$$\kappa_k = \nabla^2 - \gamma_k^2 \mu_0^2, \quad L_{13} = c_{44}\nabla^2 - \gamma_k^2 \delta_1, \quad \mu_0^2 = \frac{c_{44}}{V}, \tag{9}$$
$$L_{14} = L_{23} = e_{15}\nabla^2 - \gamma_k^2 \delta_2, \quad L_{24} = \gamma_k^2 \delta_3 - \varepsilon_{11}\nabla^2,$$
$$\theta_k = U(\partial_1 u_k + \partial_2 v_k) + \gamma_k c w_k + \gamma_k e \varphi_k,$$
$$\delta_1 = c_{33} - \frac{c^2}{U}, \quad \delta_2 = e_{33} - \frac{ce}{U}, \quad \delta_3 = \varepsilon_{33} + \frac{e^2}{U}.$$

The integration of this set gives

$$u_k - iv_k = 2\gamma_k \frac{U}{V} \sum_{m=1}^{3} \frac{p_4^*(\mu_m)}{\mu_m^2 - \mu_0^2} \frac{\partial}{\partial z} \Omega_k^{(m)} + 2i \frac{\partial}{\partial z} \Omega_k,$$

$$w_k = \gamma_k^2 \sum_{m=1}^{3} (d_2 \mu_m^2 - \delta_5) \Omega_k^{(m)}, \quad k = 0, 1, \ldots,$$
$$\varphi_k = \gamma_k^2 \sum_{m=1}^{3} (\delta_4 - d_1 \mu_m^2) \Omega_k^{(m)}, \tag{10}$$
$$\delta_4 = \frac{\delta_1}{c} - \frac{\delta_2}{e}, \quad \delta_5 = \frac{\delta_2}{c} + \frac{\delta_3}{e},$$

where the function $\Omega_k^{(m)}$ is an arbitrary solution to the Helmholtz equation $(\nabla^2 - \gamma_k^2 \mu_m^2)\Omega_k^{(m)} = 0$; Ω_k is an arbitrary solution to the equation $(\nabla^2 - \gamma_k^2 \mu_0^2)\Omega_k = 0$; μ_m, $m = 1, 2, 3$, are the roots of the bicubic equation [5]; and d_k are known constants depending on the physical and mechanical characteristics of the piezoelectric ceramic material.

The functions $\Omega_k^{(m)}$ and Ω_k determine the potential and vortex components of the solution, respectively. As follows from Eq. (10), the above homogeneous solutions are free of the biharmonic part.

The desired metaharmonic functions appearing in Eq. (10) are sought in the following form of simple-

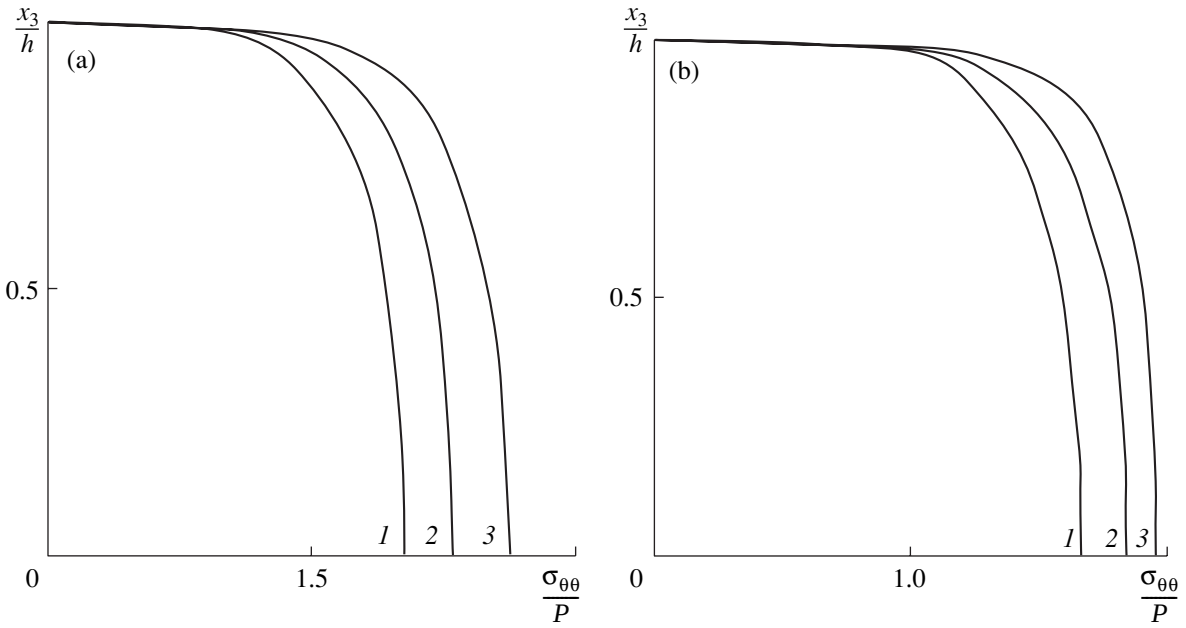

Fig. 1. Distribution of the relative circular stress $\frac{\sigma_{\theta\theta}}{P}$ in the thickness coordinate for (a) $R_1 = R_2 = 1$ and (b) $R_1 = 2R_2 = 1$. Lines *1*, *2*, and *3* are for $\frac{h}{R_1} = 1$, 2, and 4, respectively.

layer potentials [6]:

$$\Omega_k = \int_L p_k(\zeta) K_0(\gamma_k \mu_0 r) ds, \quad r = |\zeta - z|,$$
$$z = x_1 + i x_2,$$
$$\Omega_k^{(m)} = \int_L p_k^{(m)}(\zeta) K_0(\gamma_k \mu_m r) ds, \tag{11}$$
$$\zeta = \xi_1 + i\xi_2 \in L = \cup L_j, \quad m = 1, 2, 3,$$

where $K_n(z)$ is an nth-order modified Bessel function of the second kind and $p_k(\zeta)$ and $p_k^{(m)}(\zeta)$ are the desired densities such that $p_k^{(3)} = \bar{p}_k^{(2)}$.

We assume that the components of the stress vector and the normal component of the electric displacement vector, which act on the cavity surface, can be decomposed as

$$N = \sum_{k=0}^{\infty} N_k \cos\gamma_k x_3, \quad T = \sum_{k=0}^{\infty} T_k \cos\gamma_k x_3,$$
$$Z = \sum_{k=0}^{\infty} Z_k \sin\gamma_k x_3, \quad D_n = \sum_{k=0}^{\infty} D_n^{(k)} \sin\gamma_k x_3. \tag{12}$$

It is appropriate to represent the boundary conditions on the cavity surface in the form

$$\sigma_{11}^* + \sigma_{22}^* - e^{2i\psi}(\sigma_{22}^* - \sigma_{11}^* + 2i\sigma_{12}^*) = 2(N - iT),$$
$$\mathrm{Re}\{e^{i\psi}(\sigma_{13} - i\sigma_{23})\} = Z, \quad \sigma_{kj}^* = \sigma_{kj} + \sigma_{kj}^{\infty}, \tag{13}$$
$$D_n = 0,$$

where ψ is the angle between the positive normal to the contour L and Ox_1 axis, N and T are the normal and tangential components of the stress vector (N, T, Z) acting on the body surface from the outer normal, and σ_{kj} are the stress-tensor components.

Representation (11) and decompositions (8) and (12) enable us to reduce boundary value problem (13) to a set of four (for each k) singular integro-differential equations, which is solved numerically by the method of mechanical quadratures [7].

As an example, we consider a layer weakened by an elliptic-section through-tunnel cavity free of stresses ($\xi_1 = R_1\cos\varphi$, $\xi_2 = R_2\sin\varphi$, $0 \le \varphi \le 2\pi$) when a tensile load $\sigma_{11}^{\infty} = P = \text{const}$ acts at infinity.

Figures 1a and 1b show the distribution of the relative circular stress $\frac{\sigma_{\theta\theta}}{P}$ in the thickness coordinate at the point $\varphi = \frac{\pi}{2}$, where the stress is maximal, for $R_1 = R_2 = 1$ and $R_1 = 2R_2 = 1$, respectively. Lines *1*, *2*, and *3* are for $\frac{h}{R_1} = 1$, 2, and 4, respectively. The numerical results were obtained for the piezoelectric ceramic material PZT-4, whose characteristics were taken from [4, 8].

REFERENCES

1. É. I. Grigolyuk, Yu. D. Kovalev, and L. A. Fil'shtinskiĭ, Dokl. Akad. Nauk **345** (1), 54 (1995) [Phys. Dokl. **40**, 592 (1995)].
2. A. F. Ulitko, *The Method of Vector Eigenfunctions in* 3D *Problems of Elasticity Theory* (Naukova Dumka, Kiev, 1979).
3. I. I. Vorovich and O. S. Malkina, Prikl. Mat. Mekh. **31** (2), 230 (1967).
4. V. T. Grinchenko, A. F. Ulitko, and N. A. Shul'ga, *The Mechanics of Connected Fields in the Elements of Constructions. Electroelasticity* (Naukova Dumka, Kiev, 1989), Vol. 5.
5. L. A. Fil'shtinskiĭ, Teor. Prikl. Mekh. (Kiev), No. 21, 13 (1990).
6. V. S. Vladimirov, *Equations of Mathematical Physics* (Nauka, Moscow, 1981; Marcel Dekker, New York, 1971).
7. S. M. Belotserkovskiĭ and I. K. Lifanov, *Numerical Methods in Singular Integral Equations* (Nauka, Moscow, 1985).
8. D. Berlincourt, D. R. Curran, and H. Jaffe, Piezoelectric and Piezomagnetic Materials and Their Function in Transducers, in *Physical Acoustics: Principles and Methods*, Vol. 1, Part A: *Methods and Devices*, Ed. by W. P. Mason (Academic, New York, 1964; Mir, Moscow, 1966).

Translated by R. Tyapaev

Doklady Physics, Vol. 47, No. 7, 2002, pp. 525–527. Translated from Doklady Akademii Nauk, Vol. 385, No. 1, 2002, pp. 64–66.

MECHANICS

Transition between Brittle and Ductile Erosional Fracture

Academician N. F. Morozov*, Yu. V. Petrov, and V. I. Smirnov*****

Received March 6, 2000

Generally, analysis of surface erosion by solid-particle impact should be conducted by invoking the apparatus of fracture mechanics. However, conventional quasi-static modeling cannot provide explanations of many observed effects, because static criteria are inconsistent with the essential dynamics of erosion.

Erosion processes are characterized by the action of very short dynamic stress pulses on surfaces. The possibility of fracture can be assessed only by means of criteria taking into account the transient nature of the fracture of solids. An efficient criterion for analyzing rapid fracture processes is based on the concept of latent time [1, 2]. For a defect-free material subject to erosion, the criterion is formulated as

$$\int_{t-\tau}^{t} \sigma(s)ds \le \sigma_s\tau, \qquad (1)$$

where τ is the latent time of fracture, σ_s is the static tensile strength of the material, and $\sigma(t)$ is the maximal tensile stress.

Fractographic studies show that a key factor in erosional fracture is the development of circular brittle cracks induced by impacting solid particles whose radii vary from tens to hundreds of microns [3]. Their impact on the surface gives rise to extremely short fracturing pulses. Knowing their characteristics and the threshold velocity for impact fracture, we can determine an elementary "quantum" of action resulting in fracture [1] and the corresponding latent time. Moreover, if the parameters used in the fracture criterion are known, we can calculate some basic characteristics of the erosion process. This approach can be developed in the simplest approximation by invoking the Hertz impact theory [4].

Suppose that a single solid particle of radius R moving at a velocity v hits the surface of an elastic material occupying a half-space. The time-dependent maximal (radial) fracturing stress at a point adjacent to the contact area is calculated (in a cylindrical coordinate system) by the formula [4, 5]

$$\sigma_r(v, R, t) = \frac{1-2\nu}{2}\frac{k\sqrt{h(t)}}{\pi R}, \qquad (2)$$

where the function $h(t)$ is expressed as [6]

$$h(t) \approx 0.995h_0\sin\left(\frac{\pi t}{t_0}\right). \qquad (3)$$

Here, $h_0 = \left(\frac{5mv^2}{4k}\right)^{5/2}$ is the particle penetration depth and $t_0 \approx 2.9432\frac{h_0}{v}$ is the contact duration; $k = \frac{4}{3}\frac{\sqrt{R}E}{1-\nu^2}$, where E is the elastic modulus; and ν is the Poisson ratio.

Suppose that v equals the threshold particle velocity corresponding to the onset of fracture. Introducing the function

$$f(v, R, \tau) = \max_t \int_{t-\tau}^{t} \sigma_r(v, R, s)ds - \sigma_s\tau \qquad (4)$$

and using the latent-time criterion, we determine the latent time as the positive root of the equation

$$f(v, R, \tau) = 0 \qquad (5)$$

for given values of v and R.

We can now calculate the latent time by using experimental values of the threshold velocity for erosional fracture of surfaces and the formulas written out above.

We consider the erosional fracture of B95 aluminum alloy with the following mechanical properties: E = 73 GPa, ν = 0.3, σ_s = 456 MPa, the static fracture toughness K_{Ic} = 37 MPa $\sqrt{\text{m}}$, and the acoustic velocity c = 6500 m/s. The radius of an erosive particle is R = 150 μm, and its density is ρ = 2400 kg/m^3 (its mass is

* *Faculty of Mechanics and Mathematics, St. Petersburg State University, Bibliotechnaya pl. 2, Staryĭ Petergof, 198904 Russia*

** *Institute for Transportation Problems, Russian Academy of Sciences, Dvenadtsataya liniya 13, Vasil'evskiĭ ostrov, St. Petersburg, 199178 Russia*

*** *St. Petersburg Transport University, Moskovskiĭ pr. 9, St. Petersburg, 199103 Russia*

1028-3358/02/4707-0525$22.00 © 2002 MAIK "Nauka/Interperiodica"

calculated as $m = \frac{4\pi\rho R^3}{3}\Big)$. For the aluminum alloy with the mechanical properties defined above, the threshold impact velocity for erosional fracture has been determined experimentally: $v = 33$ m/s [7]. Using the above formulas to evaluate the impact characteristics for a particle interacting with a surface, we obtain $t_0 = 0.29$ μs and $h_0 = 3.46$ μm. Our analysis shows that the function $f(v, R, \tau)$ has a unique positive root. The latent time calculated for the material properties specified above is $\tau \approx 0.71$ μs. Note that a similar value of the latent time can be obtained from the formula $\frac{d}{c} \approx 0.65$ μs, where $d = \frac{2K_{Ic}^2}{\pi\sigma_c^2}$.

The reverse situation is also valid. Knowing the latent time for a material (e.g., from spall tests), we can calculate the key characteristics of the erosion process. Curve *1* in Fig. 1 represents the threshold velocity for erosional fracture calculated for the B95 alloy as a function of the erosive-particle radius for $\tau = 0.71$ μs. The curve consists of a quasi-static branch and a dynamic branch. The former branch is characterized by a weak dependence of the threshold velocity on the erosive-particle size, whereas the latter branch demonstrates a relatively steep (power-law) increase in the threshold velocity with decreasing particle size. Note the sharp transition between the quasi-static and dynamic regimes at a certain particle size (on the order of hundreds of microns in the present case). The theoretical curve shown here is qualitatively consistent with available experimental data [8]. It should also be noted that the dependence calculated by using the conventional critical-stress criterion in the scheme outlined above (curve *2* in Fig. 1) fails to explain the observed behavior of the threshold velocity for erosional fracture.

From a practical standpoint, it is also important to examine the possibility of ductile fracture in the region of contact between an erosive particle and the surface of a material occupying a half-space. Fracture of this type is observed experimentally in the form of plastic prints. To analyze it, we invoke the dynamic yield criterion given in [9]:

$$\int_{t-\tau_Y}^{t} \left(\frac{\sqrt{3}T_s(s)}{\sigma_Y}\right)^{\alpha} ds \le \tau_Y. \qquad (6)$$

Here, $T_s(t)$ is the tangential stress intensity defined as

$$T_s^2(t) = \frac{1}{6}\{[\sigma_r(t) - \sigma_\theta(t)]^2 + [\sigma_\theta(t) - \sigma_z(t)]^2 + [\sigma_z(t) - \sigma_r(t)]^2\},$$

in terms of the stress-tensor components σ_z, σ_r, and σ_θ in a cylindrical coordinate system; α is an empirical constant parameter characterizing the material used; σ_Y is the yield stress determined under uniaxial quasi-static loading; and τ_Y is the corresponding latent (structural) time. Criterion (6) is valid in the cases of both uniaxial loading and pure shear. The static yield criterion (the von Mises criterion), which corresponds to the case of slowly varying load, is obtained by taking the limit as $\frac{\tau_Y}{t_0} \longrightarrow 0$, where t_0 is the characteristic loading time.

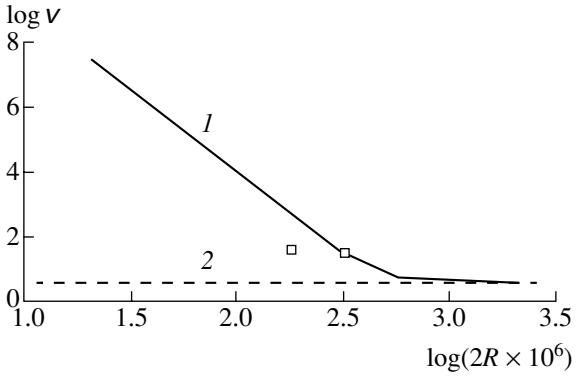

Fig. 1. Threshold velocity v (m/s) as a function of the particle radius R (m).

The tangential stress intensity on the surface reaches its maximum at the origin of the coordinate system, where $\sigma_r = \sigma_\theta$ and

$$T_s(v, R, t) = \frac{3(1-2\nu)}{4\sqrt{3}} \frac{k\sqrt{h(t)}}{\pi R} \qquad (7)$$

with $h(t)$ given by (3).

To predict ductile fracture for the B95 alloy, we set $\alpha = 2$ (see [10]) and $\tau_Y = 5$ μs. By analogy with (4), we define the function

$$F(v, R, \tau_Y) = \max_t \int_{t-\tau_Y}^{t} \left[\frac{\sqrt{3}T_s(v, R, s)}{\sigma_Y}\right]^{\alpha} ds - \tau_Y \qquad (8)$$

and use it to numerically evaluate the threshold velocity for ductile fracture as a function of the erosive-particle radius. Figure 2 compares the threshold velocities for brittle and ductile fracture (curves *2* and *1*, respectively). As is seen, for small radii ($R \le 140$ μm), an increase in the impact velocity causes the material to yield, and a further increase in velocity leads to the development of cracks. As the particle size increases,

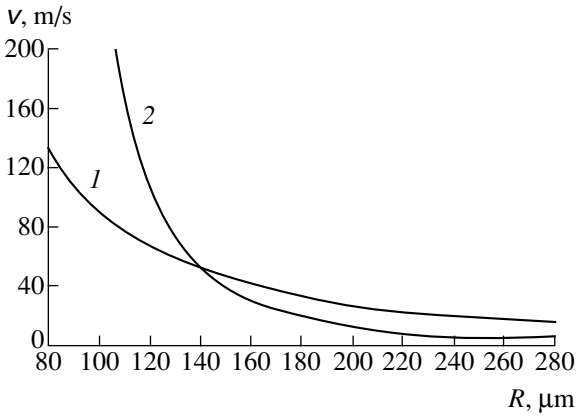

Fig. 2. Threshold velocities for erosional fracture of the B95 alloy: (*1*) ductile fracture; (*2*) brittle fracture.

the mechanism of fracture changes. With further increase in radius, the fracture curves tend to converge, suggesting that transition between fracture mechanisms (from ductile to brittle fracture and vice versa) is possible. The point of crossover between curves *1* and *2* corresponds to the threshold velocity for fracture at which the fracture mechanism changes. For the mechanical parameters specified above, the point has the coordinates $R \approx 140$ μm and $v_* \approx 56$ m/s. An increase in the impact velocity facilitates transition from ductile to brittle fracture.

The theoretical curves presented here demonstrate the substantial effect of the size of erosive particles on the threshold velocity for erosional fracture and, therefore, on the erosional-wear intensity [3].

The results of this study show that the application of a criterion consistent with the transient nature of the process makes it possible to predict (even in the simplest classical approximation) certain experimentally observed effects which are intractable within the framework of models relying on the conventional strength and yield criteria. The new characteristic quantity—namely, latent time—introduced into the model provides a basis for a unified treatment of such outwardly different processes as spall fracture and erosional fracture. Most importantly, this unification makes it possible to develop experimental methods based on erosional fracture for determining the time-dependent strength and yield, i.e., for examining dynamic strength characteristics of solids.

REFERENCES

1. Yu. V. Petrov, Dokl. Akad. Nauk **321**, 66 (1991) [Sov. Phys.-Dokl. **36**, 802 (1991)].
2. Y. V. Petrov and N. F. Morozov, ASME J. Appl. Mech. **61,** 710 (1994).
3. *Erosion*, Ed. by K. Pris (Academic, New York, 1979; Mir, Moscow, 1982).
4. E. M. Morozov and Yu. V. Kolesnikov, *The Mechanics of Contact Destruction* (Nauka, Moscow, 1989).
5. B. R. Lawn and T. R. Wilshaw, J. Mater. Sci. **10** (6), 1049 (1975).
6. S. C. Hunter, J. Mech. Phys. Solids **5** (3), 162 (1957).
7. L. I. Urbanovich, E. M. Kramchenkov, and Yu. N. Chunosov, Trenie Iznos **13**, 1052 (1992).
8. Yu. V. Polezhaev, *Thermogasodynamic Tests of Aircrafts* (Mosk. Aviatsionnyĭ Inst., Moscow, 1986).
9. N. F. Morozov and Yu. V. Petrov, *Problems of Dynamic Fracture of Solids* (Sankt-Peterb. Gos. Univ., St. Petersburg, 1997).
10. M. A. Meyers, *Dynamic Behavior of Materials* (Wiley, New York, 1994).

Translated by A. Betev

Doklady Physics, Vol. 47, No. 7, 2002, pp. 528–530. Translated from Doklady Akademii Nauk, Vol. 385, No. 2, 2002, pp. 186–188.

MECHANICS

Ultimate Forms for Models Describing Fragmentation of Meteoric Bodies

N. G. Barri and V. P. Stulov

Presented by Academician V.V. Rumyantsev February 18, 2002

Received February 19, 2002

The problem of the disintegration of small celestial bodies on entry into the planetary atmosphere is far from its solution. On the one hand, disintegration of meteoroids is directly observed [1] and is confirmed by the discovery of meteoric fields on the Earth's surface [2, 3]. On the other hand, the first attempts to discover the occurrence of fragmentation by analyzing the retardation rate on a luminous segment of the meteoroid's trajectory showed that either the fragmentation is entirely absent or affects the variation in the meteoroid velocity extremely weakly [4]. In many cases, in order to establish the fact of disintegration according to the bolide-luminescence intensity, more adequate luminescence models than those present at the moment in the literature are required.

Recently, several models describing the fragmentation of meteoroids under the action of an aerodynamic load were proposed. These models are based both on general physical concepts of fracturing inhomogeneous bodies under the action of forces applied to them and on certain assumptions simplifying the description of the disintegration process. We list only some of these models. The model proposed in [5] is based on the suggestion that the number of fragments produced is proportional to the dynamic component of the momentum flux $\rho_a V^2$ for the incoming gas. Physical properties of the model of instantaneous disintegration were formulated for the first time in [6]. Later, this model was employed in numerical calculations carried out in [7]. Finally, the model developed in [8] takes into account the dependence of the fragmentation process on the primary-body size. This model assumes that with a load increasing to its maximal value, each fragment is split in two.

In the cited papers, the models proposed were used for numerically calculating trajectories of meteor-swarm fragments. Furthermore, analytical solutions for trajectories, which allow for a decrease in the total mass of the fragments due to ablation [9–11], were obtained after slight simplifications. In the present study, we offer ultimate forms of solutions corresponding to large values of the mass-ablation parameter.

The important role of mass loss by a meteoroid penetrating the atmosphere is confirmed by both theoretical results and direct observations. The theoretical data are rather numerous; therefore, we here restrict our analysis to only monograph [12]. As far as direct observations are concerned, we first briefly describe the world experience in bolide-network operation. Meteorite patrols and then bolide networks were organized in Europe, the United States, and Canada in the second half of the last century. The goal was to take pictures of luminous segments of bolide trajectories. Afterwards, the meteorites were sought in locations on the Earth's surface extrapolated from their trajectories. Thousands of observations and photographic records of luminous trajectories had been performed. However, these efforts resulted in the discovery of only four fragments of meteoritic bodies. Even taking into account all the difficulties of this search, we must acknowledge the large role of total mass dispersion of solid fragments on their trajectories in the atmosphere.

Below, we propose simple formulas useful both for qualitative estimates and for comparison with observational data.

The study of the sequence of physical processes along the trajectory of a meteoritic body shows that in the case of sufficiently large objects, as a rule, the disintegration of a meteoroid occurs first, and only then does the ablation and retardation of formed fragments take place. Therefore, in all the models, it is assumed that at the disintegration point, the values of the velocity and mass of a meteoroid are equal to their values at the moment of their entry into the atmosphere. Thus, as for the case of the motion of a unified body [12], the ballistic factor α and the mass-ablation parameter β are basic dimensionless defining parameters. The additional parameter is the dimensionless altitude of disintegration y_0. In all cases, this altitude is defined as the altitude when the aerodynamic load for a body reaches its maximum.

The main difficulty in using the above analytical solutions in various decomposition models is the fact that elliptic integrals depending on the parameter β are

Institute of Mechanics, Moscow State University, Michurinskiĭ pr. 101, Moscow, 117463 Russia

1028-3358/02/4707-0528$22.00

present in the solutions. Therefore, we can expect substantial simplifications in the limit $\beta \gg 1$.

In the case of the instantaneous-disintegration model [6], the solution for a change in the body's velocity takes the form [10]

$$m = \exp[-\beta(1-\nu^2)], \tag{1}$$

$$\frac{2\alpha}{r_m}\left[\frac{t-t_0}{4}a^{3/2} + \left(\frac{t_0}{3} - \frac{1}{12r_m}\right)(a^{3/2}-1)\right]$$

$$= \varphi(y, y_0, \alpha, r_m) = \frac{1}{2}e^{-\beta}\Delta(\beta, \nu), \tag{2}$$

$$\Delta = \overline{\mathrm{Ei}}(\beta) - \overline{\mathrm{Ei}}(\beta\nu^2), \quad \overline{\mathrm{Ei}}(x) = \int_{-\infty}^{x}\frac{e^t}{t}dt,$$

$$a = [1 + r_m(t-t_0)]^2, \quad t = \exp\left(-\frac{y}{2}\right).$$

The defining parameters are

$$\alpha = \frac{1}{2}c_\mathrm{d}\frac{\rho_0 h_0 A_e}{M_e \sin\gamma}, \quad \beta = \frac{1}{2}\frac{c_\mathrm{h}V_e^2}{c_\mathrm{d}H^*},$$

$$y_0 = \ln\frac{\rho_0 V_e^2}{\sigma_*}, \quad r_m = \frac{2^{3/2}}{\sin\gamma}\left(\frac{\rho_0}{\rho_m}\right)^{1/2}\frac{h_0}{R_0}, \tag{3}$$

where σ_* and ρ_m are the strength and the density of the body's material, respectively. Here, the angle γ of the trajectory, the coefficients c_d and c_h of damping and heat exchange, respectively, and the evaporation enthalpy H^* are constant quantities. The values of the velocity V, of the body's mass M, and of the midsection area A at the entry of the body into the atmosphere are taken as the corresponding scales and are denoted by the subscript e. The altitude of the homogeneous atmosphere h_0 is taken as the altitude scale h, and the density ρ_0 corresponding to the altitude $h = h_0$ is chosen as the density scale for ρ_a. Thus, $\nu = \frac{V}{V_e}$, $m = \frac{M}{M_e}$, $a = \frac{A}{A_e}$, $y = \frac{h}{h_0}$, $\rho = \frac{\rho_a}{\rho_0}$.

Using the well known representation for the integral exponential function $\overline{\mathrm{Ei}}(x)$ at large values of the argument x [13], we arrive at the following ultimate form of solution (1), (2) as $\beta \gg 1$:

$$\nu = 1, \quad m = 1 - 2\beta\varphi(y, y_0, \alpha, r_m). \tag{4}$$

Here, it is sufficient to allow for only the first term in the representation of $\overline{\mathrm{Ei}}(x)$ at $x \gg 1$. Note that in the ultimate solution, the mass m depends on the product of the defining parameters α and β.

For the model of the subsequent slow fragmentation [5], the solution for the change in the body's velocity along the trajectory has the form [9] [the body's mass changes in accordance with formula (1)]:

$$\frac{\alpha}{2}e^{\frac{y_0}{3}}\left(e^{-\frac{4}{3}y} - e^{-\frac{4}{3}y_0}\right) = \psi(y, y_0, \alpha) = \frac{1}{3}\tilde{\beta}^{1/3}e^{-\tilde{\beta}}\tilde{\Delta},$$

$$\tilde{\beta} = \frac{\beta}{3}, \quad \tilde{\Delta} = \int_{\tilde{\beta}\nu^2}^{\tilde{\beta}}\frac{e^t}{t^{4/3}}dt. \tag{5}$$

The parameters α, β, and y_0 have the previous meaning (see [3]). Here, in the representation of the integral $\tilde{\Delta}$ for $\beta \gg 1$, we must use the asymptotic expression of the incomplete gamma function [14] with allowance for the first expansion term. After some straightforward calculation, we obtain the following ultimate form of solution (1), (5) for $\beta \gg 1$:

$$\nu = 1, \quad m^{1/3} = 1 - \beta\psi(y, y_0, \alpha). \tag{6}$$

Here, the product $\alpha\beta$ also serves as a defining parameter for the variation in the body's mass.

Finally, for the model of rapid sequential fragmentation [8], the dependence of the body's velocity on the altitude along the trajectory has the form that corresponds to [11] [as before, the mass of the body changes in accordance with solution (1)]:

$$2^{7/3}\frac{\alpha}{3}e^{2y_0}(e^{-3y} - e^{-3y_0}) = \chi(y, y_0, \alpha)$$

$$= -(\beta+1) + \frac{\exp[-\beta(1-\nu^2)]}{\nu^4}(\beta\nu^2 + 1) + \beta^2 e^{-\beta}\Delta. \tag{7}$$

The quantity Δ is written out in the same form as in (2). For the asymptotic representation of the right-hand side of formula (7), we again take the expression $\overline{\mathrm{Ei}}(x)$ for $\beta \gg 1$ [13]. The correct result is obtained when the first three expansion terms are taken into account Finally, we find the following ultimate form of solution (1), (7) for $\beta \gg 1$:

$$\nu = 1, \quad m = 1 - \frac{\beta}{2}\chi(y, y_0, \alpha). \tag{8}$$

Comparing formulas (6) and (8), we see that the designations of slow and rapid fragmentation introduced above are easy to justify.

It is worth noting that all three ultimate solutions (4), (6), and (8) describe the ablation of the meteoroid body in the absence of retardation. The same solutions are obtained under the assumption $V = V_e$ in the original differential equations.

Without doubt, similar expressions can be found if we ignore the constraint concerning the consideration of sufficiently large meteoroids for which $\nu = 1$, $m = 1$ at $y = y_0$, i.e., at the point of the onset of disintegration. In the case, the corrected solutions of type (4), (6) and (8) are simply extensions to the domain $y < y_0$ of the

corresponding solutions for a unified body, which exist for $y > y_0$ [12].

ACKNOWLEDGMENTS

The work was supported by the Russian Foundation for Basic Research, project no. 99-01-00385.

REFERENCES

1. P. Spurný, Planet. Space Sci. **42** (2), 157 (1994).
2. *Sikhoté-Alinskiĭ Iron Meteoritic Rain*, V. G. Fesenkov and E. L. Krinov, Eds. (Akad. Nauk SSSR, Moscow, 1959), Vol. 1.
3. A. K. Terent'eva and S. I. Barabanov, in *Circumterrestrial Astronomy of XXI Century* (GEOS, Moscow, 2001), pp. 307–311.
4. V. P. Stulov, Astron. Vestn. **34**, 545 (2000).
5. B. Baldwin and Y. Sheaffer, J. Geophys. Res. **76**, 4653 (1971).
6. S. S. Grigoryan, Kosm. Issled. **17**, 875 (1979).
7. J. G. Hills and P. Goda, Astron. J. **105**, 1114 (1993).
8. A. G. Ivanov and V. A. Ryzhanskiĭ, Dokl. Akad. Nauk **353**, 334 (1997) [Phys.–Dokl. **42**, 139 (1997)].
9. V. P. Stulov, Astron. Vestn. **32**, 455 (1998).
10. V. P. Stulov and P. V. Stulov, Astron. Vestn. **33**, 45 (1999).
11. V. P. Stulov and L. Yu. Titova, Dokl. Akad. Nauk **376**, 53 (2001) [Dokl. Phys. **46**, 50 (2001)].
12. V. P. Stulov, V. N. Mirskiĭ, and A. I. Vislyĭ, *Aerodynamics of Bolides* (Nauka, Moscow, 1995).
13. E. Yahnke, F. Emde, and F. Losch, *Tables of Higher Functions* (McGrow-Hill, New York, 1960; Nauka, Moscow, 1964).
14. *Handbook of Mathematical Functions*, Ed. by M. Abramowitz and I. A. Stegun (Dover, New York, 1965; Nauka, Moscow, 1979).

Translated by G. Merzon

Doklady Physics, Vol. 47, No. 7, 2002, pp. 531–534. Translated from Doklady Akademii Nauk, Vol. 385, No. 2, 2002, pp. 189–192.

MECHANICS

A Stochastic Model of the Motion of the Deformable-Earth Pole

Yu. G. Markov* and I. N. Sinitsyn**

Presented by Academician V.V. Kozlov March 13, 2002

Received March 1, 2002

1. The basis of many astrometric investigations is the dynamic theory of the rotation of the Earth relative to its center of mass. The investigation of rotation around the center of mass is hampered by the difficulty of constructing a dynamic model of the deformable Earth. At present, the development of mathematical models that describe the motion of the of observations and measurements of the International Earth Rotation Service (IERS) are not only of scientific value but also of practical interest [1–4].

According to the IERS data for the last 15–20 years, the Chandler vibration (free nutation), which has an amplitude of 0.20"–0.25" and a period of 433 ± 2 sidereal days, is separated in the complex motion [3]. The characteristics of the Chandler component are related to the inertia tensor of the deformable Earth [4]. Along with the Chandler component in the pole motion, it is possible to separate the annual vibration, which has an amplitude of ~0.07"–0.08" and a period of one year (365 sidereal days). According to [4, 5], the annual vibrations of Earth's axis are induced by solar gravitational torque, the orbital motion of the rotating Earth, and diurnal mantle tides. Estimates of the gravitational torque speak to the reality of such a mechanism for the excitation of vibrations. The causes and mechanism of the excitation of annual vibrations are unknown. It is conventional to attribute them to seasonal geophysical phenomena (to processes in Earth's atmosphere and to oceanic tides) [1, 2]. A refined model developed for the Chandler vibration of the pole on the basis of a viscoelastic model of the deformable Earth at the time interval of ~10 years was described in [5].

The trend of axis the of Earth's figure (~0.5" in the direction of 90° westwards from Greenwich), which, in our opinion, is associated with the centrifugal moments of inertia of the deformable Earth, is of fundamental importance for constructing a mathematical model of the pole motion at large time intervals (~50 years and longer). Changes in the trend can be induced by geotectonic processes with time constants on the order of 10^3 years and by the influence of a dynamic asymmetry leading to the modulation of Chandler vibrations with a period of ~220 years.

Let us develop a combined celestial-mechanical stochastic model on the basis of the IERS data [3] and of analytical considerations. The determinate component of the model represents the principal regular dynamic effects; the stochastic component, irregular effects following statistical regularities [6, 7].

2. Generalizing the results from [5], we proceed from the following three-dimensional nonlinear differential set with random parameters:

$$\dot{p} + N_* q = 3V_1 b\omega_*^2 \cos\omega_* t - V_4 r^2 + P(t, p, q, r, \mathbf{V}), \quad p(t_0) = p_0, \tag{1}$$

$$\dot{q} - N_* p = -3V_2 b\omega_*^2 \cos\omega_* t + V_5 r^2 + Q(t, p, q, r, \mathbf{V}), \quad q(t_0) = q_0, \tag{2}$$

$$\dot{r} = -3V_3\omega_*^2(b' + b''\cos 2\omega_* t) + R(t, p, q, r, \mathbf{V}), \quad r(t_0) = r_0, \tag{3}$$

where

$$\begin{aligned} P &= P(t, p, q, r, \mathbf{V}) = -3V_2V_6d_1b\omega_*^2\cos\omega_* t \\ &\quad - 3V_3V_5d_1\omega_*^2(b' + b''\cos 2\omega_* t) + \Delta P, \\ Q &= Q(t, p, q, r, \mathbf{V}) = -3V_1V_6d_2b\omega_*^2\cos\omega_* t \\ &\quad - 3V_3V_4d_2\omega_*^2(b' + b''\cos 2\omega_* t) + \Delta Q, \\ R &= R(t, p, q, r, \mathbf{V}) = -3V_1V_2d_3b\omega_*^2\cos\omega_* t \\ &\quad + 3V_1V_5d_3b\omega_*^2\cos\omega_* t + \Delta R. \end{aligned} \tag{4}$$

Here, p, q, and r are the components of terrestrial angular velocity; V_1, V_2, and V_3 are the random parameters

*Moscow Institute of Aviation, Volokolamskoe sh. 4, Moscow, 125080 Russia

**Institute of Information Science Problems, Russian Academy of Sciences, ul. Vavilova 30/6, Moscow, 117900 Russia

1028-3358/02/4707-0531$22.00

derived by time-averaging over the diurnal interval $T_* = \frac{2\pi}{r_*}$:

$$V_1 = V_1(t) = \frac{1}{T_*}\int_t^{t+T_*} \frac{\tilde{C}(\tau) - \tilde{B}(\tau)}{A^*}\cos r_*\tau d\tau,$$

$$V_2 = V_2(t) = \frac{1}{T_*}\int_t^{t+T_*} \frac{\tilde{C}(\tau) - \tilde{A}(\tau)}{B^*}\sin r_*\tau d\tau, \quad (5)$$

$$V_3 = V_3(t) = \frac{1}{T_*}\int_t^{t+T_*} \frac{\tilde{B}(\tau) - \tilde{A}(\tau)}{C^*}\sin 2r_*\tau d\tau,$$

which characterize the effective solar diurnal tidal humps; V_4, V_5, and V_6 are the random parameters

$$V_4 = V_4(t) = \frac{J^*_{qr}}{A^*} + \frac{1}{T_*}\int_t^{t+T_*} \frac{\tilde{J}_{qr}(\tau)}{A^*}d\tau,$$

$$V_5 = V_5(t) = \frac{J^*_{qr}}{B^*} + \frac{1}{T_*}\int_t^{t+T_*} \frac{\tilde{J}_{pr}(\tau)}{B^*}d\tau, \quad (6)$$

$$V_6 = V_6(t) = \frac{J^*_{pq}}{C^*} + \frac{1}{T_*}\int_t^{t+T_*} \frac{\tilde{J}_{pq}(\tau)}{C^*}d\tau,$$

which determine the effective tidal protrusions. Here, $A^* + \tilde{A}(t), B^* + \tilde{B}(t), C^* + \tilde{C}(t)$ and $J^*_{pq} + \tilde{J}_{pq}(t)$, $J^*_{qr} + \tilde{J}_{qr}(t)$, and $J^*_{rp} + \tilde{J}_{rp}(t)$ are the axial and centrifugal moments of inertia of the Earth, respectively, where the constant components are marked by an asterisk, and the variable components induced by the solar diurnal tides, by the tilde. We introduce the following notation for the random initial conditions:

$$V_7 = p_0, \quad V_8 = q_0, \quad V_9 = r_0.$$

The remaining quantities in Eqs. (1)–(4) are

$$N_* = (C^* - B^*)A^{*-1}\omega_*, \quad r_* = 365\omega_*,$$
$$2b' = \left(1 - \frac{b^2}{2}\right), \quad 2b'' = -b^2, \quad (7)$$
$$d_1 = \frac{B^*C^*}{A^*}, \quad d_2 = \frac{A^*C^*}{B^*}, \quad d_3 = \frac{A^*B^*}{C^*}.$$

Here, ω_* is the constant determined by the gravitational and focal parameters and b is the known coefficient [5].

The set of equations (1)–(3) was derived under the following assumptions. Lunar gravitational torques are ignored, because their effect on the vibrations is relatively small. The lunar influence leads to a monthly vibration whose amplitude is lower than that of the annual vibration by a factor of 15–20. In addition, we took into account the fact that the terms involving r, r^2, ω_*, and ω_*^2 substantially exceed the corresponding terms with squared and combined quantities p, q, $\frac{\dot{C}}{C^*}$, $\frac{\dot{J}_{pr}}{A^*}$, $\frac{\dot{J}_{rq}}{B^*}$, etc. The quantities ΔP, ΔQ, and ΔR are the terms of higher orders.

3. Using Eqs. (1)–(3), where the parameters V_i are real normal (Gaussian) random values with the mathematical expectations m_i^V, variances D_i^V, and covariances K_{ij}^V, $i, j = 1, 2, \ldots, 9$, and the method of stochastic expansion in random parameters [7], we obtain the following expansions of the expectations, variances, covariances, and covariance functions of the variables $p_t = p(t)$, $q_t = q(t)$, $r_t = r(t)$ for the moments of time t, $t' > t$:

$$m_t^{p,q,r} = \sum_{i=1}^{9} \psi_{i,t}^{p,q,r} m_i^V + \Delta m_t^{p,q,r}, \quad (8)$$

$$D_t^{p,q,r} = \sum_{i=1}^{9}\sum_{j=1}^{9} \psi_{i,t}^{p,q,r}\psi_{j,t}^{p,q,r} K_{ij}^V + \Delta D_t^{p,q,r}, \quad (9)$$

$$K_{t,t'}^{p,q,r} = \sum_{i=1}^{9}\sum_{j=1}^{9} \psi_{i,t}^{p,q,r}\psi_{j,t'}^{p,q,r} + \Delta K_{t,t'}^{p,q,r}, \quad (10)$$

$$K_{t,t'}^{pq} = \sum_{i=1}^{9}\sum_{j=1}^{9} \psi_{i,t}^{p}\psi_{j,t'}^{q} K_{ij}^V + \Delta K_{t,t'}^{pq},$$
$$K_{t,t'}^{qr} = \sum_{i=1}^{9}\sum_{j=1}^{9} \psi_{i,t}^{q}\psi_{j,t'}^{r} K_{ij}^V + \Delta K_{t,t'}^{qr}, \quad (11)$$
$$K_{t,t'}^{rp} = \sum_{i=1}^{9}\sum_{j=1}^{9} \psi_{i,t}^{r}\psi_{j,t'}^{p} K_{ij}^V + \Delta K_{t,t'}^{rp}.$$

Here, $\psi_{i,t}^{p,q,r}$ with $i = 1, 2, \ldots, 9$ are the influence functions of parameters V_i obtained by solving Eqs. (1)–(3) for $P = Q = R = 0$ and by replacing p, q, and r by $\psi_{i,t}^{p,q,r}$, respectively. The functions $\Delta m_t^{p,q,r}$, $\Delta D_t^{p,q,r}$, $K_{t,t}^{p,q,r}$, $\Delta K_{t,t'}^{pq}$, $\Delta K_{t,t'}^{qr}$, and $\Delta K_{t,t'}^{pr}$ are the components of the expectations, variances, and covariances that take into account the nonlinear functions P, Q, and R.

4. For zero initial conditions when nonlinear (in V_i) functions (4) can be neglected and r can be replaced by r_0 in the functions $V_{4,5}r^2$, the substitutions

$$\begin{gathered} i, j = 1, 2, \ldots, 5, \quad t = t_0, \\ \psi^p_{1,t} = b_0\omega_*^2 \sin\omega_* t = -\psi^q_{2,t}, \\ \psi^q_{1,t} = -b_0 N_* \cos\omega_* t = \psi^p_{2,t}, \\ \psi^r_{3,t} = -3b'\omega_*^2 t - \frac{3}{2}b''\omega_* \sin 2\omega_* t, \\ \psi^q_{4,t} = \psi^p_{5,t} = -r_0^2 N_*^{-1}, \\ b_0 = 3b\omega_*^2(\omega_*^2 - N_*^2)^{-1} \end{gathered} \tag{12}$$

must be made in Eqs. (8)–(11). In this case, the average statistical trends in p_t and q_t, the variances, and the covariances are constant at $t = t'$ and equal to

$$\langle m_t^p \rangle = -r_0^2 N_*^{-1} m_5^V, \quad \langle m_t^q \rangle = -r_0^2 N_*^{-1} m_4^V, \tag{13}$$

$$\langle D_t^p \rangle = \frac{1}{2}b_0^2(\omega_*^2 D_1^V + N_*^2 D_2^V) + (r_0^2 N_*^{-1})^2 D_5^V,$$

$$\langle D_t^q \rangle = \frac{1}{2}b_0^2(N_*^2 D_1^V + \omega_*^2 D_2^V) + (r_0^2 N_*^{-1})^2 D_4^V, \tag{14}$$

$$\langle K_{tt}^{pq} \rangle = \langle K_{tt}^{qr} \rangle = \langle K_{tt}^{rq} \rangle = 0,$$

where $\langle\cdot\rangle$ indicates averaging over time $2\pi\omega_*^{-1}$.

In the nonlinear approximation, the mean statistical trend in the variables p_t and q_t, which is averaged over the years $2\pi\omega_*^{-1}$, is determined by the following formulas:

$$\begin{aligned} \langle m_t^p \rangle = -\frac{1}{N_*}\Big[& m_5^V r_0^2 + 9\omega_*^4\left(b'^2 t^2 + \frac{b''^2}{8}\right) \\ & \times (m_5^V m_3^{V2} + m_5^V D_3^V + 2m_3^V K_{35}^V) \\ & - 6b'\omega_*^2 r_0 t(m_5^V m_3^V + K_{35}^V) \\ & - 3d_1 b'\omega_*^2(m_3^V m_5^V + K_{35})\Big], \end{aligned} \tag{15}$$

$$\begin{aligned} \langle m_t^q \rangle = -\frac{1}{N_*}\Big[& m_4^V r_0^2 + 9\omega_*^4\left(b'^2 t^2 + \frac{b''^2}{8}\right) \\ & \times (m_4^V m_3^{V2} + m_4^V D_3^V + 2m_3^V K_{34}^V) \\ & - 6b'\omega_*^2 r_0 t(m_4^V m_3^V + K_{34}^V) \\ & - 3d_2 b'\omega_*^2(m_4^V m_3^V + K_{34})\Big]. \end{aligned} \tag{16}$$

From Eqs. (15) and (16), the following conclusions can be made. The mean trend in the angular-velocity component p_t (q_t) is determined by the parameters V_3 and V_5 (V_3 and V_4) (i.e., the tidal hump in the second harmonic, the tidal protuberance, and their correlation).

Allowance for the quadratic (in V_i) terms makes it possible to derive refined analytical expressions for the influence functions, trends, variances, covariances, and covariance functions in model (8)–(11).

5. Stochastic model (8)–(11) is given in terms of statistical moments of the first and second orders and, therefore, is called the correlational stochastic model. The method of stochastic expansions also makes it possible to find the higher order statistical moments [7]. Therefore, it is possible to develop stochastic models including the moments of various orders. When a stochastic model is described in terms of one-dimensional and multidimensional distributions, more refined methods of the theory of nonlinear stochastic systems [6, 7] are used similar to [8].

6. The stochastic models of the deformable Earth make it possible to solve certain practical problems by using the methods of mathematical statistics [9], namely:

(i) To calculate the statistical characteristics of angular-velocity components p_t, q_t, and r_t at various moments of time (in particular, for the statistical prediction and detection of anomalous phenomena) from the known statistical characteristics of random parameters $\mathbf{V} = [V_1 \ldots V_9]^T$;

(ii) To estimate the mathematical expectations, variances, and covariances of parameters in Eqs. (1)–(3) and to determine the confidence intervals for them from known observation data [3];

(iii) To solve mixed problems where only certain variables and parameters are observable with an acceptable accuracy.

At the Institute of Problems of Information Science (RAS), a specialized software package was developed for solving the above problems on the basis of the stochastic differential model (1)–(3) and the methods of the normal and ellipsoidal approximation of distributions [6, 7].

The further increase in requirements regarding the accuracy and time of predictions requires, on the one hand, more elaborate inclusion of the errors in the measurements of the IERS angular velocity parameters, and, on the other hand, the inclusion of the nonlinear stochastic perturbations ΔP, ΔQ, and ΔR in Eqs. (1)–(3).

ACKNOWLEDGMENTS

This work was supported by the Russian Foundation for Basic Research, project nos. 01-02-17250 and 01-01-00758.

REFERENCES

1. W. Munk and G. Macdonald, *The Rotation of the Earth* (Cambridge Univ. Press, Cambridge, 1960; Mir, Moscow, 1964).
2. H. Moritz and A. Mueller, *Earth Rotation: Theory and Observation* (Ungar, New York, 1987; Naukova Dumka, Kiev, 1992).
3. IERS Annual Reports: 1990–2000 (Central Burea IERS, Observ. P., 2000).
4. L. D. Akulenko, S. A. Kumakshev, and Yu. G. Markov, Dokl. Akad. Nauk **379** (2), 191 (2001) [Dokl. Phys. **46**, 261 (2001)].
5. L. D. Akulenko, S. A. Kumakshev, and Yu. G. Markov, Dokl. Akad. Nauk **382** (2), 199 (2002) [Dokl. Phys. **47** (1), 78 (2002)].
6. V. S. Pugachev and I. N. Sinitsyn, *Stochastic Differential Systems: Analysis and Filtering* (Nauka, Moscow, 1990; Wiley, New York, 1987).
7. V. S. Pugachev and I. N. Sinitsyn, *The Theory of Stochastic Systems* (Logos, Moscow, 2000).
8. I. N. Sinitsyn, Dokl. Akad. Nauk **348** (3), 327 (1996) [Phys. Dokl. **41**, 218 (1996)].
9. V. S. Pugachev, *Probability Theory and Mathematical Statistics for Engineers* (Nauka, Moscow, 1979; Pergamon, Oxford, 1984).

Translated by V. Bukhanov

Doklady Physics, Vol. 47, No. 7, 2002, pp. 535–537. Translated from Doklady Akademii Nauk, Vol. 385, No. 2, 2002, pp. 193–195.

MECHANICS

On the Generalized Mindlin Problem

D. A. Pozharskiĭ

Presented by Academician F.L. Chernous'ko February 21, 2002

Received February 28, 2002

The classical Mindlin paper [1] published in 1936 consists of first and second sections concerning concentrated forces perpendicular and parallel to the boundary of the elastic half-space, respectively. In paper [2], the fundamental solutions obtained by Lord Kelvin and Mindlin (the first section of [1]) are generalized for the case of a three-dimensional elastic wedge where a concentrated force is perpendicular to its edge under different types of boundary conditions at its sides. Below, we present expressions for three Papkovich–Neuber harmonic functions for a wedge that has unstressed sides and where a concentrated force parallel to its edge acts in its middle half-plane. When the opening angle of the wedge corresponds to a half-space, the expressions for elastic displacements and stresses coincide with formulas from the second section of [1]. Displacements at the wedge edge are calculated as well. The solutions obtained by Boussinesq and Cherutti for an elastic wedge with one side subjected to normal and tangential loads and the other side free of stress are generalized in [3]. The problems of a three-dimensional wedge are solved by presenting a harmonic function as the complex Fourier–Kontorovich–Lebedev integral and by reducing the three-dimensional problem of elasticity theory to the Hilbert boundary value problem generalized in the sense of Vekua [4–6].

Using the cylindrical coordinates r, φ, z, we consider the three-dimensional elastic wedge ($0 \le r < \infty$, $|\varphi| \le \alpha$, $|z| < \infty$) with the opening angle 2α, the shear modulus G, and the Poisson's ratio ν. The z-axis of the right-handed coordinate system is directed along the wedge edge (Fig. 1). Let the wedge sides $\varphi = \pm\alpha$ be free of stress, and the concentrated force T parallel to the edge be applied at an arbitrary point $r = x$, $z = y$ and act in the bisecting half-plane $\varphi = 0$. Since the problem is symmetric in φ, we consider the wedge region $-\alpha \le \varphi \le 0$ with the boundary conditions

$$\varphi = -\alpha\colon\ \sigma_\varphi = \tau_{r\varphi} = \tau_{\varphi z} = 0; \qquad (1)$$

$$\varphi = 0\colon u_\varphi = \tau_{r\varphi} = 0, \quad \tau_{\varphi z} = \frac{1}{2}T\delta(r-x)\delta(z-y). \qquad (2)$$

In addition, stresses are assumed to decrease at infinity.

In the cylindrical coordinates, the general solution to the Navier equilibrium equations can be expressed in terms of three Papkovich–Neuber harmonic functions $\Phi_n = \Phi_n(r, \varphi, z)$, $n = 0, 1, 2$ by Eqs. (5)–(7) from [2]. Stresses are determined from these formulas by Hooke's law. Harmonic functions Φ_n are sought as complex Fourier integrals with respect to z and the complex Kontorovich–Lebedev integrals with respect to r. The familiar method [4–6] provides a solution to boundary value problem (1), (2) in the form of Eqs. (5)–(7) from [2], where, after passing to the real Fourier and Kontorovich–Lebedev integrals ($n = 0, 1, 2$),

$$\Phi_n(r, \varphi, z) = \frac{T}{\pi^3 G}\int_0^\infty\int_0^\infty \sinh(\pi\tau)[A_n(\tau, t)\cosh(\varphi\tau) + B_n(\tau, t)\sinh(\varphi\tau)]\mathcal{K}_{i\tau}(tr)\sin(t[z-y])t^{-1}d\tau\, dt, \qquad (3)$$

$$B_0(\tau, t) = \mathcal{K}_{i\tau}(tx) + \frac{x}{4(1-\nu)}\mathcal{K}'_{i\tau}(tx), \qquad (4)$$

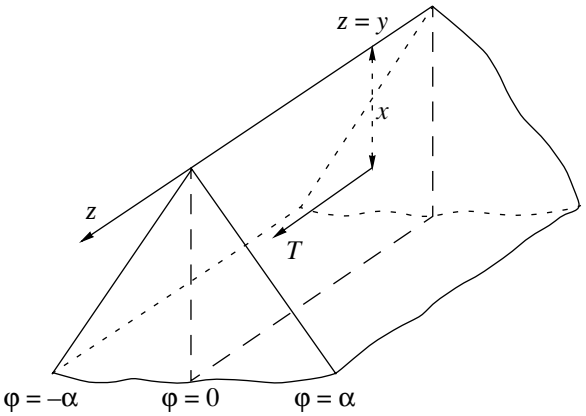

Fig. 1. Concentrated force inside a three-dimensional wedge.

Institute of Mechanics and Applied Mathematics, Rostov State University, pr. Stachki 200/1, Rostov-on-Don, 344090 Russia

1028-3358/02/4707-0535$22.00

$$A_1(\tau, t) = \frac{\tau}{x}\mathcal{K}_{i\tau}(tx),$$
$$B_2(\tau, t) = \mathcal{K}'_{i\tau}(tx) := \frac{\partial}{\partial x}\mathcal{K}_{i\tau}(tx). \quad (5)$$

Here, functions (4) and (5) are found from conditions (2) and are independent of α, $\mathcal{K}_{i\tau}(x)$ is the modified Bessel function, and the other integrands entering into (3) have the form

$$A_0(\tau, t) = \coth(\alpha\tau)\left[\mathcal{K}_{i\tau}(tx) + \frac{x}{4(1-\nu)}\mathcal{K}'_{i\tau}(tx)\right] - \frac{1-2\nu}{2t\sinh(\alpha\tau)}\int_0^\infty \frac{\Psi(s, t)\sinh(\pi s)}{\cosh(\pi s) + \cosh(\pi\tau)}ds, \quad (6)$$

$$B_1(\tau, t) = [\tau x^{-1}\sinh(2\alpha\tau)\mathcal{K}_{i\tau}(tx) + \sin(2\alpha)\mathcal{K}'_{i\tau}(tx) - 4(1-\nu)\sinh(\alpha\tau)\cos\alpha\Psi(\tau, t)]g_-^{-1}(\tau, \alpha), \quad (7)$$

$$A_2(\tau, t) = [\tau x^{-1}\sin(2\alpha)\mathcal{K}_{i\tau}(tx) + \sinh(2\alpha\tau)\mathcal{K}'_{i\tau}(tx) - 4(1-\nu)\cosh(\alpha\tau)\sin\alpha\Psi(\tau, t)]g_-^{-1}(\tau, \alpha), \quad (8)$$

$$\Psi(\tau, t) = \frac{1}{g_+(\tau, \alpha)}\left[\frac{g_-(\tau, \alpha)}{\cosh(\pi\tau/2)}\Phi(\tau, t) + \frac{\Psi_*(\tau, t)}{2(1-\nu)}\right], \quad (9)$$

$$\Psi_*(\tau, t) = \mathcal{K}_{i\tau}(tx)\cos\alpha\{\tau x^{-1}[\tau\cosh(\alpha\tau)\sin(2\alpha) + 2\sinh(\alpha\tau)(2(1-\nu) - \kappa\cos^2\alpha)] + 2t^2x\cosh(\alpha\tau)\tan\alpha\sin^2\alpha\} + \mathcal{K}'_{i\tau}(tx)\sin\alpha[\tau\sinh(\alpha\tau)\sin(2\alpha) - 2\cosh(\alpha\tau)(2(1-\nu) - \kappa\sin^2\alpha)] + g_-(\tau, \alpha)\int_0^\infty\{\mathcal{K}_{iu}(tx)\sin\alpha[2ux^{-1}\cosh(\alpha u) \times (1-2\nu-\kappa\cos^2\alpha) - (t^2x - u^2x^{-1})\sinh(\alpha u)\sin(2\alpha)] + \mathcal{K}'_{iu}(tx)\cos\alpha[2\sinh(\alpha u)(1-2\nu-\kappa\sin^2\alpha) - u\cosh(\alpha u)\sin(2\alpha)]\}\frac{g_-^{-1}(u, \alpha)\sinh(\pi u)du}{\cosh(\pi u) - \cosh(\pi\tau)}, \quad (10)$$

$$g_+(\tau, \alpha) = \sinh(2\alpha\tau) + \tau\sin(2\alpha), \quad (11)$$

$$g_-(\tau, \alpha) = \cosh(2\alpha\tau) - \cos(2\alpha), \quad \kappa = 3 - 4\nu. \quad (12)$$

At fixed t, the function $\Phi(\tau, t)$ satisfies the Fredholm integral equation of the second kind ($0 \le \tau < \infty$)

$$\Phi(\tau, t) = (1-2\nu)\int_0^\infty L(\tau, u)\times\left[\Phi(u, t) + \frac{\cosh(\pi u/2)}{g_-(u, \alpha)}\frac{\Psi_*(u, t)}{2(1-\nu)}\right]du - \frac{tx\cosh(\pi\tau/2)}{2(1-\nu)}\int_0^\infty \frac{\sinh(\pi u)\cosh(\alpha u)g(u, \alpha)G(u, t)}{\cosh(\pi u) + \cosh(\pi\tau)}du, \quad (13)$$

$$G(u, t) = 4(1-\nu)\mathcal{K}_{iu}(tx)x^{-1} + \mathcal{K}'_{iu}(tx). \quad (14)$$

The functions $L(\tau, u)$ and $g(u, \alpha)$ are determined by Eqs. (17) and (18) from [2].

Integrals (3) for functions (4)–(14) are convergent at all $\varphi \in [-\alpha, 0]$. At $n = 0$, the order of integration is important in Eq. (3): integration with respect to t must be taken at the end.

At $\alpha = \frac{\pi}{2}$, the solution to boundary value problem (1), (2) in the form of Eqs. (5)–(7) from [2] with Eqs. (3)–(14) coincides with the solution to the Mindlin problem for a half-space when a concentrated force is parallel to its boundary. Then, $\Phi(\tau, t) = 0$ and, using the integral

$$\int_0^\infty \frac{\cosh(\pi u/2)\mathcal{K}_{iu}(tx)}{\cosh(\pi u) + \cosh(\pi\tau)}du = \frac{t}{2\cosh(\pi\tau/2)}\int_x^\infty \mathcal{K}_{i\tau}(tx)dx,$$

one obtains

$$A_0(\tau, t) = \frac{(1-2\nu)^2t^2}{2(1-\nu)\sinh(\pi\tau)}\int_x^\infty\int_x^\infty \mathcal{K}_{i\tau}(tx)dx\,dx - \frac{(1-2\nu)t^2x}{2(1-\nu)\sinh(\pi\tau)}\int_x^\infty \mathcal{K}_{i\tau}(tx)dx + \coth\frac{\pi\tau}{2}\left[\mathcal{K}_{i\tau}(tx) + \frac{x}{4(1-\nu)}\mathcal{K}'_{i\tau}(tx)\right],$$

$$B_1^-(\tau, t) = \frac{\tau}{x}\tanh\frac{\pi\tau}{2}\mathcal{K}_{i\tau}(tx),$$

$$A_2(\tau, t) = \frac{2(1-2\nu)t^2}{\sinh(\pi\tau)}\int_x^\infty \mathcal{K}_{i\tau}(tx)dx - \frac{2t^2x}{\sinh(\pi\tau)}\mathcal{K}_{i\tau}(tx) + \tanh\frac{\pi\tau}{2}\mathcal{K}'_{i\tau}(tx).$$

Calculation of the integrals (see [7]) leads to the following expressions for the displacements $u_r(r, 0, z)$ and $u_z(r, 0, z)$:

$$u_r(r, 0, z) = \frac{T(z-y)}{16\pi(1-\nu)G}\left(\frac{r-x}{R_-^3} + \frac{\kappa(r-x)}{R_+^3} - \frac{6rx(r+x)}{R_+^5} + \frac{4(1-\nu)(1-2\nu)}{R_+(R_+ + r + x)}\right), \quad (15)$$

$$u_z(r, 0, z) = \frac{T}{16\pi(1-\nu)G}\left(\frac{4(1-\nu)}{R_-} + \frac{4(1-\nu)}{R_+} - \frac{(r-x)^2}{R_-^3} - \frac{\kappa(r+x)^2}{R_+^3} + \frac{2rx}{R_+^3} - \frac{6rx(z-y)^2}{R_+^5} + \frac{4(1-\nu)(1-2\nu)(r+x)}{R_+(R_+ + r + x)}\right), \quad (16)$$

$$R_\pm = [(r \pm x)^2 + (z-y)^2]^{1/2}.$$

Formulas (15) and (16) agree exactly with Eqs. $(18)_3$ and $(18)_1$ derived in [1], respectively. Unfortunately, similar formulas (9.29) presented in [8] contain misprints.

The inverse-operator theorem for a combination of the two special Neumann series [2, 6, 9] explains the occurrence of both Fredholm integral equation (13) and the similar equation (16) from [2]. At any angle α and, for $\nu > 0.053$, a solution to Fredholm equation (13) can be represented as the Neumann power series in $(1 - 2\nu)$, which is uniformly convergent in the Banach space $C_M(0, \infty)$ of functions that are continuous and bounded in the semiaxis [5, 6]. It is convenient to solve Eq. (13) by the collocation method.

The above formulas, together with the results of [2], can be used to solve the problems concerning a thin rigid inclusion into a three-dimensional wedge. The similar problem for space was considered in [10].

Mindlin (see Fig. 6 in [1]) calculated the displacement $u_r(0, 0, z)$ normal to the half-space boundary by Eq. (15) at $y = 0$ and $\nu = 0.3$ and found that maximum $|u_r(0, 0, z)|$ is reached at $z \approx 0.63x$. As an example, we investigate the absolute extrema of the displacements $u_r(0, 0, z)$ and $u_z(0, 0, z)$ for the wedge edge at $y = 0$ and $\nu = 0.5$. Figure 2 shows the dimensionless transverse displacement

$$u_r^*(0, 0, z^*) = -u_r(0, 0, z)4\pi GxT^{-1},$$

$$z^* = zx^{-1}$$

for the wedge covering the three quarters, one half, and one quarter of space. One can see that the maximum point u_r^* shifts to the right with decreasing wedge angle.

With the use of the relation $\mathcal{H}_{iu}(0) = \pi\delta(u)$, where $\delta(u)$ is the Dirac function, and of Eq. (6.671.14) from [7], we obtain the longitudinal displacement at the edge:

$$u_z(0, 0, z) = \frac{T}{8G\alpha}\left(\frac{1}{R} + \frac{z^2}{R^3}\right), \quad R = (x^2 + z^2)^{1/2}.$$

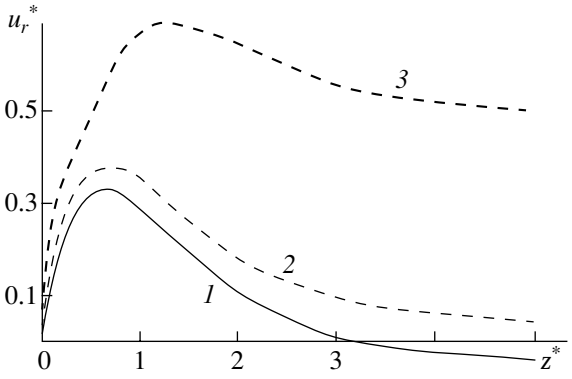

Fig. 2. Transverse displacement at the wedge edge for $\alpha =$ (*1*) $\frac{3\pi}{4}$, (*2*) $\frac{\pi}{2}$, and (*3*) $\frac{\pi}{4}$. Curve *2* has the maximum at $z^* = \frac{\sqrt{2}}{2}$.

According to this expression, the absolute maximum at any angle α is

$$\max u_z(0, 0, z) = \frac{\sqrt{6}T}{18Gx\alpha} \text{ at } z = \frac{\sqrt{2}}{2}x.$$

ACKNOWLEDGMENTS

This work was supported by the Alexander von Humboldt Foundation, Germany.

REFERENCES

1. R. D. Mindlin, Physics (N. Y.) **7,** 195 (1936).
2. D. A. Pozharskiĭ, Dokl. Akad. Nauk **380** (4), 487 (2001) [Dokl. Phys. **46**, 722 (2001)].
3. D. A. Pozharskiĭ, Dokl. Akad. Nauk **372** (3), 333 (2000) [Dokl. Phys. **45**, 236 (2000)].
4. A. F. Ulitko, *The Method of Vector Eigenfunctions in 3D Problems of Elasticity Theory* (Naukova Dumka, Kiev, 1979).
5. U. A. Lubyagin, D. A. Pozharskiĭ, and M. I. Chebakov, Dokl. Akad. Nauk SSSR **321** (1), 58 (1991) [Sov. Phys. Dokl. **36**, 797 (1991)].
6. V. M. Alexandrov and D. A. Pozharskii, *Three-Dimensional Contact Problems* (Kluwer, Dordrecht, 2001).
7. I. S. Gradshteyn and I. M. Ryzhik, *Tables of Integrals, Series, and Products* (Nauka, Moscow, 1971; Academic, New York, 1980).
8. H. G. Hahn, *Elastizitatstheorie* (Teubner, Stuttgart, 1985).
9. D. A. Pozharskiĭ, Izv. Akad. Nauk, Mekh. Tverd. Tela **28** (6), 105 (1993).
10. V. M. Alexandrov, B. I. Smetanin, and B. V. Sobol', *Thin Concentrators of Stresses in Elastic Bodies* (Nauka, Moscow, 1993).

Translated by Yu. Verevochkin

Doklady Physics, Vol. 47, No. 7, 2002, pp. 538–539. Translated from Doklady Akademii Nauk, Vol. 385, No. 3, 2002, pp. 332–333.

MECHANICS

Vibration-Strength Viruses in Elastic Solids: The Half-Space Case

Academician V. A. Babeshko, V. V. Buzhan, and R. Williams[1]

Received January 21, 2002

We consider an elastic half-space with a system of flat rigid inclusions oriented parallel to each other. Such a system of inclusions was defined in [2, 3] as one of the varieties of the so-called vibration-strength "virus." Being a major cause of the onset of brittle fracture, these viruses most often develop in tectonic-plate fracture zones as well as in irregularly strengthened structural elements. For this reason, recently begun studies of the conditions for the localization of wave processes in elastic solids by this type of defect irregularities are topical.

General systems of relevant integral equations were investigated in [2, 3] in order to clarify the conditions for wave-process localization by a virus. In [4], the fundamental concepts of previous studies were confirmed for the case of an unbounded elastic medium, and the basic approach to solving the problem was formulated. In the present paper, the previously started studies are extended to the half-space case.

1. We consider an elastic half-space in the rectangular coordinate system (x_1, x_2, x_3) with L horizontal irregularities which reside in cross sections $x_3 = h_l$, $l = 1, 2, \ldots, L$ and occupy the corresponding domains Ω_l. Displacements $\mathbf{u}_l \exp\{-i\omega t\}$ act on the boundaries of the inclusions. Stresses $\boldsymbol{\tau}_{L+1} \exp\{-i\omega t\}$ act on the day surface $x_3 = h_{L+1}$ in the domain Ω. We denote the stresses at the inclusion boundaries by $\boldsymbol{\tau}_l^{\pm}$. According to the definition taken from [2], the structure under discussion is a mixed virus of the (1, 2) class and of the $(L + 1)$th level. It is written out in the form $V(1/h_l; \Omega_l/\ldots/h_L; \Omega_L // 2/h_{L+1}; \infty)$.

The following integral relations were obtained in [3] for the layer $-\infty \le x_1, x_2 \le +\infty$, $h_{l-1} \le x_3 \le h_l$:

$$\begin{aligned} D_{l-1}^{+}\mathbf{T}_{l-1}^{+} - D_l^{+}\mathbf{T}_l^{-} &= L_{l-1}^{+}\mathbf{U}_{l-1}^{+} - L_l^{+}\mathbf{U}_l^{-}, \\ D_{l-1}^{-}\mathbf{T}_{l-1}^{+} - D_l^{-}\mathbf{T}_l^{-} &= L_{l-1}^{-}\mathbf{U}_{l-1}^{+} - L_l^{-}\mathbf{U}_l^{-}, \end{aligned} \tag{1}$$

$$\mathbf{U}_l^{\pm}(\alpha_1, \alpha_2, x_3) = \int_{-\infty}^{\infty}\int \mathbf{u}_l^{\pm}(x_1, x_2, x_3) e^{i(\alpha_1 x_1 + \alpha_2 x_2)} dx_1 dx_2,$$

$$\mathbf{T}_l^{\pm}(\alpha_1, \alpha_2, x_3) = \int_{-\infty}^{\infty}\int \boldsymbol{\tau}_l^{\pm}(x_1, x_2, x_3) e^{i(\alpha_1 x_1 + \alpha_2 x_2)} dx_1 dx_2.$$

Here, $\mathbf{u}_l^{\pm}$ are displacements at the layer boundaries.

In order to obtain integral equations, we eliminate all terms containing $e^{\pm i\alpha_{3j}h_0}$ and $e^{i\alpha_{3j}h_1}$ from relation (1) $\left(\alpha_{31} = \sqrt{\varepsilon^2 - \alpha^2}, \alpha_{32} = \sqrt{1 - \alpha^2}, \varepsilon = \dfrac{c_t}{c_l}; c_l \text{ and } c_t \text{ are the velocities of the longitudinal and transverse waves in the medium, respectively, and } \alpha^2 = \alpha_1^2 + \alpha_2^2\right)$. We set

$$\mathbf{U}_l = \mathbf{U}_l^{-} = \mathbf{U}_l^{+}, \quad l = 1, 2, \ldots, L;$$

$$\mathbf{T}_{L+1} = \mathbf{T}_{L+1}^{-} = \mathbf{T}_{L+1}^{+}.$$

As a result, we arrive at the following system of integral relations:

$$\begin{aligned} D_1^{-}\mathbf{T}_1^{-} &= L_1^{-}\mathbf{U}_1, \\ D_1^{+}\mathbf{T}_1^{+} - D_2^{+}\mathbf{T}_2^{-} &= L_1^{+}\mathbf{U}_1 - L_2^{+}\mathbf{U}_2, \\ D_1^{-}\mathbf{T}_1^{+} - D_2^{-}\mathbf{T}_2^{-} &= L_1^{-}\mathbf{U}_1 - L_2^{-}\mathbf{U}_2, \\ &\ldots \\ D_L^{+}\mathbf{T}_L^{+} - D_{L+1}^{+}\mathbf{T}_{L+1}^{-} &= L_L^{+}\mathbf{U}_L - L_{L+1}^{+}\mathbf{U}_{L+1}, \\ D_L^{-}\mathbf{T}_L^{+} - D_{L+1}^{-}\mathbf{T}_{L+1} &= L_L^{-}\mathbf{U}_L - L_{L+1}^{-}\mathbf{U}_{L+1}. \end{aligned} \tag{2}$$

Here, $\mathbf{U}_{L+1}$ are displacements at the surface of the half-space $x_3 = h_{L+1}$.

Solving set (2) by the elimination method results in the system of integral equations

$$M_L\mathbf{G} = \mathbf{F}, \tag{3}$$

$$\mathbf{G} = \{\mathbf{U}_1, \mathbf{U}_2, \ldots, \mathbf{U}_L, \mathbf{T}_{L+1}\}^T,$$

[1] Collaborator from the United States.

Kuban State University,
ul. Karla Libknekhta 9, Krasnodar, 350640 Russia

1028-3358/02/4707-0538$22.00

$$\mathbf{F} = \{\mathbf{T}_1, \mathbf{T}_2, \ldots, \mathbf{T}_L, \mathbf{U}_{L+1}\}^T,$$
$$M_L = P_L K_L, \qquad (4)$$
$$P_L = \operatorname{diag}\{S_1^{-1}, S_1^{-1}, \ldots, S_1^{-1}\},$$

$$K_L = \begin{bmatrix} I & J_{12}^+ & J_{13}^+ & \ldots & J_{1L}^+ & J_{1,L+1}^+ \\ J_{12}^- & I & J_{23}^+ & \ldots & J_{2L}^+ & J_{2,L+1}^+ \\ J_{13}^- & J_{23}^- & I & \ldots & J_{2L}^+ & J_{3,L+1}^+ \\ \ldots & \ldots & \ldots & \ldots & \ldots & \ldots \\ J_{1,L}^- & J_{2,L}^- & J_{3,L}^- & \ldots & I & J_{L,L+1}^+ \\ 0 & 0 & 0 & \ldots & 0 & -I \end{bmatrix}$$

$$\times \begin{bmatrix} I & 0 & 0 & \ldots & 0 & 0 \\ 0 & I & 0 & \ldots & 0 & 0 \\ 0 & 0 & I & \ldots & 0 & 0 \\ \ldots & \ldots & \ldots & \ldots & \ldots & \ldots \\ 0 & 0 & 0 & \ldots & I & A_{L,L+1}^+ \\ -J_{1,L+1}^- & -J_{2,L+1}^- & -J_{3,L+1}^- & \ldots & -J_{L,L+1}^- & -R_- \end{bmatrix}.$$

Here, $\mathbf{T}_l = \mathbf{T}_l^+ - \mathbf{T}_l^-$ is the stress jump at the boundary of the lth inclusion, I is the unit matrix, $A_{kl}^+ = D_+^{-1} P_{kl} L_-$, and $R_- = D_-^{-1} L_-$. The representations for the matrix $J_{kl}^{\pm}$, S_1, P_{kl}, $D_\pm$, and $L_\pm$ are given in [4].

2. The technique for solving both system (3) and the corresponding system for the space of [4] is based on the knowledge of real-valued singularities for elements of the system-symbol matrix-valued function and zeros of its determinant.

From (4), we have

$$\det M_L = \det P_L \det K_L. \qquad (5)$$

It is also shown in [4] that determinants of matrices similar to P_L have no real zeros, and their singularities are branch points of radicals α_{31} and α_{32}.

According to the block-matrix theory, the determinant of the first matrix in the expansion of K_L coincides with the determinant of the matrix obtained by deleting the last row and the last column. The matrix in question belongs to the system of integral equations for the spatial case of [4]. The determinant of the second matrix can be obtained by consecutive expansion from the first to the $(L-1)$th row and accounts for the contribution of the day surface $x_3 = h_{L+1}$ in expression (5).

Thus, the results of the investigations for the root subsets of the system-symbol matrix determinant presented in [4] have found their extension to the half-space case. In particular, the presence of the exponential functions $\exp\{i\alpha_{3k}(h_{p+1} - h_p)\}$ can cause a high-frequency oscillation of the determinant function in the segment [0, 1] with an increase in the remoteness of neighboring inclusions. This effect may be responsible for the appearance of regular real zeros. The appearance of a single zero u_0 in the interval $(1, +\infty)$ is explained by the absence of the oscillation. An increase in the remoteness of the inclusion nearest to the day surface leads to the problem for a homogeneous half-space, which explains the tendency of u_0 toward a root of the Rayleigh characteristic equation for $h_{L+1} - h_L \longrightarrow \infty$ (see figure).

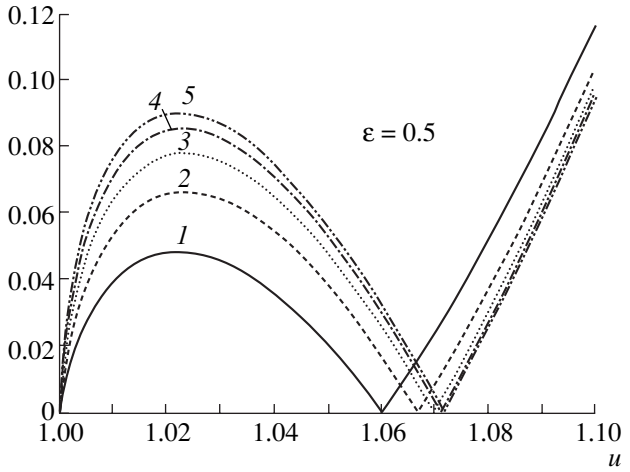

Modulus M of the function $\det K_L$. $h_{L+1} - h_L = 6$ (*1*), 7 (*2*), 8 (*3*), 9 (*4*), 10 (*5*).

ACKNOWLEDGMENTS

This work was supported by the Russian Foundation for Basic Research, project nos. 99-01-00787 and r2000Yug (00-01-96024, 00-01-96019); by the Ministry of Education of the Russian Federation, project no. E00-4.0-145; by the CRDF, project no. REC-004; and by the Integratsiya program, project no. A0017.

REFERENCES

1. V. M. Aleksandrov, B. I. Smetanin, and B. V. Sobol', *Thin Concentrations of Stresses in Elastic Bodies* (Nauka, Moscow, 1993).
2. V. A. Babeshko, Izv. Ross. Akad. Nauk, Mekh. Tverd. Tela, No. 3, 5 (2000).
3. V. A. Babeshko, Izv. Vyssh. Uchebn. Zaved. Sev.-Kavk. Reg. Estestv. Nauki, No. 3, 1 (2000).
4. V. A. Babeshko, V. V. Buzhan, A. V. Pavlova, and S. V. Ratner, Izv. Vyssh. Uchebn. Zaved. Sev.-Kavk. Reg. Estestv. Nauki, Spetsvypusk, p. 26 (2001).

Translated by V. Tsarev

Doklady Physics, Vol. 47, No. 7, 2002, pp. 540–543. Translated from Doklady Akademii Nauk, Vol. 385, No. 3, 2002, pp. 334–337.

MECHANICS

Optimization of Shells Made of Quasi-brittle Materials under a Cyclic Load

N. V. Banichuk

Presented by Academician D.M. Klimov February 1, 2002

Received February 5, 2002

Problems concerning the design of minimum-weight axisymmetric shells made of quasi-brittle materials are considered. The optimization problem under investigation is to find the optimal thickness distributions for shells with allowance for the possibility of the origination and growth of cracks caused by cyclic actions on a shell. This problem is characterized by incomplete information on the initial dimensions, positions, and orientations of cracks. Here, formulation of the optimal design problem and its analytical solution are based on the guaranteed (minimax) approach. Earlier, this approach was used to optimize quasi-brittle bodies subjected to constant loads [1, 2].

An equilibrium stressed state of a membrane shell of revolution that is subjected to axisymmetric loads q_n and q_ϕ is described by the relations [3]

$$\frac{N_\phi}{r_1} + \frac{N_\theta}{r_2} = -q_n, \tag{1}$$

$$2\pi r_0 N_\phi \sin\phi + R = 0, \tag{2}$$

$$\sigma_\phi = \frac{N_\phi(\phi)}{h(\phi)}, \quad \sigma_\theta = \frac{N_\theta(\phi)}{h(\phi)}. \tag{3}$$

Here, q_n and q_ϕ are the intensities of external actions that are normal to the median surface and tangential to the meridian, respectively (Fig. 1). Position of the meridian is determined by the angle θ measured from a certain fixed meridian plane, and the position of the parallel circle is given by the angle ϕ between the normal to the median surface and the axis of revolution. The meridional plane and the plane normal to the meridian are the planes of the principal curvatures at the point under consideration. The corresponding radii of curvature are denoted by r_1 and r_2, and the radius of the parallel circle is designated as r_0. In addition, N_ϕ and N_θ are the normal forces of the membrane (per unit length), σ_ϕ and σ_θ are the corresponding stresses, and h is the shell thickness. The quantity R is the resultant external action on the shell part situated above the parallel circle determined by the angle ϕ. At given $h(\phi)$, $q_n(\phi)$, $q_\phi(\phi)$, $R(\phi)$, $r_1(\phi)$, $r_2(\phi)$, and $r_0(\phi)$ ($r_0 = r_2 \sin\phi$), the forces N_ϕ and N_θ are found from Eqs. (2) and (1), respectively, and the stresses are calculated by Eq. (3).

Hereafter, the thickness h is assumed to be small compared to the radii of curvature of the shell [3, 4]:

$$h_m = \max_\phi h(\phi) \ll r_m, \tag{4}$$

$$r_m = \min\{\min_\phi r_1(\phi), \min_\phi r_2(\phi)\}, \tag{5}$$

where the exterior minimum in (5) denotes the minimum of the two quantities written in braces.

It is assumed that the shell is made of quasi-brittle material and contains an initial through crack of length $l = l_0$. The crack is considered to be rectilinear and is assumed to be much longer than the shell thickness but

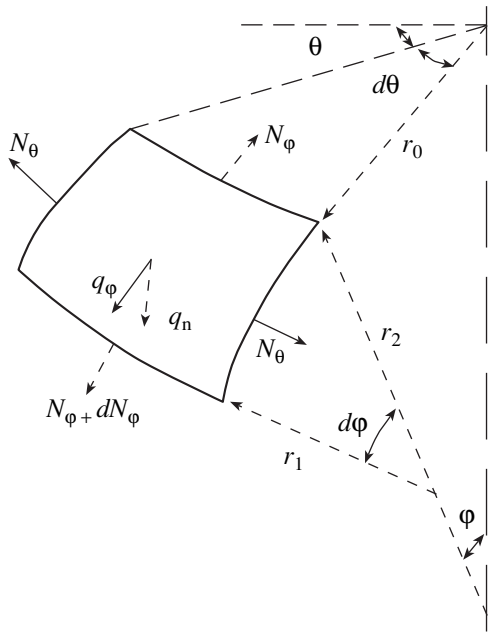

Fig. 1.

Institute for Problems of Mechanics,
Russian Academy of Sciences,
pr. Vernadskogo 101, Moscow, 117526 Russia

1028-3358/02/4707-0540$22.00

much shorter than the characteristic dimension r_m ($h_m \ll l \ll r_m$). The position of the initial crack is not fixed on the shell beforehand. The cyclic loads applied to the shell,

$$q_\phi = q_\phi^0 p, \quad q_n = q_n^0 p, \tag{6}$$

$$0 \le p_{min} \le p \le p_{max}, \tag{7}$$

cause both the quasistatic variation of the stressed state of the shell and a monotonic increase in crack length. Here, q_ϕ^0 and q_n^0 are the given amplitude functions of the independent coordinate ϕ, p is the load parameter, and p_{min} and p_{max} are given constants. For cyclic loads, the fatigue growth of the crack is described by the equation [5, 6]

$$\frac{dl}{dn} = C(\Delta K_1)^m, \quad l_0 \le l \le l_{cr}, \quad 0 \le n \le n_{cr}. \tag{8}$$

Here, n is the number of cycles; C and m ($2 < m \le 4$) are the given material constants; K_1 is the stress-intensity factor for an opening-mode crack determined by the formula

$$K_1 = \sigma_n \sqrt{\frac{\pi l}{2}}, \tag{9}$$

where σ_n is the normal stress in the uncracked shell at the point where the crack is expected in the damaged shell, and the increment ΔK_1 in Eq. (8) is defined as

$$\Delta K_1 = (K_1)_{max} - (K_1)_{min} = \sqrt{\frac{\pi l}{2}} \sigma_n^0 (p_{max} - p_{min}), \tag{10}$$

where $(K_1)_{max}$ and $(K_1)_{min}$ are the maximum and minimum of the stress-intensity factor in the cycle and σ_n^0 and σ are calculated as

$$\sigma_n^0 = (\sigma_n)_{p=1}, \quad \sigma = p_{max}\sigma_n^0. \tag{11}$$

With allowance for Eq. (10), differential equation (8) determines the crack length l as a function of the number of cycles n when crack growth is quasistatic. It is valid until the moment when crack propagation becomes unstable (the shell fails) at $n = n_{cr}$; i.e., $l = l_{cr}$. The following fracture criterion is used to find l_{cr}:

$$K_1(l_{cr}, \sigma) = K_{1\epsilon}. \tag{12}$$

Here, $K_{1\epsilon} = K_{1c} - \epsilon$, where $\epsilon > 0$ is a sufficiently small number and K_{1c} is the brittle strength constant of the material. Relations (9), (11), and (12) yield

$$l_{cr} = \frac{2}{\pi}\left(\frac{K_{1\epsilon}}{\sigma}\right)^2 = \frac{2}{\pi}\left(\frac{K_{1\epsilon}}{p_{max}\sigma_n^0}\right)^2. \tag{13}$$

Initial crack length l_0 is assumed to be less than the critical value l_{cr}, i.e., $l_0 \le l_{cr}$. The service life of the construction is determined by the number of load cycles n_{cr} after which the crack length attains the critical value l_{cr}. Therefore, the design of a shell with demand on the service life requires the inclusion of the condition

$$n_{cr} \ge n_*, \tag{14}$$

where n_* is the given minimum number of cycles to failure.

Below, we consider the problem of optimal shell design. It takes into account that both the stress-intensity factor K_1 and the number of cycles to failure n_{cr} depend implicitly (through the quantity σ) on shell thickness and parameters determining crack position. The desired optimal distribution of shell thickness $h = h(\phi)$ must satisfy the geometric restriction $h \ge h_0$ ($h_0 > 0$ is given) and inequality (14) for all permissible positions and lengths of cracks and must minimize the functional $J(h)$ (volume of shell material)

$$J = J(h) \longrightarrow \min_h,$$
$$J(h) = \int_0^{2\pi}\int_{\phi_0}^{\phi_f} hr_1 r_2 \sin\phi \, d\phi \, d\theta = 2\pi \int_{\phi_0}^{\phi_f} hr_1 r_2 \sin\phi \, d\phi, \tag{15}$$

where ϕ_0 and ϕ_f ($\phi_0 < \phi_f$) are the given parameters determining the range of the angle ϕ. As was noted above, the initial crack position, orientation, and length are unknown beforehand. For this reason, the calculation of n_{cr} is complicated, because various admissible positions and orientations of initial cracks must be analyzed. In this case, the rigorous formulation of the problem requires certain additional assumptions about permitted positions and lengths of the crack. The initial crack is characterized by the vector $\omega = \{\phi_c, l_0, \alpha\}$, where ϕ_c is the coordinate of the crack middle, l_0 is the crack length, and the angle α assigns crack orientation with respect to the shell meridian. The second coordinate of the crack middle θ_c is insignificant, because the problem under consideration is axisymmetric and the guaranteed approach used allows any crack position in parallels ($0 \le \theta_c \le 2\pi$). If $\alpha = 0$, the crack is oriented in the meridional direction (axial crack); if $\alpha = \frac{\pi}{2}$, the crack is oriented in the direction of parallels (peripheral crack). It is assumed that the initial crack lengths l_0 are less than the given limiting value l_m, where $l_0 \le l_m \ll r_m$. The above assumptions and available additional data on the shell regions where the appearance of cracks is most probable make it possible to consider the set of permitted cracks $\Lambda(\omega \in \Lambda)$ as being given.

Thus, the problem of optimal design is to find the thickness distribution $h(\phi)$ that minimizes functional (15) with allowance for the geometric restriction

$$h(\phi) \ge h_0 \tag{16}$$

and the following restriction on the number of cycles to failure:

$$\min_{\omega} n_{cr} \geq n_*, \tag{17}$$

where the minimum with respect to ω is found over the set Λ:

$$\omega \in \Lambda. \tag{18}$$

The quantity n_{cr} in Eq. (17) depends on σ. To find its explicit form, we integrate Eq. (8) between the limits $0 \leq n \leq n_{cr}$, $l_0 \leq l \leq l_{cr}$ and use Eq. (13) for l_{cr}. As a result, we find

$$n_{cr} = \frac{\psi_1(\sigma)}{\psi_2(\sigma)}, \quad \psi_1(\sigma) = 1 - \left(\frac{l_0\pi}{2}\left(\frac{\sigma}{K_{1\epsilon}}\right)^2\right)^{\frac{m}{2}-1},$$
$$\psi_2(\sigma) = \left(\frac{m}{2}-1\right) l_0^{\frac{m}{2}-1} C\left(\frac{\pi}{2}\right)^{\frac{m}{2}} \sigma^m \left(1 - \frac{p_{min}}{p_{max}}\right)^m. \tag{19}$$

According to Eq. (19), the critical number of cycles n_{cr} is a monotonically decreasing function of the quantities σ and l_0. Consequently, it attains a minimum when $l_0 = l_m$ and σ takes one of the two extreme values

$$\sigma = (\sigma)_{\alpha=0} = \sigma_\theta, \quad \sigma = (\sigma)_{\alpha=\frac{\pi}{2}} = \sigma_\phi, \tag{20}$$

which correspond to the axial ($\alpha = 0$) and peripheral $\left(\alpha = \frac{\pi}{2}\right)$ cracks.

Let $\sigma_* > 0$ be a root of the algebraic equation

$$n_{cr}(\sigma) = n_*. \tag{21}$$

Then, service life restriction (17) turns into the following system of two inequalities:

$$\max_{\phi_c}\left(\sigma_\phi = \frac{N_\phi}{h}\right) \leq \sigma_*, \quad \max_{\phi_c}\left(\sigma_\theta = \frac{N_\theta}{h}\right) \leq \sigma_*,$$
$$N_\phi = -\frac{R}{2\pi r_0 \sin\phi_c}, \quad N_\theta = r_2\left(\frac{R}{2\pi r_0 r_1 \sin\phi_c} - q_n\right), \tag{22}$$

where the intensities of external loads and the force R determined by them are taken at $p = p_{max}$.

The system of inequalities (22) is satisfied if and only if

$$h(\phi) \geq -\frac{R(\phi)}{2\pi\sigma_* r_0(\phi)\sin\phi},$$
$$h(\phi) \geq \frac{r_2(\phi)}{\sigma_*}\left(\frac{R(\phi)}{2\pi r_0(\phi) r_1(\phi)\sin\phi} - q_n(\phi)\right) \tag{23}$$

for $\phi \in [\phi_0, \phi_f]$. In this case, the solution of problem (15)–(18), which is reduced to the minimization of integral (15) with restrictions (16), (23), has the form

$$h = \max\left\{h_0, \frac{N_\phi}{\sigma_*}, \frac{N_\theta}{\sigma_*}\right\}$$
$$= \max\left\{h_0, -\frac{R}{2\pi\sigma_* r_0 \sin\phi}, \frac{r_2}{\sigma_*}\left(\frac{R}{2\pi r_0 r_1 \sin\phi} - q_n\right)\right\}. \tag{24}$$

At any fixed $\phi \in [\phi_0, \phi_f]$, max in (24) means the maximum of the three quantities in braces. At $m = 4$, which is typical of metals [7], we have

$$n_{cr} = \frac{1 - \frac{\pi l_m}{2}\left(\frac{\sigma}{K_{1\epsilon}}\right)^2}{C\left(\frac{\pi}{2}\right)^2 l_m \sigma^4 \left(1 - \frac{p_{min}}{p_{max}}\right)^4}, \tag{25}$$

and the condition $n_{cr}(\sigma) \geq n*$ takes the following form of the explicit restriction on σ:

$$\sigma^2 \leq \sigma_*^2 \equiv b_1(-1 + \sqrt{1 + b_2}),$$
$$b_1 = \frac{1}{C\pi\left(1 - \frac{p_{min}}{p_{max}}\right)^4 K_{1\epsilon}^2 n^*},$$
$$b_2 = 4n_* C K_{1\epsilon}^4 \frac{1}{l_m}\left(1 - \frac{p_{min}}{p_{max}}\right)^4. \tag{26}$$

At sufficiently large values of n_{cr}, i.e., in the case of high-cycle fatigue, the quantity σ_* has the asymptotic representation

$$\sigma_* = \left[\sqrt{\frac{\pi}{2}}(C l_m n_*)^{1/4}\left(1 - \frac{p_{min}}{p_{max}}\right)\right]^{-1}. \tag{27}$$

The example below represents the problem of optimal design for a torus shell obtained by revolving a circle of radius a around a vertical axis at distance b from the circle center. Half the vertical shell section is shown in Fig. 2. The shell is subjected to uniform internal pressure $q_n = pq^0$ ($q^0 = \text{const}$), which cycles proportionally to the parameter p. The arising forces N_ϕ and N_θ are found by considering the equilibrium of a ring-shaped shell segment and are written as [3]

$$N_\phi = \frac{a}{2}\left(1 + \frac{b}{r_0}\right)q_n, \quad N_\theta = \frac{a}{2}q_n, \tag{28}$$

where $r_0 = b + a\sin\phi$. Taking the inequality $N_\phi > N_\theta$ into account and using Eq. (24), we arrive at the optimal thickness distribution in the shell:

$$h = \max\left\{h_0, \frac{N_\phi}{\sigma_*}\right\} = \max\left\{h_0, \frac{aq^0}{2\sigma_*}\left(1 + \frac{b}{r_0}\right)\right\}. \tag{29}$$

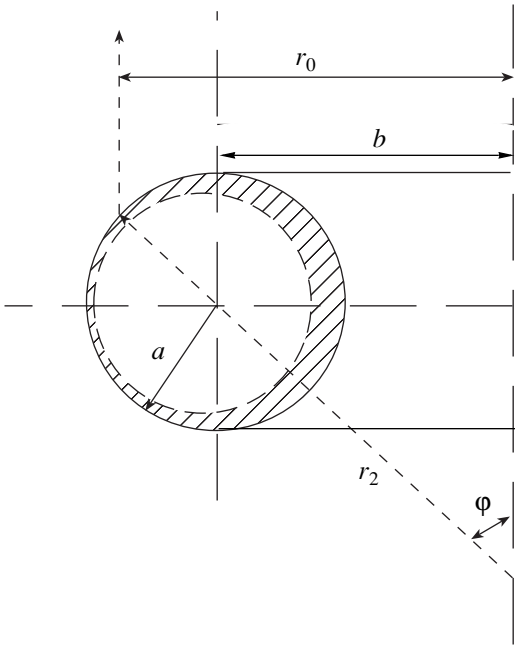

Fig. 2.

If $m = 4$ and n_{cr} values are so large that asymptotic representation (27) is valid, the optimal thickness distribution is written as the following explicit function of the determining parameters:

$$h = \max\left\{h_0, \frac{aq_0}{2}\left(1 + \frac{b}{r_0}\right)\right. \times \left.\sqrt{\frac{\pi}{2}}\,(Cl_m n_*)^{1/4}\left(1 - \frac{p_{min}}{p_{max}}\right)\right\}. \quad (30)$$

The optimal thickness distribution in the toroidal shell is shown in Fig. 2. Figure 2 and Eqs. (29) and (30) indicate that the shell thickness h decreases with increasing distance from the axis of revolution $r_0 = b + a\sin\phi$.

ACKNOWLEDGMENTS

This work was supported in part by the Russian Foundation for Basic Research, project no. 00-01-96025, and by the r2000-Yug Regional Program.

REFERENCES

1. N. V. Banichuk, Dokl. Akad. Nauk **358**, 40 (1998) [Dokl. Phys. **43**, 34 (1998)].
2. N. V. Banichuk, Mech. Struct. Mach. **26**, 365 (1998).
3. S. P. Timoshenko and S. Woinowsky-Krieger, *Theory of Plates and Shells*, 2nd ed. (McGraw-Hill, New York, 1959; Nauka, Moscow, 1966).
4. V. V. Novozhilov, K. F. Chernykh, and E. I. Mikhaĭlovskiĭ, *The Linear Theory of Thin Shells* (Politekhnika, Leningrad, 1991).
5. M. F. Kanninen and C. H. Popelar, *Advanced Fracture Mechanics* (Oxford Univ. Press, New York, 1985).
6. R. N. L. Smith, *Basic Fracture Mechanics: Including an Introduction to Fatigue* (Butterworth-Heinemann, Oxford, 1991).
7. K. R. E. Hellan, *Introduction to Fracture Mechanics* (McGraw-Hill, New York, 1984; Mir, Moscow, 1988).

Translated by Yu. Verevochkin

Doklady Physics, Vol. 47, No. 7, 2002, pp. 544–547. Translated from Doklady Akademii Nauk, Vol. 385, No. 3, 2002, pp. 338–341.

MECHANICS

A New Integral in the Problem of Rolling a Ball on an Arbitrary Ellipsoid

A. V. Borisov, I. S. Mamaev, and A. A. Kilin

Presented by Academician V. V. Kozlov February 19, 2002

Received March 4, 2002

1. EQUATIONS OF MOTION FOR A BALL ON A SURFACE

We consider equations of rolling without slip for a completely dynamically symmetric ball (with its central moment of inertia being $I = \mu E$) on an arbitrary surface. These equations can be derived from various general forms of the equations of nonholonomic mechanics. Here, we use conventional equations for the momentum and angular momentum.

In contrast to the conventional approach in the dynamics of rigid bodies, in which a coordinate system attached to a body is used, a fixed coordinate system is more convenient when considering equations of motion for a uniform ball. In this coordinate system, the equations for the momentum and angular momentum with respect to the ball's center of mass with allowance for the reaction and external forces take the form

$$m\dot{\mathbf{v}} = \mathbf{N} + \mathbf{F}, \quad (I\dot{\boldsymbol{\omega}}) = \mathbf{a} \times \mathbf{N} + \mathbf{M}_F \tag{1}$$

with the non-slip condition (i.e., the velocity of the point of contact is zero) given by the equality

$$\mathbf{v} + \boldsymbol{\omega} \cdot \mathbf{a} = 0. \tag{2}$$

Here, m is the ball's mass; $\mathbf{v}$ is the velocity of the center of mass; $\boldsymbol{\omega}$ is the angular velocity; $I = \mu E$ is the central inertia tensor; $\mathbf{a}$ is the radius vector directed from the point of contact to the center of mass; R is the ball radius; $\mathbf{N}$ is the reaction force at the point of contact; and $\mathbf{F}$ and $\mathbf{M}_F$ are the external force and the moment of forces with respect to this point (see Fig.1).

Excluding the reaction force $\mathbf{N}$ from these equations and imposing the kinematic condition that the velocity of the point of contact on the surface should be the same as that on the sphere, we arrive at a system of six equations for the angular momentum $\mathbf{M}$ and the vector $\boldsymbol{\gamma} = -R^{-1}\mathbf{a}$ normal to the surface:

$$\dot{\mathbf{M}} = D\dot{\boldsymbol{\gamma}} \times (\boldsymbol{\omega} \times \boldsymbol{\gamma}) + \mathbf{M}_F, \quad \dot{\mathbf{r}} + R\dot{\boldsymbol{\gamma}} = \boldsymbol{\omega} \times R\boldsymbol{\gamma}, \tag{3}$$

where $D = mR^2$. Here, the vectors $\boldsymbol{\omega}$ and $\mathbf{r}$ (radius vector of the point of contact) should be found from the equations

$$\mathbf{M} = \mu\boldsymbol{\omega} + D\boldsymbol{\gamma} \times (\boldsymbol{\omega} \times \boldsymbol{\gamma}), \quad \boldsymbol{\gamma} = \frac{\nabla F(\mathbf{r})}{|\nabla F(\mathbf{r})|}, \tag{4}$$

where $F(\mathbf{r}) = 0$ is the equation specifying the fixed surface on which the ball rolls (the latter equation in (4) is a Gauss map). Hereinafter, following E. Routh, we will explicitly specify the surface on which the center of mass of the sphere moves, with points on the surface given by the radius vector $\mathbf{r}' = \mathbf{r} + R\boldsymbol{\gamma}$. Thus, it is the center of mass (rather than the point of contact) that moves on an ellipsoid. This surface is equidistant with respect to the surface on which the point of contact moves.

In the case of potential forces, the moment of forces $\mathbf{M}_F$ is expressed in terms of the potential $U(\mathbf{r}') = U(\mathbf{r} + R\boldsymbol{\gamma})$, which depends on the center-of-mass position according to the formula $\mathbf{M}_F = R\boldsymbol{\gamma} \times \dfrac{\partial U}{\partial \mathbf{r}'}$.

Remark 1. *In Routh's monograph* [6], *the equations of motion for a sphere were derived with respect to semimovable axes and were explicitly solved in certain*

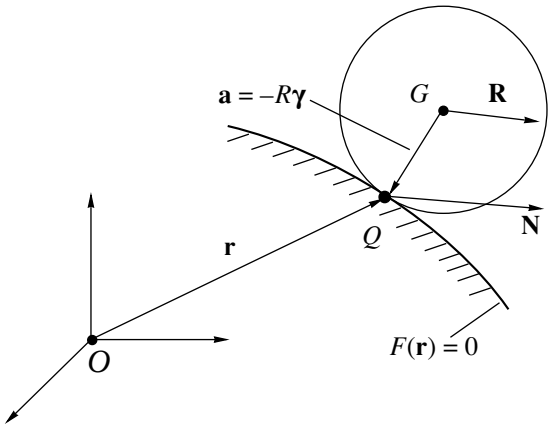

Fig. 1. Rolling of a sphere on a surface (G is the center of mass and Q is the point of contact of the ball with the surface).

Institute of Computer Research,
Universitetskaya ul. 1, Izhevsk, 426034 Russia

1028-3358/02/4707-0544$22.00

cases. Later, most authors of handbooks [1, 5] *only repeated Routh's results and actually appended nothing to them. It is worth noting that E. Routh paid special attention to the stability of particular solutions* (*e.g., a sphere rotating at the top of a surface of revolution*). *Here, we do not present the Routh equations in their original form, because Eqs.* (3) *are similar to the equations in* [3], *which describe an arbitrary body moving on either a plane or a sphere. This allows us to consider various problems* (*for example, the integrability of equations*) *from a unified standpoint.*

Integrals of motion. Equations (3) with a potential field $U(\mathbf{r} + R\boldsymbol{\gamma})$ have the energy integral and the geometric integral

$$H = \frac{1}{2}(\mathbf{M}, \boldsymbol{\omega}) + U(\mathbf{r} + R\boldsymbol{\gamma}), \quad F_1 = \boldsymbol{\gamma}^2 = 1. \quad (5)$$

In the case of an arbitrary surface $F(\mathbf{r}) = 0$, besides these two integrals, system (3) has neither the measure nor the two additional integrals that are necessary for the system to be integrable in accordance with the Euler–Jacobi theory. Generally speaking, the behavior of the system is chaotic. As will be argued below, in some cases, there may exist a measure and only one additional integral, with the chaotic behavior being less pronounced. As was pointed out by E. Routh, for the case of a surface of revolution, the system has two additional integrals and becomes integrable, while its behavior is regular. In this case, the system is reduced to a Hamiltonian system by an appropriate change of the time variable.

Rolling of a sphere on a quadric surface. We now derive the particular case of Eqs. (3) when the ball's center of mass moves on a quadric surface given by the equations

$$(\mathbf{r} + R\boldsymbol{\gamma}, B^{-1}(\mathbf{r} + R\boldsymbol{\gamma})) = 1, \quad B = \mathrm{diag}(b_1, b_2, b_3). \quad (6)$$

In the case of an ellipsoid, the quantities b_i are positive and determine the principal semiaxes squared. Using Eqs. (6), we express the radius vector $\mathbf{r}$ in terms of the normal $\boldsymbol{\gamma}$ to the surface:

$$\mathbf{r} + R\boldsymbol{\gamma} = \frac{B\boldsymbol{\gamma}}{\sqrt{(\boldsymbol{\gamma}, B\boldsymbol{\gamma})}}. \quad (7)$$

As a result, we arrive at the equations of motion in the variables $\mathbf{M}$ and $\boldsymbol{\gamma}$:

$$\dot{\mathbf{M}} = -\frac{D}{\mu + D}(\mathbf{M}, \dot{\boldsymbol{\gamma}})\boldsymbol{\gamma},$$
$$\dot{\boldsymbol{\gamma}} = \frac{R\sqrt{(\boldsymbol{\gamma}, B\boldsymbol{\gamma})}}{\mu + D}\boldsymbol{\gamma} \times (\boldsymbol{\gamma} \times B^{-1}(\boldsymbol{\gamma} \times \mathbf{M})). \quad (8)$$

2. MOTION OF A BALL ON AN ELLIPSOID OF REVOLUTION

First, we consider the rolling of a ball on an axisymmetric ellipsoid. The equation for a surface of revolution in the absolute coordinate system can be given in the form

$$r_1 = (f(\gamma_3) - R)\gamma_1, \quad r_2 = (f(\gamma_3) - R)\gamma_2,$$
$$r_3 = \int\left(f(\gamma_3) - \frac{1-\gamma_3^2}{\gamma_3}f'(\gamma_3)\right)d\gamma_3 - R\gamma_3, \quad (9)$$

where $f(\gamma_3)$ is a certain function determining the parametric form of the surface. Parameterization (9) is chosen such that the system presented below takes the simplest form.

In the case under consideration,

$$f(\gamma_3) = \frac{b_1}{\sqrt{b_1(1-\gamma_3^2) + b_3\gamma_3^2}}, \quad (10)$$

where b_1 and b_3 are the ellipsoid principal semiaxes squared. Equations of motion (3) admit an invariant measure with the density

$$\rho = (b_1(1-\gamma_3^2) + b_3\gamma_3^2)^{-3}. \quad (11)$$

In what follows, we consider a reduced form of the system and introduce the new variables

$$N_1 = (\mathbf{M}, \boldsymbol{\gamma}), \quad N_2 = \frac{\mu}{\mu + D}f(\gamma_3)(\gamma_3(\mathbf{M}, \boldsymbol{\gamma}) - M_3),$$
$$K_3 = \frac{M_1\gamma_2 - M_2\gamma_1}{\sqrt{1-\gamma_3}}. \quad (12)$$

These variables satisfy the equations

$$\dot{N}_1 = -kK_3\frac{f'}{\gamma_3 f^2}N_2, \quad \dot{N}_2 = kK_3\nu^2 f N_1, \quad \dot{\gamma}_3 = kK_3,$$
$$\dot{K}_3 = -k\frac{g}{\nu^4\gamma_3(1-\gamma_3^2)^2 f^3}N_2(\nu^2 f(1-\gamma_3^2)N_1 + \gamma_3 N_2), \quad (13)$$

where

$$k = \frac{R\sqrt{1-\gamma_3^2}}{(\mu + D)g}, \quad g = f - \frac{1-\gamma_3^2}{\gamma_3}f', \quad \nu^2 = \frac{\mu}{\mu + D}.$$

Using Eq. (10), we arrive at two linear equations in the independent variable γ_3:

$$\frac{dN_1}{d\gamma_3} = -\frac{b_1 - b_3}{b_1\sqrt{b_1(1-\gamma_3^2) + b_3\gamma_3^2}}N_2,$$
$$\frac{dN_2}{d\gamma_3} = \frac{\nu^2 b_1}{\sqrt{b_1(1-\gamma_3^2) + b_3\gamma_3^2}}N_1. \quad (14)$$

It is easy to prove that Eqs. (14) have the quadratic integral of motion with constant coefficients

$$F_2 = b_1^2\nu^2 N_1^2 + (b_1 - b_3)N_2^2. \quad (15)$$

This integral can be generalized to the case of a triaxial ellipsoid.

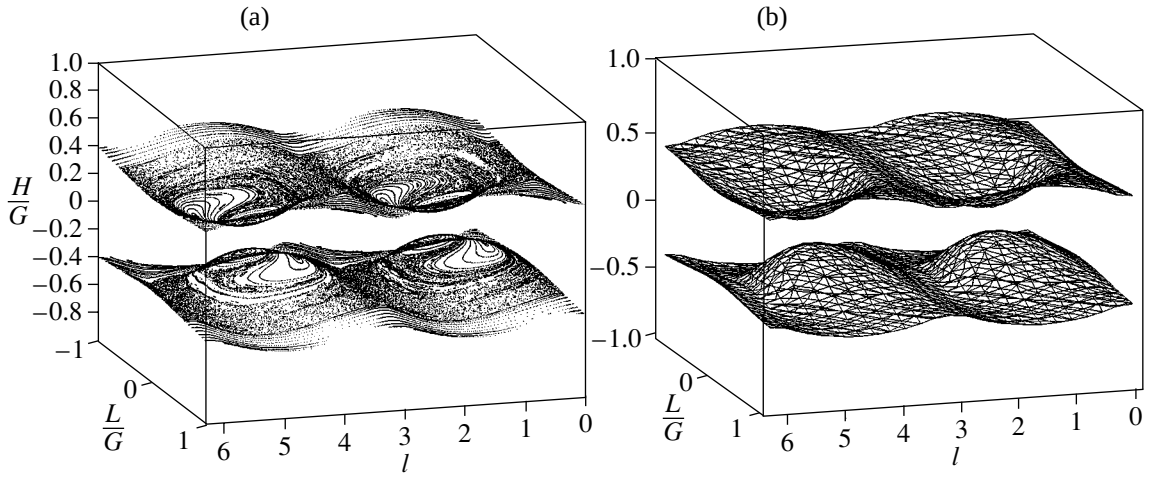

Fig. 2. (a) Three-dimensional map and (b) the surface F_2 corresponding to the level of the integral for $E = 1$, $B = \mathrm{diag}(1, 4, 9)$, and $F_2 = 1.7$.

System (14) is solvable in terms of elementary functions. Its solution, being dependent on the sign of the difference $b_1 - b_3$, takes the form

$$\text{(i) } b_1 > b_3,\ a^2 = \frac{b_1}{b_1 - b_3} > 1,$$

$$\begin{aligned} N_1 &= c_1 \sin\varphi(\gamma_3) + c_2 \cos\varphi(\gamma_3), \\ N_2 &= a\nu\sqrt{b_1}(-c_1 \cos\varphi(\gamma_3) + c_2 \sin\varphi(\gamma_3)), \\ \varphi(\gamma_3) &= \nu \arctan\frac{\gamma_3}{\sqrt{a^2 - \gamma_3^2}}; \end{aligned} \tag{16}$$

$$\text{(ii) } b_1 < b_3,\ a^2 = \frac{b_1}{b_3 - b_1} > 0,$$

$$\begin{aligned} N_1 &= c_1\tau^{-\nu} + c_2\tau^{\nu}, \quad N_2 = a\nu\sqrt{b_1}(-c_1\tau^{-\nu} + c_2\tau^{\nu}), \\ \tau(\gamma_3) &= \gamma_3 + \sqrt{a^2 + \gamma_3^2}. \end{aligned} \tag{17}$$

Here, c_1 and c_2 are constants defining linear integrals of motion.

Remark 2. *It is interesting that neither Routh nor his followers succeeded in finding the simplest reduced equations* [*similar to Eqs.* (14)] *and in solving the problem of a ball rolling on an ellipsoid of revolution in terms of elementary functions. The success of the explicit integration presented above is due to the appropriate choice of reduced variables* (12).

3. ROLLING OF A BALL ON AN ARBITRARY ELLIPSOID

We now consider in more detail the dynamics of a sphere whose center of mass moves on the quadric surface

$$(\mathbf{r} + R\boldsymbol{\gamma}, B^{-1}(\mathbf{r} + R\boldsymbol{\gamma})) = 1, \quad B = \mathrm{diag}(b_1, b_2, b_3). \tag{18}$$

In this case, equations of motion take the form of Eqs. (8), and we arrive at the Jacobi nonholonomic problem. This name stems from the fact that, as the moments of inertia of the ball tend to zero ($\mu \longrightarrow 0$; i.e., the entire ball's mass is localized at the center of mass), the problem under consideration is reduced to an ordinary holonomic problem of geodetic lines on an ellipsoid. The problem was solved by Jacobi in terms of the elliptic functions. In the case of an arbitrary surface, such a limiting transformation also leads to the problem of geodetic lines on the surface on which the center of mass moves. In the cases of other limiting transformations, it is impossible to exclude an additional degree of freedom, which arises due to rotation of the ball about a normal to the surface.

Equations (8) with an arbitrary (nondegenerate) matrix B have an invariant measure and a quadratic integral of motion:

$$\rho = (\boldsymbol{\gamma}, B\boldsymbol{\gamma})^{-2}, \quad F_2 = \frac{(\boldsymbol{\gamma} \times \mathbf{M}, B^{-1}(\boldsymbol{\gamma} \times \mathbf{M}))}{(\boldsymbol{\gamma}, B\boldsymbol{\gamma})}. \tag{19}$$

Generalized forms of this integral with degenerate matrices B (i.e., the cases of a ball rolling on a paraboloid, cone, or cylinder) can be found in [4]. Integral of motion (19) can be represented as a generalization of the Ioahimstale quadratic integral for the Jacobi problem. This integral was initially found by the authors numerically with the use of the Poincaré three-dimensional map in the Andoyer–Depry variables (L, G, H, l, g, h) described in detail, e.g., in [2]. The computer simulation of this map, in which the system under consideration was numerically integrated for a fixed energy, allowed us to find the integrals and to give the graphical interpretation in various cases of their existence. The three-dimensional cross sections of the phase flow are shown in Fig. 2 in terms of the variables l, $\frac{L}{G}$, $\frac{H}{G}$, and g for a fixed energy E = const. The cutting plane is

$g = \frac{\pi}{2}$. As can be seen, the three-dimensional phase portrait is separated into two-dimensional surfaces F_2 = const which nevertheless contain chaotic motions. This fact (i.e., the presence of chaotic motions on the two-dimensional surfaces F_2 = const) indicates that, in the case under consideration, there exists no additional independent integral ensuring the complete integrability and separation of the three-dimensional space into invariant curves.

The spatial dependence of integral (19) is very complicated, even though the integral is quadratic in velocities (**M** or **ω**). This could be the reason that this integral was not found in classical studies. (For example, it was noted by neither E. Routh nor F. Noether, who analyzed particular solutions.)

REFERENCES

1. P. Appell, *Traité de mécanique rationelle* (Gauthier-Villar, Paris, 1950; Fizmatgiz, Moscow, 1960).
2. A. V. Borisov and I. S. Mamaev, *Poisson Structures and Lie Algebras in Hamiltonian Mechanics* (RKhD, Izhevsk, 1999).
3. A. V. Borisov and I. S. Mamaev, Reg. Khaot. Dinam. **7** (2), 177 (2002).
4. A. V. Borisov, A. A. Kilin, and I. S. Mamaev, Reg. Khaot. Dinam. **7** (1), 201 (2002).
5. Yu. I. Neimark and N. A. Fufaev, *Dynamics of Nonholonomic Systems* (Nauka, Moscow, 1967).
6. E. Routh, *Dynamics of a System of Rigid Bodies* (Dover, New York, 1955; Nauka, Moscow, 1983), Vol. 2.

Translated by V. Chechin

Doklady Physics, Vol. 47, No. 7, 2002, pp. 548–551. Translated from Doklady Akademii Nauk, Vol. 385, No. 3, 2002, pp. 342–345.

MECHANICS

Fracture Constants for Ideal Rigid–Plastic Bodies

O. V. Kozlova and A. I. Khromov

Presented by Academician V.P. Myasnikov September 10, 2001

Received March 7, 2002

Fundamentals of the theory of strain and fracture of rigid–plastic bodies were considered in [1–3]. This study is devoted to determining fracture constants under axisymmetric strain. As the main fracture constant we take the specific energy dissipation in the process of particle deformation or (an equivalent formulation) the largest principal value of the Almansi finite-strain tensor. The fracture constants are determined from the reduction of area at fracture by solving the problem of the uniaxial extension of a rigid–plastic cylinder.

Fracture criteria. We assume that the fracture of a material at a crack tip occurs if the specific energy dissipation W achieves a limiting value W_*:

$$W \geq W_*. \tag{1}$$

Here, the equality determines the crack propagation velocity.

It was noted in [1] that the specific energy dissipation is bijectively related to the invariants of the Almansi finite-strain tensor

$$E_{ij} = \frac{1}{2}\left(\delta_{ij} - \frac{\partial x_k^0}{\partial x_i}\frac{\partial x_k^0}{\partial x_j}\right), \quad i, j = 1, 2, 3$$

and, in particular, to the first principal value E_1. Therefore, criterion (1) can be replaced by a local strain criterion: the fracture of a material occurs if the first principal value E_1 (largest in modulus) of the Almansi tensor achieves the limiting value E_*:

$$E_1 \geq E_*. \tag{2}$$

For axisymmetric deformation, the direction of crack development coincides with the symmetry axis (r-axis).

Let us consider the uniaxial tension of a round cylinder made of an ideal rigid–plastic material (Fig. 1). Tension occurs under the kinematical boundary conditions where the upper and lower ends of the cylinder move with the velocity $V = 1$ upward and downward along the z axis, respectively.

We assume that the plastic region is concentrated within the triangle BOC and that the region situated above the straight line OB and below the straight line OC moves as a rigid body; the free surface BC, whose generatrix BC was a segment of a straight line at the initial time, bends and takes the shape of a neck. In this case, the rigid–plastic boundaries OB and OC are the surfaces of velocity discontinuity.

The evolution of the free surface BC and the plastic region OBC can be described by conventional numerical methods outlined in [4–6].

The total strain of particles of a material occurs in two stages. In the first stage, particles are deformed at the internal points of the plastic region, where the velocity field is continuous and the specific power of energy dissipation and the components of the strain-velocity tensor have finite values. In the second stage, a particle is deformed when crossing the surface of the velocity discontinuity OB or OC, and the specific energy dissipation and the components of the strain tensor change by finite values. The strain of the particle at the second stage considerably exceeds its strain at internal points of the plastic region. This property makes it possible to formulate a local criterion of the fracture of a material in terms of the strain of particles at a surface of velocity discontinuity.

It was shown in [1, 2] that the strain at the surfaces of velocity discontinuity is determined by the specific energy dissipation:

$$W = \frac{k[V_\tau]}{V_n + G}, \quad \overline{W} = \frac{W}{k}, \tag{3}$$

where $[V_\tau]$ is the discontinuity of the transverse component of the velocity, V_n is the normal component of the velocity at the surface of discontinuity, G is the normal velocity of the discontinuity surface, and k is the yield point. If the strains of a particle are small below the discontinuity curve and if the material is not deformed up to the curve of discontinuity, the quantity $\overline{W}$ is related

Institute of Mechanical Engineering and Metallurgy, Far-East Division, Russian Academy of Sciences, ul. Metallurgov 1, Komsomolsk-on-Amur, Khabarovsk kraĭ, 681005 Russia

1028-3358/02/4707-0548$22.00

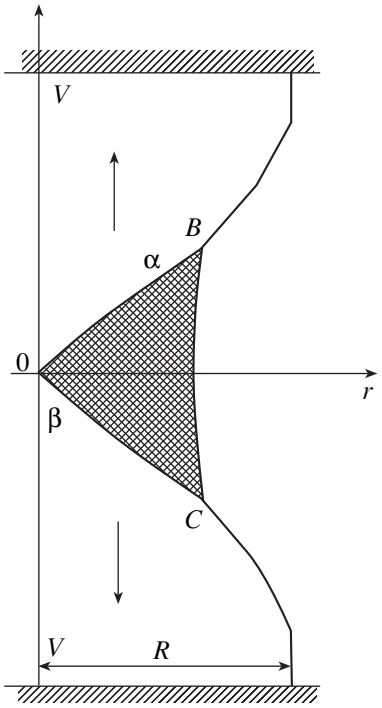

Fig. 1. Strain of a cylindrical sample subjected to a uniaxial extension.

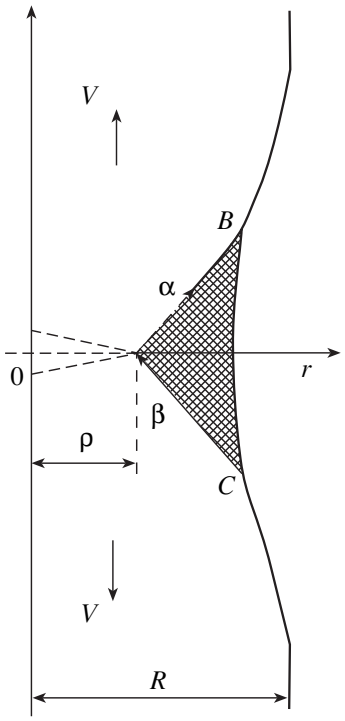

Fig. 2. Spreading of a crack within a cylindrical sample.

to the first principal value of the Almansi tensor ($E_{ij} = \delta_{ij}$) by the equation

$$E_1 = \frac{\overline{W}^2}{4}\left(\sqrt{1+\frac{4}{\overline{W}^2}}-1\right). \quad (4)$$

The quantities G and V_n can be determined by solving the problem of the tension of the cylinder with allowance for the variation of the shape of the free surface CB, for example, by the numerical methods in [4–6].

The quantity $[V_\tau]$ is determined from the following equations for the components of the velocities:

$$\begin{aligned} dV_\alpha - V_\beta d\varphi + u\frac{dS_\alpha}{2r} &= 0 \quad \text{on } \alpha \text{ slip line}, \\ dV_\beta - V_\alpha d\varphi + u\frac{dS_\beta}{2r} &= 0 \quad \text{on } \beta \text{ slip line}, \end{aligned} \quad (5)$$

where V_α and V_β are the velocity components along the α and β slip lines, respectively; u is the component of the velocity along the r axis; φ is the slope angle of the α slip line to the r axis; and dS_α and dS_β are the elements of arcs of the α and β slip lines, respectively.

The boundary conditions for the velocities are

$$\begin{aligned} V_\alpha &= V\cos\varphi \quad \text{on } \alpha \text{ slip line } OB, \\ V_\beta &= -V\sin\varphi \quad \text{on } \beta \text{ slip line } OC. \end{aligned} \quad (6)$$

We further consider the case where the deformation of a cylinder results in fracture, assuming that a crack begins developing from the cylinder axis (Fig. 2). In this case, the integration of Eqs. (5) with boundary conditions (6), for example, along the curve OB, leads to the relation

$$[V_\tau] = [V_\alpha] = V\sqrt{\frac{2\rho}{r}}, \quad (7)$$

where ρ is the coordinate of the crack tip on the r axis.

It follows from Eqs. (3), (4), and (7) that the energy dissipation as well as E_1 is larger in particles crossing the line of the discontinuity of velocities closer to the axis of the cylinder, and reaches a maximal value at the crack tip. In particular, we have

$$V_n = V\sin\varphi, \quad \overline{W} = \sqrt{\frac{2\rho}{r}}\frac{V}{G+V\sin\varphi} \quad (8)$$

for the line OB and

$$V_n = \frac{V}{\sqrt{2}}, \quad \overline{W} = \frac{2V}{\sqrt{2}G+V} \quad (9)$$

at the crack tip, where $r = \rho$ and $\varphi = \frac{\pi}{4}$. The velocity of the crack tip is related to the quantities G and $\overline{W}$

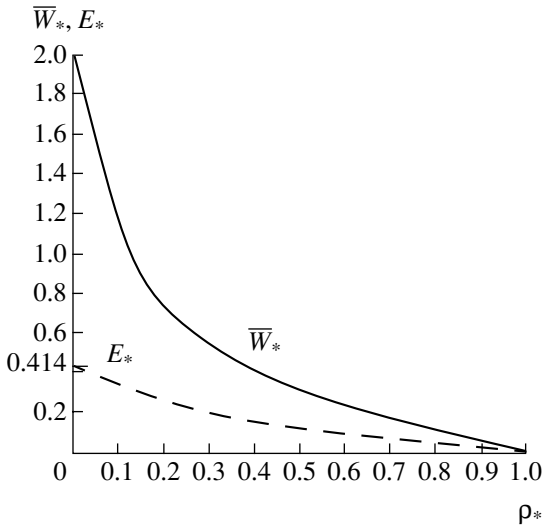

Fig. 3. Fracture constants versus the radius of the sample neck formed at the final instant.

by the equations

$$\frac{d\rho}{dt} = \frac{G}{\sqrt{2}}, \quad \frac{d\rho}{dt} = \frac{V}{\sqrt{2}}\left(\frac{2}{\overline{W}} - 1\right), \tag{10}$$

respectively. If the crack does not extend, we have

$$G = 0, \quad \overline{W} = 2, \quad E_1 = \sqrt{2} - 1 \approx 0.414. \tag{11}$$

Quantities (11) are independent of ρ. For $\rho \longrightarrow 0$, they correspond to a continuous cylinder; i.e., strain (and specific energy dissipation $\overline{W}$) is largest on the cylinder axis. Therefore, the assumption that particles in the vicinity of the cylinder axis will suffer fracture is well justified.

Fracture constants for various materials

Material	ψ, %	$\overline{W}_*$	E_*
N12K12M10TYu steel	4	0.02	0.01
ML3 magnesium alloy	11	0.04	0.025
BrOTsS4-4-2.5 bronze (cast)	13	0.048	0.028
SCh10 cast iron	20	0.07	0.038
BrOTsS4-4-4 bronze (soft)	34	0.1	0.048
OT4-0 titanium alloy	35	0.105	0.05
D18 aluminum alloy	50	0.16	0.078
AD0 aluminum	60	0.19	0.09
Kh5N12M3T steel	61	0.2	0.092
AMg2 aluminum alloy	65	0.212	0.096
BrBNT1.7 bronze	75	0.28	0.12
L96 brass (soft)	82	0.337	0.148

It follows from relations (9)–(11) and criteria (1) and (2) that, if the material does not undergo fracture at $\overline{W} = 2$ or $E_1 = \sqrt{2} - 1$, the cylinder is divided into two parts through viscous fracture. The final area of the cross section of the cylinder will be ∅ ($F = \varnothing$). In addition, the fracture constants satisfy the relations

$$\overline{W}_* < 2, \quad E_* < \sqrt{2} - 1. \tag{12}$$

Determination of the fracture constants. The reduction of area

$$\psi = \frac{F_0 - F}{F_0} \times 100, \tag{13}$$

where $F_0 = \pi R^2$ and $F = \pi\rho_*^2$ are the cross-sectional areas of the sample prior to the formation of a neck and immediately before fracture, respectively, is one of the experimentally determined characteristics of uniaxial tension.

The condition ψ < 100% or $F > 0$ implies that a crack develops within a cylinder under tension. It follows from Eq. (10) that

$$\rho_* = \frac{V}{\sqrt{2}}\left(\frac{2}{\overline{W}_*} - 1\right)t_*, \tag{14}$$

where t_* is the instant of the fracture of the sample. Since the tension process is assumed to be quasistatic, the quantity t_* can be related to the final displacement from the ends of the cylinder as

$$h_* = Vt_*. \tag{15}$$

It follows from Eqs. (13)–(15) that

$$\overline{W}_* = \frac{1}{2}h_* \Big/ \left(\sqrt{2R^2\left(1 - \frac{\psi}{100}\right)} + h_*\right). \tag{16}$$

The quantity h_* can be determined by solving the problem of cylinder tension resulting in fracture.

The table presents the fracture constants for various materials. The values of h_* were determined by numerically solving the problem of cylinder tension with allowance for a variation in the neck shape and fracture. The coefficient ψ was found from [7].

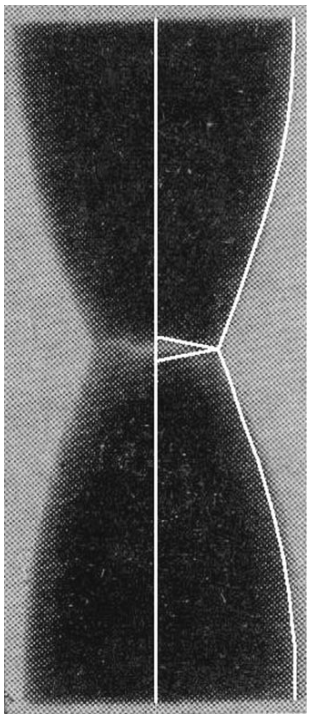

Fig. 4. X-ray photograph of the sample neck immediately before fracture [8] and the neck shape obtained from theoretical calculations (solid white curve in the right-hand part of the photograph).

Figure 3 shows the fracture constants versus the neck radius ρ_* at the instant of fracture (at $R = 1$). The x-ray photograph of the sample neck immediately before fracture [8] is presented in Fig. 4, along with the calculations of the shapes of the neck and crack in the model of the fracture of a perfect rigid–plastic body.

ACKNOWLEDGMENTS

This work was supported by the Russian Foundation for Basic Research, project no. 01-01-00717.

REFERENCES

1. A. I. Khromov, Dokl. Akad. Nauk **362**, 202 (1998) [Dokl. Phys. **43**, 587 (1998)].
2. A. I. Khromov, *Strain and Destruction of Rigid-Plastic Bodies* (Nauka, Vladivostok, 1996).
3. G. I. Bykovtsev and D. D. Ivlev, *The Theory of Plasticity* (Dal'nauka, Vladivostok, 1998).
4. B. A. Druyanov and R. I. Nepershin, *Problems of Technological Plasticity* (Mashinostroenie, Moscow, 1990; Elsevier, Amsterdam, 1994).
5. W. Prager, *Problem der Plastizitäts Theorie* (Basel, 1995).
6. A. Yu. Ishlinskiĭ, Prikl. Mat. Mekh. **8** (3), 201 (1944).
7. *Structural Materials: Handbook*, Ed. by B. N. Arzamasov (Mashinostroenie, Moscow, 1990).
8. A. Nadai, *Theory of Flow and Fracture of Solids* (McGraw-Hill, New York, 1963; Mir, Moscow, 1969), Vol. 2.

Translated by T. Syromyatnikova

Doklady Physics, Vol. 47, No. 7, 2002, pp. 552–557. Translated from Doklady Akademii Nauk, Vol. 385, No. 3, 2002, pp. 346–351.

MECHANICS

Use of the Bulk Harmonic Fall Velocity in Mechanical Calculations at Two Levels of Input Data

N. V. Sokolov

Presented by Academician G.G. Chernyĭ March 13, 2002

Received March 1, 2002

Many current problems of ecological mechanics must be solved with incomplete information about the motion of large aggregates of liquid and solid particles in liquid and gas flows [1–5]. These problems require the averaging of physical fields [6], calculation of the moments of random variables [7], and experimental determination of the bulk characteristics of particles [1, 2, 5, 8] and their use in mechanical calculations. One of these characteristics is the bulk harmonic (or mean harmonic) fall velocity of particles. As will be shown below, this quantity can be directly determined from the curve of sediment-mass accumulation for small concentrations of particles in a stationary liquid.

The comparison of two expressions for the bulk time of the sedimentation of particles indicates that

$$\frac{1}{G_{\max}}\int_0^{T_{\max}} \tau dG(\tau) = \int_{V_{\min}}^{V_{\max}}\int_0^H \frac{x}{V} dF_h(x) dF_v(V), \qquad (1)$$

where $T_{\max}$ is the time of the compete sedimentation of particles in a sedimentometer; $G_{\max} = G(T_{\max})$; $F_v(V)$ is the integral bulk distribution function of the fall velocity of particles; $F_h(x)$ is the distribution function of the initial distance of particles from the bottom–liquid phase boundary; H is the depth of the sedimentometer; V is the fall velocity (the velocity of the sedimentation of particles in a stationary liquid in the presence of gravitation); $V_{\min}$ and $V_{\max}$ are the minimum and maximum fall velocities, respectively; x and τ are the space and time integration variables, respectively; and $G(\tau)$ is the sediment mass at time τ.

For a uniform initial depth distribution of particles in the sedimentometer and constant sedimentation velocities of particles, the integration by parts of the left-hand side of Eq. (1) yields

$$\overline{V^{-1}} = \frac{2}{HG_{\max}}\int_0^{T_{\max}} [G_{\max} - G(\tau)] d\tau, \qquad (2)$$

where $\overline{V^{-1}} = \int_{V_{\min}}^{V_{\max}} \frac{1}{V} dF_v(V)$ is the quantity inverse to the bulk harmonic fall velocity. When Stokes' law is valid in the sedimentometer, the quantity $\overline{V^{-1}}$ is proportional to the previously introduced mean radius of particles. However, this quantity can also be determined when Stokes' law is violated, in particular, in non-Newtonian liquids.

Another important characteristic of the mechanical behavior of particles is the bulk fall velocity $\bar{V} = \int_{V_{\min}}^{V_{\max}} V dF_v(V)$. It can be easily determined in the initial section of the curve of mass accumulation in the sedimentometer. Indeed, for the uniform initial depth distribution of particles in the sedimentometer, we have

$$\frac{G(t)}{G_{\max}} = \int_{\frac{H}{t}}^{V_{\max}} dF_v(V) + \frac{t}{H}\int_{V_{\min}}^{\frac{H}{t}} V dF_v(V). \qquad (3)$$

It follows from Eq. (3) that

$$\bar{V} = \int_{V_{\min}}^{V_{\max}} V dF_v(V) = \frac{H}{G_{\max}} \left.\frac{dG(t)}{dt}\right|_{t < \frac{H}{V_{\max}}}; \qquad (4)$$

i.e., the bulk fall velocity is the product of the slope of the initial linear section of the curve of mass accumulation in the sedimentometer and the ratio of the depth to the maximum sediment mass.

As is known, the minimum and maximum fall velocities $V_{\min}$ and $V_{\max}$ are the ratios of the sedimentometer depth to the time of sedimentation completion and to the time of the termination of the linear section of sediment mass accumulation, respectively. These characteristics are certainly determined much less accurately than mean characteristics. The error in the determination of the distribution function of the fall velocity increases when poorly justified assumptions

Water Problems Institute, Russian Academy of Sciences, Novaya Basmannaya ul. 10, Moscow, 107078 Russia

1028-3358/02/4707-0552$22.00

about its specific form are made or when the methods of numerical and graphical differentiation are applied.

Below, we will demonstrate how hydromechanically determined characteristics can be used to estimate the carrier properties of liquid flows when information is incomplete. The advantages of this approach will also be discussed.

The relative entrainment, i.e., the expected value of the mass fraction of particles carried away by liquid flows, can be expressed as

$$\varepsilon = \int_{V_{min}}^{V_{max}} P(V)dF_\nu(V), \quad (5)$$

where $P(V)$ is the probability that liquid flows carry away the mass associated with a particle whose initial fall velocity is V. The degree of separation has the form

$$\kappa = 1 - \int_{V_{min}}^{V_{max}} P(V)dF_\nu(V). \quad (6)$$

In what follows, $F_\nu(V)$ is treated as an unknown (undefinable) function.

Let us study the possibilities of estimating the results of transporting large aggregates of particles when data on the mean harmonic and bulk fall velocities are incomplete. The solution to this problem requires upper and lower estimates of the integral $\int_{V_{min}}^{V_{max}} P(V)dF_\nu(V)$. For upper estimates, we write the inequality

$$\varepsilon \le F_\nu(V_\alpha)\sup_{\omega \in \Omega} P(V) + [1 - F_\nu(V_\alpha)]\sup_{\omega:\, V \ge V_\alpha} P(V), \quad (7)$$

where ω are elementary events and Ω is the space of elementary events. Then,

$$\varepsilon \le \sup_{\omega:\, V \ge V_\alpha} P(V) + [\sup_{\omega \in \Omega} P(V) - \sup_{\omega:\, V \ge V_\alpha} P(V)]F_\nu(V_\alpha). \quad (8)$$

The similar inequality for lower estimates has the form

$$\varepsilon \ge \inf_{\omega \in \Omega} P(V) + [\inf_{\omega:\, V < V_\alpha} P(V) - \inf_{\omega \in \Omega} P(V)]F_\nu(V_\alpha). \quad (9)$$

Therefore, further calculations require upper and lower estimates of the integral bulk distribution function in the fall velocity. To obtain these estimates, we write the relations

$$F_\nu(V)V^{-1} + V_{max}^{-1}[1 - F_\nu(V)] \le \overline{V^{-1}}, \quad (10)$$

$$F_\nu(V)V + V_{max}[1 - F_\nu(V)] \ge \bar{V}, \quad (11)$$

$$F_\nu(V)V_{min} + V[1 - F_\nu(V)] \le \bar{V}, \quad (12)$$

$$F_\nu(V)V_{min}^{-1} + V^{-1}[1 - F_\nu(V)] \ge \overline{V^{-1}}, \quad (13)$$

which yield the inequalities

$$F_\nu(V) \le \frac{\overline{V^{-1}} - V_{max}^{-1}}{V^{-1} - V_{max}^{-1}}, \quad (14)$$

$$F_\nu(V) \le \frac{V_{max} - \bar{V}}{V_{max} - V}, \quad (15)$$

$$F_\nu(V) \ge \frac{V - \bar{V}}{V - V_{min}}, \quad (16)$$

$$F_\nu(V) \ge \frac{\overline{V^{-1}} - V^{-1}}{V_{min}^{-1} - V^{-1}}. \quad (17)$$

Combining Eqs. (8), (14), and (15), we obtain the following upper estimates of the relative entrainment:

$$\varepsilon \le \sup_{\omega:\, V \ge V_\alpha} P(V) + [\sup_{\omega \in \Omega} P(V) - \sup_{\omega:\, V \ge V_\alpha} P(V)]\frac{\overline{V^{-1}} - V_{max}^{-1}}{V_\alpha^{-1} - V_{max}^{-1}}, \quad (18)$$

$$\varepsilon \le \sup_{\omega:\, V \ge V_\alpha} P(V) + [\sup_{\omega \in \Omega} P(V) - \sup_{\omega:\, V \ge V_\alpha} P(V)]\frac{V_{max} - \bar{V}}{V_{max} - V_\alpha}, \quad (19)$$

where the fall quasi-velocity of separation V_α characterizes the action of various physical fields and liquid flow on particles and is defined as the minimum fall velocity of probe particles such that the probability of the entrainment of particles whose fall velocities are no less than this value is no more than α, i.e., $\alpha = \sup_{\omega:\, V \ge V_\alpha} P(V)$.

Combining Eqs. (9), (16), and (17), we obtain the following lower estimates of the fall velocity of particles:

$$\varepsilon \ge \inf_{\omega \in \Omega} P(V) + [\inf_{\omega:\, V < V_\alpha} P(V) - \inf_{\omega \in \Omega} P(V)]\frac{V_\alpha - \bar{V}}{V_\alpha - V_{min}}, \quad (20)$$

$$\varepsilon \ge \inf_{\omega \in \Omega} P(V) + [\inf_{\omega:\, V < V_\alpha} P(V) - \inf_{\omega \in \Omega} P(V)]\frac{\overline{V^{-1}} - V_\alpha^{-1}}{V_{min}^{-1} - V_\alpha^{-1}}. \quad (21)$$

Thus, even when data on the distribution function of the fall velocity are absent and information about the probability of transporting particles with different fall characteristics by flows is incomplete, the carrier action of flows can be estimated by using data on the mean harmonic or bulk fall velocity.

Table 1. Point estimates, auxiliary expressions, and data of liquid-mechanical experiments

V_α, m/s	$\frac{\overline{V^{-1}} - V_{max}^{-1}}{V_\alpha^{-1} - V_{max}^{-1}}$	$\frac{V_{max} - \overline{V}}{V_{max} - V_\alpha}$	$\frac{V_\alpha - \overline{V}}{V_\alpha - V_{min}}$	$\frac{\overline{V^{-1}} - V_\alpha^{-1}}{V_{min}^{-1} - V_\alpha^{-1}}$	ε, %		κ, %		Absolute error magnitude
					experimental value	point estimate	point estimate	experimental value	
3.93×10^{-5}	0.325	0.606			2	15	85	98	13
5.88×10^{-5}	0.5	0.613			7.4	25	75	92.6	17.6
1.18×10^{-4}		0.63		0.156	20.4	31.5	68.5	79.6	11.1
2.36×10^{-4}		0.684		0.176	31.5	34.2	65.8	68.5	2.7
3.5×10^{-4}		0.741		0.233	36	37	63	64	1
7×10^{-4}		0.99		0.274	44	49.5	50.5	44.4	6.1
$*8.84 \times 10^{-4}$			0.193	0.28	**59	*57	*43	**41	2

Note: The absence of values implies that the calculation of auxiliary expressions is inappropriate.

* With the use of the fall entrainment velocity at $\inf_{\omega: V < V_\alpha} P(V) = 0.5$.

** Corresponding experimental value; in these cases, $\alpha = 0.5$; otherwise, $\alpha = 0$.

However, upper estimates (18) and (19) are applicable only for fall separation quasi-velocities lower than the mean harmonic and bulk fall velocities of particles. In contrast, the lower estimates are applicable in the opposite case. This circumstance excludes the possibility of simultaneously using all four Eqs. (18)–(21).

It is reasonable to take the middle of the estimate interval for a point estimate:

$$\varepsilon_{t_1} = \frac{\varepsilon_u}{2}, \tag{22}$$

$$\varepsilon_{t_2} = \varepsilon_l + \frac{1 - \varepsilon_l}{2}, \tag{23}$$

where ε_u is the smallest among upper estimates (18) and (19), whereas ε_l is the largest among lower estimates (20) and (21).

To illustrate the capabilities of the above estimates, experiments on the sedimentation of solid particles in a liquid were carried out. The procedure proposed above yields the following mean and bound fall characteristics.

Mean characteristics: the mean harmonic fall velocity (bulk harmonic fall velocity) and bulk fall velocity are equal to 1.138×10^{-4} and 7.2×10^{-4} m/s, respectively, and $\overline{V^{-1}} = 8784.1$ s/m. Bound characteristics: $V_{min} = 3.533 \times 10^{-5}$ m/s, $V_{max} = 1.767 \times 10^{-3}$ m/s, $V_{min}^{-1} = 28304.6$ s/m, and $V_{max}^{-1} = 565.9$ s/m.

Table 1 presents the values calculated for auxiliary expressions: point estimates for the relative entrainment calculated by Eqs. (22) and (23) and point estimates of the degree of separation, as well as experimental data on the sedimentation of an aggregate of particles. To estimate the relative entrainment, no more than two of Eqs. (18)–(21) can be used simultaneously. In this run of experiments, the average error of point estimates was 7.8%.

Relations (14) and (15) also enable us to refine the Markov inequality (one of the simple Chebyshev-type inequalities) and to obtain its addition by taking into account the possible singularity of function $F_V(V)$, relation between probabilities and distribution functions with singularities, and the formal change of velocity to any inverse nonnegative random variable. With this generalization, we obtain

$$P\{X \geq a_0\} \leq \frac{\mathrm{E}[X] - [\inf_{\omega \in \Omega} X]}{[\inf_{\omega: X \geq a_0} X] - [\inf_{\omega \in \Omega} X]} \leq \frac{\mathrm{E}[X] - [\inf_{\omega \in \Omega} X]}{a_0 - [\inf_{\omega \in \Omega} X]} \leq \frac{\mathrm{E}[X]}{a_0}, \tag{24}$$

$$P\{X \geq a_0\} \leq \frac{[\inf_{\omega \in \Omega} X]^{-1} - \mathrm{E}[X^{-1}]}{[\inf_{\omega \in \Omega} X]^{-1} - [\inf_{\omega: X \geq a_0} X]^{-1}} \leq \frac{[\inf_{\omega \in \Omega} X]^{-1} - \mathrm{E}[X^{-1}]}{[\inf_{\omega \in \Omega} X]^{-1} - 1/a_0}, \tag{25}$$

where $P\{X \geq a_0\}$ is the probability that $X \geq a_0$, EX is the expected value of an arbitrary random nonnegative variable X, and $a_0 >$ EX (for these a_0 values all estimates

of probability are lower). The comparison of Eqs. (24) and (25) with the Markov inequality

$$P\{X \geq a_0\} \leq \frac{EX}{a_0} \tag{26}$$

indicates that the above approach makes it possible to refine this inequality and obtain its addition.

Let us analyze another information level, namely, the case where the probability of carrying particles away by liquid flows is known as a function of the particle fall velocity. We introduce an auxiliary function $P^*(V) = \sup_{V_{max} \geq U \geq V} P(U)$, where U is an auxiliary variable. In what follows, we suppose that $P^*(V)$ is continuous at the discontinuity points of the function $F_v(V)$ and the distribution function $F_v(V)$ is continuous at the points where the function $P^*(V)$ is singular. In this case, we have

$$\varepsilon \leq \int_{V_{min}}^{V_{max}} P^*(V) dF_v(V). \tag{27}$$

If the function $P^*(V)$ is singular at the points $V = V_{min}$, V_{max}, $\overline{\overline{V^{-1}}}^{-1}$, or $\bar{V}$, the values $P^*(V_{min})$, $P^*(V_{max})$, $P^*\left(\overline{\overline{V^{-1}}}^{-1}\right)$, $P^*(\bar{V})$, or $P^*(V_{min} - 0)$, $P^*(V_{max} + 0)$, $P^*\left(\overline{\overline{V^{-1}}}^{-1} + 0\right)$, $P^*(\bar{V} + 0)$ must be assigned to its values at the corresponding points in the expressions below.

Integration by parts of the right-hand side of Eq. (27) yields

$$\int_{V_{min}}^{V_{max}} P^*(V) dF_v(V) = P^*(V_{max}) - \int_{V_{min}}^{V_{max}} F_v(V) dP^*(V). \tag{28}$$

An upper estimate for the distribution function of the initial fall velocity of particles can be obtained by Eqs. (14) and (15). Replacing the function by its upper estimate (14) and taking its applicability area into account, we obtain

$$\varepsilon \leq -\int_{V_{min}}^{\overline{\overline{V^{-1}}}^{-1}} \frac{\overline{V^{-1}} - V_{max}^{-1}}{V^{-1} - V_{max}^{-1}} dP^*(V) + P^*\left(\overline{\overline{V^{-1}}}^{-1}\right). \tag{29}$$

One more integration by parts yields

$$\varepsilon \leq (\overline{V^{-1}} - V_{max}^{-1}) \times \left[\frac{P^*(V_{min})}{V_{min}^{-1} - V_{max}^{-1}} + \int_{V_{min}}^{\overline{\overline{V^{-1}}}^{-1}} \frac{V^{-2} P^*(V)}{(V^{-1} - V_{max}^{-1})^2} dV\right]. \tag{30}$$

Taking into account that a proper fraction increases when its numerator and denominator increase simultaneously by the same amount, one can reduce Eq. (30) to the simpler but less accurate estimate

$$\varepsilon \leq \overline{V^{-1}} \left[V_{min} P^*(V_{min}) + \int_{V_{min}}^{\overline{\overline{V^{-1}}}^{-1}} P^*(V) dV\right], \tag{31}$$

where the first term can sometimes be negligible compared to the second term.

Using estimate (15) instead of Eq. (14), we obtain the similar estimate

$$\varepsilon \leq -(V_{max} - \bar{V}) \int_{V_{min}}^{\bar{V}} \frac{dP^*(V)}{V_{max} - V} + P^*(\bar{V}). \tag{32}$$

One more integration by parts yields

$$\varepsilon \leq (V_{max} - \bar{V}) \times \left[\frac{P^*(V_{min})}{V_{max} - V_{min}} - \int_{V_{min}}^{\bar{V}} P^*(V) \ln(V_{max} - V) dV\right]. \tag{33}$$

When probabilities $P(V)$ are determined experimentally and numerically, it is preferable to estimate the relative entrainment by Eqs. (30), (31), and (33), because they are free of numerical differentiation leading to larger errors. When the problems of the stochastic mechanical motion of particles are solved analytically and the functions $P(V)$ are found in an explicit form, inequalities (29) and (32) give less unwieldy intermediate expressions than do inequalities (30), (31), and (33) (the final results are certainly the same).

Let us analyze simple specific cases.

Solving the equations of motion for particles that have a uniform initial height distribution and settle out in a liquid which is stationary or executes slow plunger

Table 2. Estimates of the carrier action of a flow with the known fall-velocity dependence of the probability of carrying particles away

V_0, m/s	Relative entrainment					Absolute error magnitude, %
	experimental value	estimates with $\overline{V^{-1}}$		estimates with $\bar{V}$ by Eq. (37)	relative entrainment ε	
		by Eq. (35)	by Eq. (36)			
3.93×10^{-5}	2	≤3.5	≤3.3	≤6.3	1.7	0.3
5.88×10^{-5}	7.4	≤16.5	≤15.9	≤24	7.9	0.5
1.18×10^{-4}	20.4	≤47.2	≤46.3	≤43.4	21.7	1.3
2.36×10^{-4}	31.5	≤73.6	≤73.1	≤54.6	27.3	4.2
3.5×10^{-4}	36	≤82.2	≤81.9	≤60	30	6
7×10^{-4}	44	≤91.1	≤91.0	≤72	36	8
8.84×10^{-4}	48	≤92.9	≤92.8	≤78.2	39.1	8.9

motion in the laminar mode, we determine the probability as

$$P(V) = \begin{cases} 1 - \dfrac{V}{V_0}, & \text{for } V < V_0 \\ 0, & \text{for } V \geq V_0, \end{cases} \tag{34}$$

where the fall separation velocity V_0 is the minimum fall velocity of particles completely trapped under these conditions. In this case, $P^*(V) = P(V)$. Substituting Eq. (34) into Eq. (31) and performing integration, we obtain the estimate

$$\varepsilon \leq \begin{cases} \dfrac{1}{2} V_0 \overline{V^{-1}} \left[1 - \left(\dfrac{V_{\min}}{V_0} \right)^2 \right], & \text{for } V_{\min} \leq V_0 < \dfrac{1}{\overline{V^{-1}}} \\ 1 - \dfrac{1}{2} \left[\dfrac{1}{\overline{V^{-1}}} + \overline{V^{-1}} V_{\min}^2 \right] V_0^{-1}, & \text{for } V_0 \geq \dfrac{1}{\overline{V^{-1}}}, \end{cases} \tag{35}$$

which can be found even when the maximum fall velocity of particles is unknown.

Substituting probability (34) into Eq. (29) and using the integral tables from [9], one can obtain the following more accurate estimate of the relative entrainment, which is based on the mean harmonic fall velocity:

$$\varepsilon \leq \begin{cases} \dfrac{\overline{V^{-1}} - V_{\max}^{-1}}{V_0} V_{\max}^2 \left[\ln \dfrac{V_{\max} - V_{\min}}{V_{\max} - V_0} - \dfrac{V_0 - V_{\min}}{V_{\max}} \right], & \text{for } V_{\min} \leq V_0 < \dfrac{1}{\overline{V^{-1}}} \\ 1 - \dfrac{1}{\overline{V^{-1}} V_0} + \dfrac{\overline{V^{-1}} - V_{\max}^{-1}}{V_0} V_{\max}^2 \left[\ln \dfrac{V_{\max} - V_{\min}}{V_{\max} - 1/\overline{V^{-1}}} - \dfrac{1/\overline{V^{-1}} - V_{\min}}{V_{\max}} \right], & \text{for } V_0 \geq \dfrac{1}{\overline{V^{-1}}}. \end{cases} \tag{36}$$

Finally, calculating integrals in Eqs. (32) or (33) with the known bulk fall velocity, we obtain (after some manipulations)

$$\varepsilon \leq \begin{cases} \dfrac{V_{\max} - \bar{V}}{V_0} \ln \dfrac{V_{\max} - V_{\min}}{V_{\max} - V_0}, & \text{for } V_{\min} \leq V_0 < \dfrac{1}{\bar{V}} \\ 1 - \dfrac{\bar{V}}{V_0} + \dfrac{V_{\max} - \bar{V}}{V_0} \ln \dfrac{V_{\max} - V_{\min}}{V_{\max} - \bar{V}}, & \text{for } V_0 \geq \dfrac{1}{\bar{V}}. \end{cases} \tag{37}$$

Table 2 presents the point estimates obtained for the relative entrainment from Eqs. (35)–(37) and corresponding experimental data. For a point estimate, we use half the interval from zero to the least lower bound [least of Eqs. (35)–(37)].

Calculations indicate that in the cases under consideration, logarithmic estimate (36) is noticeably better than the simpler Eq. (35) only for fall separation velocities close to the minimum value. Compared to

Eqs. (35) and (36), the error of estimate (37) varies from a maximum to a minimum with increasing V_0.

As might be expected, the magnitude of the average absolute error of point estimates at this information level was found to be about 4%, which is less than the value for the case where the initial fall-velocity dependence of the probability of carrying particles away is unknown.

Thus, the bulk harmonic fall velocity of particles is efficiently applied to obtain the point estimates of the relative entrainment of an aggregate of disperse particles by liquid flows at two levels of input data. A correction to the Markov inequality was also found when deriving expressions for calculations. All experimental data entirely corroborate the applicability of resulting expressions. In this case, the bulk fall velocity was determined by a specially developed liquid-mechanical procedure.

REFERENCES

1. N. V. Sokolov, Dokl. Akad. Nauk **371**, 476 (2000) [Dokl. Phys. **45**, 167 (2000)].
2. N. V. Sokolov, Dokl. Akad. Nauk SSSR **287**, 177 (1986).
3. N. V. Sokolov, Dokl. Vses. Akad. S–kh. Nauk, No. 7, 31 (1989).
4. N. V. Sokolov, Dokl. Akad. Nauk SSSR **325**, 549 (1992).
5. N. V. Sokolov, Dokl. Akad. Nauk **337**, 70 (1994).
6. S. S. Grigoryan, Dokl. Akad. Nauk SSSR **254**, 846 (1980) [Sov. Phys. Dokl. **25**, 287 (1980)].
7. A. S. Monin and A. M. Yaglom, *Statistical Fluid Mechanics: Mechanics of Turbulence* (Gidrometeoizdat, St. Petersburg, 1992; MIT Press, Cambridge, Mass., 1971), Vol. 1.
8. N. V. Sokolov, Khim. Prom–st. (Moscow), No. 1, 39 (1987).
9. H. B. Dwight, *Tables of Integrals and Other Mathematical Data* (Macmillan, London, 1961; Nauka, Moscow, 1973).

Translated by R. Tyapaev